Exploring Star Formation and Dust Attenuation of Galaxies Using Multiwavelength Data

by

Yuan Fang-Ting

A dissertation submitted to Nagoya University in conformity with the requirements for the degree of Doctor of Philosophy.

Nagoya, Aichi

September, 2012

Abstract

This work takes advantage of multiwavelength data from ultraviolet to infrared to investigate the star formation and dust attenuation of local galaxies. The first part of this work focuses on star formation rate (SFR) calibrations using the mid-infrared (MIR) band luminosities of AKARI and WISE, and the second part investigates star formation and dust attenuation in major mergers.

In the first part, we investigate SFRs in a GALEX-SDSS-2MASS-AKARI sample of 153 nearby galaxies using the spectral energy distribution (SED) fitting method. We find the luminosities at the *S9W* and *L18W* bands of AKARI/IRC correlate with the SFR of galaxies in spite of complicated features contained in these bands. We present the SFR calibrations using *S9W* and *L18W* for the first time. Our calibrations are consistent with previous results based on Spitzer data. From the best models obtained by the SED fitting, we then built mock samples from redshift 0 to 2.5 to investigate SFR calibrations using WISE luminosities. We find that the W3 and W4 band luminosities can work as SFR indicators with small scatters. These SFR calibrations agree well with previous works within the uncertainties, and can be applied to dust-rich galaxies.

In the second part we studied a local sample of major merger galaxies and a control sample of isolated galaxies using GALEX ultraviolet (UV) and Spitzer infrared (IR) images. We find that dust attenuation in merger galaxies is enhanced with respect to isolated galaxies. We find this enhancement is contributed mainly by spiral galaxies in spiral-spiral (S-S) pairs, and increases with increasing stellar mass of a galaxy. Combining the IR and UV parts of SFRs, we then calculated the total SFRs and

specific star formation rates (SFR per stellar mass, SSFRs). We find the SSFRs to be enhanced in merger galaxies. This enhancement depends on galaxy stellar mass and the companion's morphology, but depends little on whether the galaxy is a primary or secondary component or on the separation between two components. These results are consistent with a previous study based only on IR images. In addition, we investigate the nuclear contributions to SFRs. SFRs in paired galaxies are more concentrated in the central part of the galaxies than in isolate galaxies. Our studies of dust attenuation show that the nuclear parts of pairs most resemble ultra-luminous infrared galaxies (ULIRGs). Including UV data in the present work not only provides reliable information on dust attenuation, but also refines analyses of SFRs.

Acknowledgements

First of all, I give my sincere gratitude to my adviser Prof. Takeuchi for the support of my study and research. His patience, smartness and knowledge helped me a lot during this three years. With his help, I had the chance to travel to Europe to study and meet a lot of researchers in my field. He has been a strong and supportive adviser, but he has always given me great freedom to pursue independent work. It is a great honor to be his first Ph.D student.

I also give my sincere thanks to the members of my thesis committee, Prof. Inutsuka, Prof. Tanabashi, Prof. Tobe and Prof. Matsumoto, who helped me a lot on improving this thesis.

I thank my teachers in Nanjing University. They taught me the basic knowledge of astronomy and encouraged me to be an astronomer. My special thanks go to Prof. Zhu, Prof. Cheng and Prof. Ding, who encouraged me to apply this Ph.D position at Nagoya University.

Prof. Buat, Prof. Burgarella, Dr. Giovannoli, Dr. Heinis and Prof. Iglesias-Páramo also deserve my sincerest thanks. My thanks go to Prof. Pollo as well for her great help on this thesis. It is my great pleasure to meet them and have the chance to work with them. They are excellent astronomers and I learned a lot from them.

I would like to thank Prof. Ishibashi, who helped me a lot for my living in Japan. Without him, I would not have had the chance to come to study at Nagoya University. I also give my thanks to Prof. Sugiyama for providing the GCOE funding, which makes me live comfortably in Japan.

I thank all my friends in the Department of Physics. I would like to give my special thanks to Ms. Fujiwara, Mr. Murata, Mr. Asano and Mr. Ikeyama, who

helped me solve plenty of troubles, especially when I just came to Japan, and to Dr. Matsuoka, for helping me a lot on my study and living in Japan and offering me the opportunity of observation. My special thanks also go to Dr. Stone, who helped me a lot on improving my English. Of course I won't forget to thank Ola and Kasia, for encouraging me all the time!

My friends in Nagoya University and around the world gives me a lot of joy and support. Special thanks go to Yu Yu, Xian Shi, Weiyu Du, Meilin Dai, Mengya Gao, Hanjing Wu and Gui Mei.

Last, I wish to thank my parents, Liqiang Yuan and Fang Fang, who raised me up and supported me in all my pursuits, for all their love and encouragement!

Contents

List of Figures

List of Tables

Chapter 1

Overview

The star formation rate (SFR) is an essential quantity for understanding the formation of galaxies and the evolution of the universe. However, dust attenuation introduces large uncertainties when measuring the SFR. In this chapter, we introduce the background knowledge and the context of our research of star formation and dust attenuation.

1.1 Basic cosmology

Physical cosmology is the research about the large-scale nature of the universe. The standard word picture (well known as 'Big Bang') of modern cosmology contains the following main elements: 1, the mass distribution in the universe is homogeneous in the large-scale average; 2, the universe is expanding, and the dynamics of the expansion is described by Einstein's general relativity[1]; 3, the universe expanded from a hot dense state where its mass was dominated by thermal blackbody radiation. In this section, we introduce the basics of physical cosmology and the connection between cosmology and the studies of galaxies. More details can be found in Peebles (1993) and Mo et al. (2010).

[1]The standard world picture is not applicable to the universe at early enough epochs, because it extrapolates back to a singular state in which conventional physics is undefined. Therefore, the 'inflation' model is used for the very early universe. The inflation theory is beyond the scope of this thesis, so we omit the description of this theory.

Cosmological principle

The standard cosmological model is based on the 'cosmological principle'. According to this principle, the universe is homogeneous and isotropic in the large-scale average.

The mass distribution of the universe can be traced by the distribution of galaxies. If the mass is uniformly distributed, the number counts of galaxies should follow

$$N(< m) \propto 10^{0.6m}, \tag{1.1}$$

where m is the apparent magnitude of galaxies.

Observations show that at intermediate distance galaxies are distributed following the $10^{0.6m}$ law. The number density of nearby galaxies is higher because of the local concentration of galaxies in and around the Virgo clusters. The departure from this law for very distant galaxies is caused by the time evolution of the galaxies and spacetime.

The mapping of galaxies using various methods of observations in the nearby and deep universe show that there is no preferential directions where galaxies show special concentration. Therefore, it is reasonable to believe that the universe is homogeneous and isotropic.

The expanding universe

Well established evidence ruled out the possibility that the universe is static. An expanding universe is concluded to explain the observations. The expansion means that the proper physical distance between two well-separated galaxies are receding from each other.

In an expanding universe it is convenient to use the comoving frame, which is connected to the object. In the comoving frame the position coordinates for an object do not change with time. Then the proper distance $l(t)$ between two galaxies is given by

$$l(t) = l_0 a(t), \tag{1.2}$$

where l_0 is constant and $a(t)$ is the scale factor that related to the universal expansion.

The receding velocity of a galaxy is

$$v = \dot{l} = l_0 \dot{a} = l\frac{\dot{a}}{a} \equiv Hl. \tag{1.3}$$

The receding velocity of galaxies can be interpreted as Doppler effect: When the galaxy is moving along the line of sight with a speed v_r, its spectrum will shift accordingly. Therefore, the shift of the spectrum of one galaxy is an indicator of its velocity. Due to the expansion, galaxies have redshifted spectra. The redshift is usually expressed as z, and can be calculated by the following equation:

$$1 + z = \frac{\lambda_{obs}}{\lambda_{emi}} = \frac{\lambda_{obs}}{\lambda_{emi}} = \frac{a_0}{a}, \tag{1.4}$$

where λ_{emi} is the wavelength of a photon emitted by the galaxy, λ_{obs} is the wavelength of the photon when it is observed by us, a is the scale factor at the time of emission of the radiation, and a_0 is at the time of observation.

The linear relation between distance and redshift is called Hubble's law. In 1929, Hubble measured the distance-redshift relation for some twenty-four relatively bright galaxies with redshifts $v \leq 1000$ km s^{-1}. The distances of these galaxies were measured using Cepheid variable stars, whose light changes periodically, and the period P depends on the luminosity L. Therefore, by measuring the period of the light change, we can obtain the luminosity. Then the distance d can be derived using

$$d^2 = \frac{L}{4\pi f} \tag{1.5}$$

by comparing the intrinsic luminosity L and apparent brightness f.

Hubble found that the redshift z and the distance d of these galaxies follow a linear relation:

$$cz = H_0 d \quad \texttt{for galaxies with } v_r << c, \tag{1.6}$$

where c is the speed of light, and H_0 is the Hubble constant.

The value of Hubble's constant is still subject to debate. The very recent measure of Hubble constant by NASA's Spitzer Telescope is reported as $H_0 = 74.3 \pm 2.1$ kms^{-1}Mpc^{-1}. Practically, the Hubble constant can be written as

$$H_0 = 100h\text{km}\,\text{s}^{-1}\text{Mpc}^{-1}, \tag{1.7}$$

where the dimensionless parameter h is believed to be between 0.5 and 0.85. Values around 0.7 are commonly adopted.

The classical Hubble relation (Equation 1.6) can be applied to measuring distances to nearby galaxies at $z < 0.1$ where the curvature of the universe can be ignored. For distant galaxies, it is found there are deviations from this linear relation. The reason of the deviations is that the expansion of the universe is accelerating. It can only be understood within a relativistic cosmological model.

In observation, most galaxies have redshifted spectra, but there are also galaxies with blueshifted spectra. The reason is that galaxies is also affected by the gravitational force in the galaxy cluster it belongs to, and when the gravitational effect that pulls it toward us is stronger than the effect of cosmological expanding, the spectrum of the galaxy can be observed blueshifted due to this peculiar velocity. For example, the spectrum of Andromeda galaxy is blueshifted because of the attraction from other galaxies in the local group. This peculiar velocity should be subtracted when calculating the redshift of the galaxy.

The dynamics of the universe is described by Einstein's theory of general relativity. Under the cosmological principle, Einstein's equations give rise to the Friedmann equations:

$$\frac{\ddot{a}}{a} = -\frac{4}{3}\pi G(\rho_b + 3p_b) + \frac{\Lambda}{3} \tag{1.8}$$

$$H^2 = \left(\frac{\dot{a}}{a}\right)^2 = \frac{8}{3}\pi G\rho_b + \frac{K}{a^2} + \frac{\Lambda}{3} \tag{1.9}$$

where ρ_b and p_b are the density and pressure of the ordinary material (such as stars, gas and radiation), Λ is the cosmological constant, G is the gravitational constant, and K is the curvature of the universe.

The universe with $z \leq 1000$ is dominated with matter with little pressure, and therefore $\rho_b \propto a^{-3}$. Then

$$H^2 = \left(\frac{\dot{a}}{a}\right)^2 = H_0^2[\Omega_m y^3 + \Omega_K y^2 + \Omega_\Lambda], \tag{1.10}$$

where $y = 1 + z = a_0/a$. The density parameter Ω_m is defined as

$$\Omega_m = \frac{8\pi G\rho_0}{3H_0^2}, \tag{1.11}$$

The curvature parameter Ω_K is

$$\Omega_K = \frac{K}{a_0^2 H_0^2}, \tag{1.12}$$

and the parameter related to the cosmological constant Ω_Λ is

$$\Omega_\Lambda = \frac{\Lambda}{3H_0^2}. \tag{1.13}$$

Assume a flat universe, the $\Omega_K = 0$, and the other two parameters contributes to the present expansion rate H_0 with

$$\Omega_m + \Omega_\Lambda = 1. \tag{1.14}$$

The distance and the time

Galaxies distribute from nearby to very distant universe, and they are so remote that even the light needs several years to reach us. The present age of the universe can be calculated by

$$t = \int_0^{a_0} \frac{da}{a} = \int_1^\infty \frac{dy}{y[\Omega_m y^3 + \Omega_K y^2 + \Omega_\Lambda]}, \tag{1.15}$$

where $y = 1 + z$. Figure 1.1 shows the relation between the redshift and the age of the universe, assuming the Λ-dominated flat cosmology: $\Omega_m = 0.3$, $\Omega_\Lambda = 0.7$, and $H_0 = 70\ \mathrm{km\,s^{-1}\,Mpc^{-1}}$.

Light from the most nearby galaxy, Canis Major Dwarf, needs 25,000 years to be observed by us. For other galaxies, it takes more time. The most distant galaxy with the highest confirmed spectroscopic redshift is UDFy-38135539. The redshift is $z = 8.6$, corresponding to just 600 million years after the Big Bang (~ 13 billion years before now). Therefore, as we observe through different distance, we actually observe through time. By observing galaxies at different redshifts, we are actually observing the evolution of the universe.

Structure and galaxy formation

Although in large-scale average, the universe is homogeneous and isotropic, in smaller scale, the inhomogeneous structures such as stars and galaxies exist. The

Figure 1.1 Relation between the redshift and the age of the universe. The Λ-dominated flat cosmology is adopted: $\Omega_m = 0.3$, $\Omega_\Lambda = 0.7$, and $H_0 = 70\ \mathrm{km\,s^{-1}\,Mpc^{-1}}$.

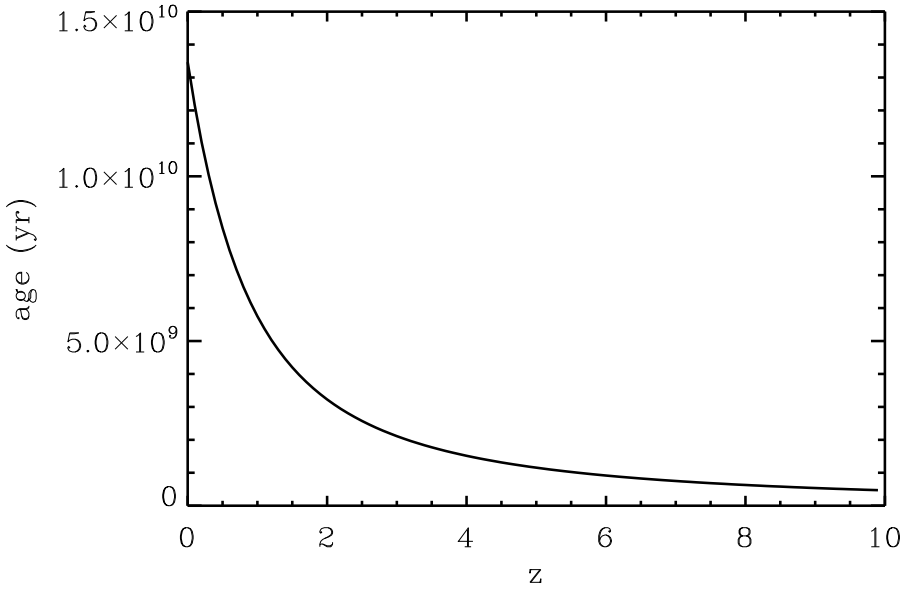

observation of the cosmic microwave background (CMB) proved that the very early universe is highly homogeneous and isotropic. Therefore, it is a question that how the structures of the present universe form from a homogeneous and isotropic state.

Theoretical models of cosmology must explain the structure formation in the universe. The leading theoretical paradigm is Λ-CDM model, which is also referred to as the standard model of the Big Bang picture. The model states that the universe contains a cosmological constant (dark energy), denoted by Λ, and cold dark matter. In the Λ-CDM model, structure formation is caused by the small deviation from homogeneity at the early universe. The small perturbations grow with time in an expanding universe dominated by non-relativistic matter due to the gravitational instability. Consequently, the difference of density between over-dense regions and under-dense regions becomes larger, and gravitation causes the over-dense regions to collapse.

In structure formation theory, the over-dense regions then become clumps composed of dark matter and gas. These clumps are proto-galaxies. Then the hydrogen and helium in the proto-galaxies starts to form stars, and the first galaxies form in the universe. The Λ-CDM model suggests hierarchical galaxy formation, in which galaxies gain their masses and form their shapes and structures by clustering and merging processes. The Λ-CDM model successfully predicts the large-scale structure in the distribution of galaxies. However, this model also has potential shortcomings such as that it underestimates the number of thin disk galaxies presented in the universe. The reason for the underestimation may be a prediction of too many mergers and therefore an overestimation of elliptical galaxies through merging processes(Steinmetz & Navarro 2002). Therefore, a further refinement of this model to precisely produce the galaxy populations in the universe is still a challenging topic in current cosmology.

1.2 Picture of the universe

Figure 1.2 illustrate the evolution of the universe. It can be seen that in early universe ($z > 15 - 30$), the intergalactic medium is neutral. The first galaxies were formed at $z \approx 10 - 30$. After this epoch, the reionization begins, the universe evolve

Figure 1.2 An illustration of the history of the universe, taken from Robertson Brant E. et al. (2010)

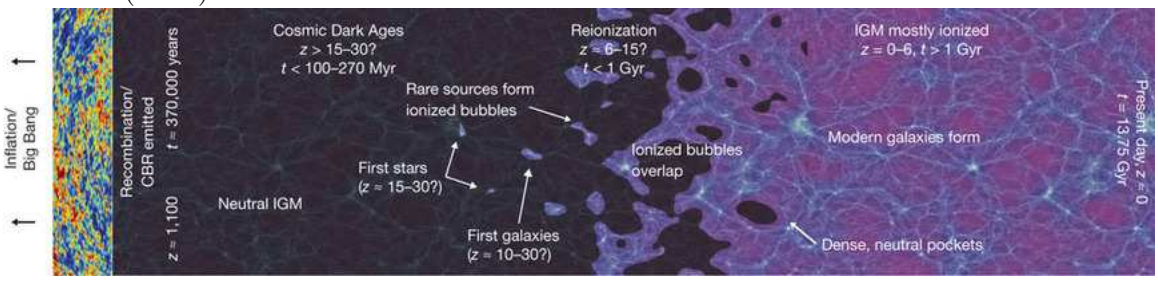

from neutral state to ionized state. The reionization and galaxy formation will be discussed in Section 1.7.

1.3 Galaxies

To understand our universe, it is necessary to investigate galaxies, the fundamental building blocks of the universe. As already mentioned in Section 1.1, galaxies are not only the bright sources which bring us information from local to deep universe, but also the test pool of physics laws (Binney & Merrifield 1998; Mo et al. 2010).

The concept that numerous nebulae in the sky are galaxies similar to our Milky Way was not confirmed until 1924, when Hubble determined the distance to Andromeda Nebula using Cepheid variable stars. He found that the distance to Andromeda is too large for it to be inside our own Galaxy. This finding renovated the view of the whole universe, and in modern time, with the advancing of the observation technique, the extragalactic astronomy becomes more and more popular and exciting.

1.3.1 Classification of galaxies

There are around 100 billion galaxies in the universe. Every galaxy has different physical properties. To systematically research their physics, astronomers divide them into several classes.

The first classification is the famous 'Hubble Tuning fork', which was introduced

by Hubble at the beginning of 20th century (Figure 1.3.1). According to Hubble's classification, galaxies are divided into elliptical galaxies, spiral galaxies, lenticular or S0 galaxies and Irregular galaxies with respect to their shapes:

1. The elliptical galaxy has smooth light distribution and a shape of an ellipse. Elliptical galaxies are further divided into E0 to E7 classes according to the ratios of the minor to major axes. E0 is the roundest elliptical galaxy.

2. The spiral galaxy is featured with a thin disk and several spiral arms. Spiral galaxies are further divided into two subcategories, normal spirals and barred spirals, according to the presence or absence of a barred structure. More specific classification of these two subcategories indexed using 'a, b, c' is according to the properties of central bulge component and spiral arms. For instance, a spiral galaxy with a luminous bulge, tightly wound spiral arms and faint HII regions is classified as an Sa galaxy. In contrast, a spiral galaxy with a faint bulge, loose arms and bright HII regions is classified as an Sc galaxy. Sometimes these properties give conflicting classification, and then the tightness that the arms are wound is the most important criterion to classify them.

   Some spiral galaxies have a bar-like structure. These galaxies are classified as barred spiral galaxies (SB). Barred galaxies are common in the universe. Approximately 1/3 of the spiral galaxies are barred galaxies. Similar to spiral galaxies, the barred spiral galaxies are also divided into subclasses of SBa, SBb and SBc.

3. The lenticular or S0 galaxy has a smooth light distribution. Lenticular or S0 galaxies are featured with a central bulge and a thin disk without spiral arms or HII regions. These galaxies are transition types between elliptical and spiral galaxies.

4. Galaxies lacking any dominant features and therefore cannot be classified into any types mentioned above are called irregulars. They have patchy appearance and no obvious symmetry.

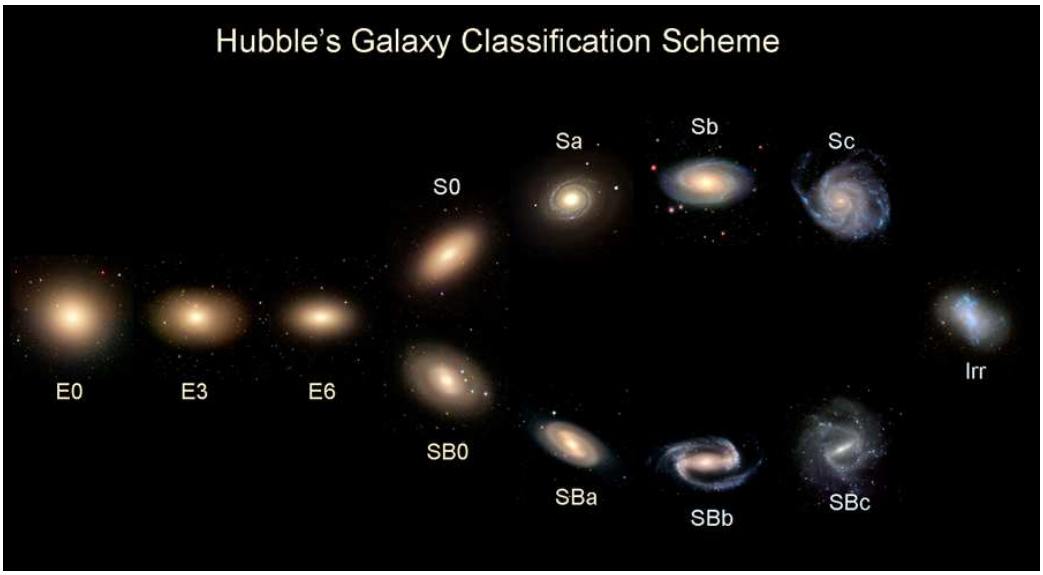

Figure 1.3 Hubble tuning fork diagram that illustrates the classification of galaxies, taken from `http://hendrix2.uoregon.edu/~imamura/123/lecture-3/lecture-3.html`.

The Hubble sequence was once thought to indicate the evolution of galaxies from the left side to the right side of Figure 1.3.1, and thus the elliptical and lenticular galaxies are also called 'early-type' galaxies and the spirals and irregulars are referred to as 'late-type' galaxies. Nowadays, it is found that the real situation may be just the reverse. However, the historical names are still used.

After Hubble, a significant amount of efforts were made to refine the classification of galaxies. The classification presented in de Vaucouleurs is commonly used in current researches. This classification is also based on the morphology of galaxies. It introduces new classes such as S0a, Sab, Sbc to the Hubble sequence to give finer classification of spiral galaxies, and it also extends the spiral galaxies to the irregular galaxies. Furthermore, de Vaucouleurs used numbers to represent each type of galaxies, which are called de Vaucouleurs' T types.

In addition, there are other methods of classification using the physical properties of a galaxy as criteria. These properties include luminosity, color, surface brightness, star formation rate, etc. We would like to mention that according to the current

level of star formation rate, galaxies can be divided into the quiescent and starburst categories. Starburst galaxies have very active star formation, and may reach a star formation rate of 1000 $M_{\odot}\,\mathrm{yr}^{-1}$. Also, the galaxy can be divided into the normal and active categories according to whether it contains an active nucleus.

Peculiar galaxies

The majority of the observed galaxies can be classified by the Hubble's classification and its revisions. However, there are also strange galaxies that appear unusual in their sizes, shapes or composition. These galaxies are called 'peculiar galaxies'. Peculiar galaxies have no typical features on their gas content or surface brightness. The features of morphology of these galaxies show that they have been strongly perturbed and are not in the state of dynamical equilibrium, indicating these galaxies appear as a result of interaction between galaxies and are undergoing a transition.

AGNs

As we mentioned above, galaxies can be divided into normal and active according to the presence of a central active nucleus (AGN). The nucleus is small, bright and dense and has distinct features with other components of one galaxy. The existence of AGNs in galaxies can be confirmed using X-ray observations. The AGN is thought to connect with the central massive blackhole of the galaxy. The activity may be caused by the accretion of gas into the massive blackhole.

1.3.2 General properties of galaxies on Hubble sequence

The reason why the morphological types are commonly used is that the morphological classification is correlated with the physical properties of galaxies. Galaxies of the same type usually share common physical properties such as color, gas content, star formation rate and dynamics. Here we give a general introduction to each type of galaxies:

Elliptical galaxies (E)

Elliptical galaxies usually have little gas and dust and lack the activity of star formation. They contain mainly old and red stars (Population II stars).

The size of elliptical galaxies varies in a large range. The largest elliptical galaxies can be over a million light-years in diameter ($\sim$ 10 times of the size of the Milky Way). The smallest dwarf elliptical galaxies are less than one-tenth the size of the Milky Way.

Spiral galaxies (S, SB)

Spiral galaxies are rich in gas and dust, and show signs of active star formation. The disk of a spiral galaxy is dominated by young and blue stars (Population I stars) and shows patterns of the spiral arms. These 'arms' are related to the star formation regions: The gas content is compressed there, and then young and blue stars form. The spiral arms are clearly visible because of the brightness of newly born stars. There are many spiral galaxies in the universe (more than 70% of the observed galaxies). The Milky Way and the Andromeda galaxy are both typical spiral galaxies.

On the other hand, the bulge of a spiral galaxy contains mainly old and red stars (Population II stars).

Except a disk and a bulge, a barred spiral galaxy has a bar-like structure in its center. Bars are thought to perform as a mechanism to induce gas from the spiral arms into the center and create new stars.

Lenticular galaxies (S0)

Lenticular galaxies contain mainly old stars. Lenticular galaxies have few signs of star formation because they used up or lost most of their interstellar matter during the evolution and therefore are unable to form new stars. There may be a significant amount of dust in their disks.

Similar to the spiral galaxies, some lenticular galaxies contain the bar-like structures. They are called 'barred lenticular galaxies' (SB0).

Irregular galaxies (Irr)

Irregular galaxies also contain abundant amounts of gas and dust. Most irregular galaxies are currently forming stars, and the star formation rate is comparable to that in spiral galaxies (Hunter 1997).

1.3.3 Galaxy merger

Galaxies in the universe are far from isolated. They frequently interact with each other. When the orbital energy of the interacting galaxies is sufficiently low, the systems may lead to a merger. Mergers play a very important role in the evolution of galaxies (see also Chapter 4).

Mergers are classified according to two their certain properties. The common classifications of mergers are listed as follows.

- According to the number of interacting galaxies, mergers can be divided into binary mergers and multiple mergers. The binary merger is caused by two interacting galaxies, while the multiple merger is caused by more than two galaxies.

- The mass of progenitor galaxies is used as the criterion to define 'major' and 'minor' mergers. A mass ratio q is defined as M_1/M_2, where M_1 and M_2 are the masses of the progenitor galaxies in a pair, and M_1 is assumed to be larger than M_2. Then if the value of q is less than four[2], the merger is called a major merger. In contrast, if q is larger than four, it is called a minor merger. In other words, the two components in a major merger have approximately the same size and mass, whereas in a minor merger, one component is significantly larger than the other. Major mergers can change the morphology of the progenitor galaxies significantly. Major mergers of two spiral galaxies can create an elliptical galaxy. On the other hand, in a minor merger, the larger galaxy absorbs most of the gas and stars in the smaller one with little change of other major properties, and the smaller galaxy dissolves.

[2]The number can be different by different authors.

- The mergers can also be divided by their gas content. A merger of gas-rich galaxies is called a 'wet merger', and the one of gas-poor galaxies is called a 'dry merger'. Wet mergers may induce active star formation, transform disk progenitor galaxies into elliptical galaxies, and trigger quasar and AGN activities. Dry mergers can not increase star formation rate, but can bring an increase of stellar mass as a result of merging. A merger of gas-rich and gas-poor galaxies is called a 'mixed merger'.

Although many details about the merging process are still remained to be understood, it is clear that the merger of two gas-rich galaxies can trigger starbursts and induce AGN activities. The contribution of merger processes to enhance the star formation rate and to turn on AGNs requires further quantitative investigations. In Chapter 4, we discuss the merger induced star formation using a local sample of close galaxy pairs.

1.4 Star formation in galaxies

The studies of the present and past star formation histories has been one of the most active fields of astronomical research during the last decade (Brinchmann et al. 2004). As mentioned in Section 1.3.2, galaxies on Hubble sequence have different star formation properties. Many properties of galaxies such as gas and dust content, metallicity depend on the star formation rate (SFR). Star formation changes cold and dark clouds into hot and bright stars, and the evolution of stars and consequent processes changes the whole composition of galaxies and also the universe. Understanding the star formation in galaxies is important for understanding the properties, formation, and evolution of galaxies. Therefore, it is necessary for us to understand the process of star formation and to determine the rate of it.

1.4.1 Basic conceptions about stars

Classification

Stars are classified according to their spectra or light curves. There are a few important classes of stars that are defined in terms of the light curve, such as novae and pulsars. Most stars are classified using the spectral classification. In spectral classification, stars that have spectra with similar structures are grouped together.

According to features of stellar spectra, stars are divided in to classes O, B, A, F, G, K and M. The physical properties of stars depend on the classes they belong to. For example, from O to M the temperature and mass of the star decrease in general. The metallicity of stars also changes accordingly from O to M classes. This dependence is because of the intrinsic connection between the physical properties of a star and the spectrum it generates. The spectral classes can be further divided into subclasses, which are expressed using decimal numbers 0 to 9 (e.g., A0, A1... and A9).

The luminosity (absolute magnitude) of a star gives another clue for classification. Stars can be divided into five groups, I (supergiants), II (bright giants), III (normal giants), IV (subgiants) and V (dwarfs), according to their luminosities.

The famous Morgan-Keenan (MK) system combines these two criteria and gives two-dimensional classification of stars. The class of a star in MK system is expressed using its spectral class plus its luminosity class. For example, the sun is classified G2V. Figure 1.4 gives an example for spectra of different MK types of stars.

Color-Magnitude diagram and stellar evolution

The color-magnitude relation of stars is essential in stellar astrophysics. The diagram of color-magnitude relation is called a Hertzsprung-Russell diagram (H-R diagram). Stars are distributed in several well defined sequences in the H-R diagram. In Figure 1.5, we can see that most of stars locate in a sequence running from lower-right to the upper-left. This sequence is called the main sequence. The positions of the stars on the main sequence are determined by their masses. Other sequences such as giants, bright giants, supergiants and white dwarfs are also shown in Figure 1.5.

Figure 1.4 An example of spectra from stars of different spectral types. Each spectrum is shifted vertically by an arbitrary amount in order to separate it from its neighbours (data are taken from Pickles (1998)).

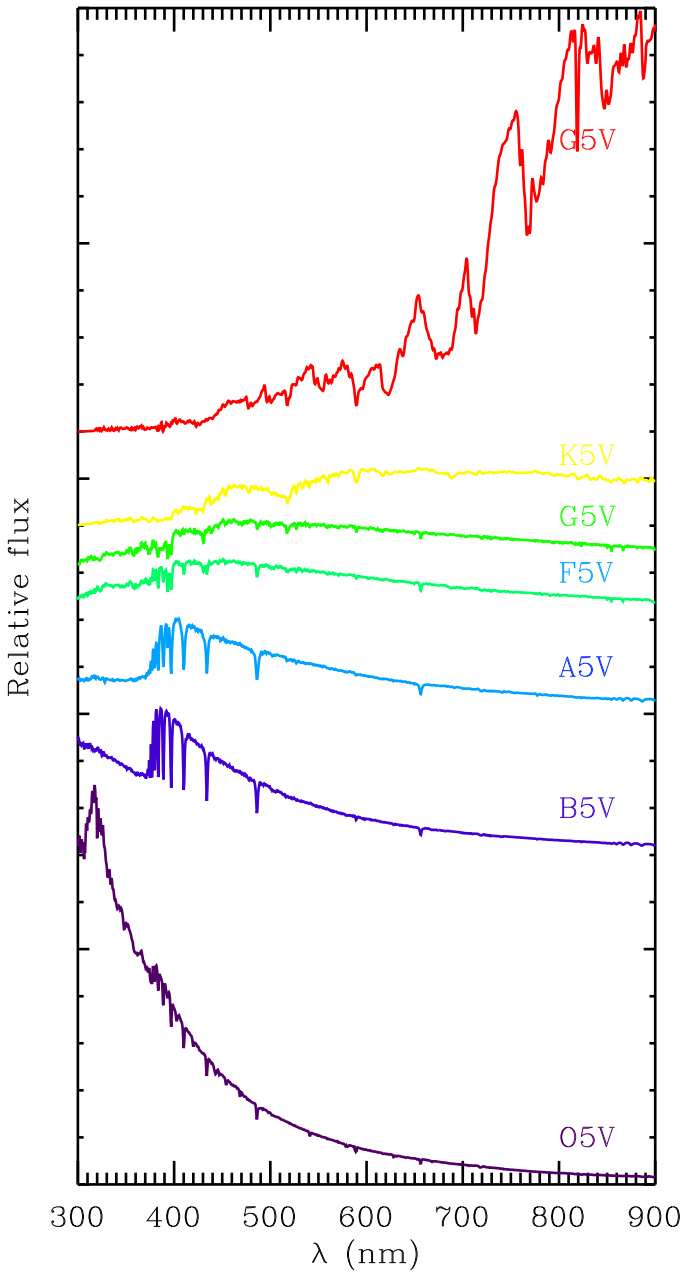

Figure 1.5 The H-R diagram. Taken from `http://en.wikipedia.org/wiki/Hertzsprung-Russell_diagram`.

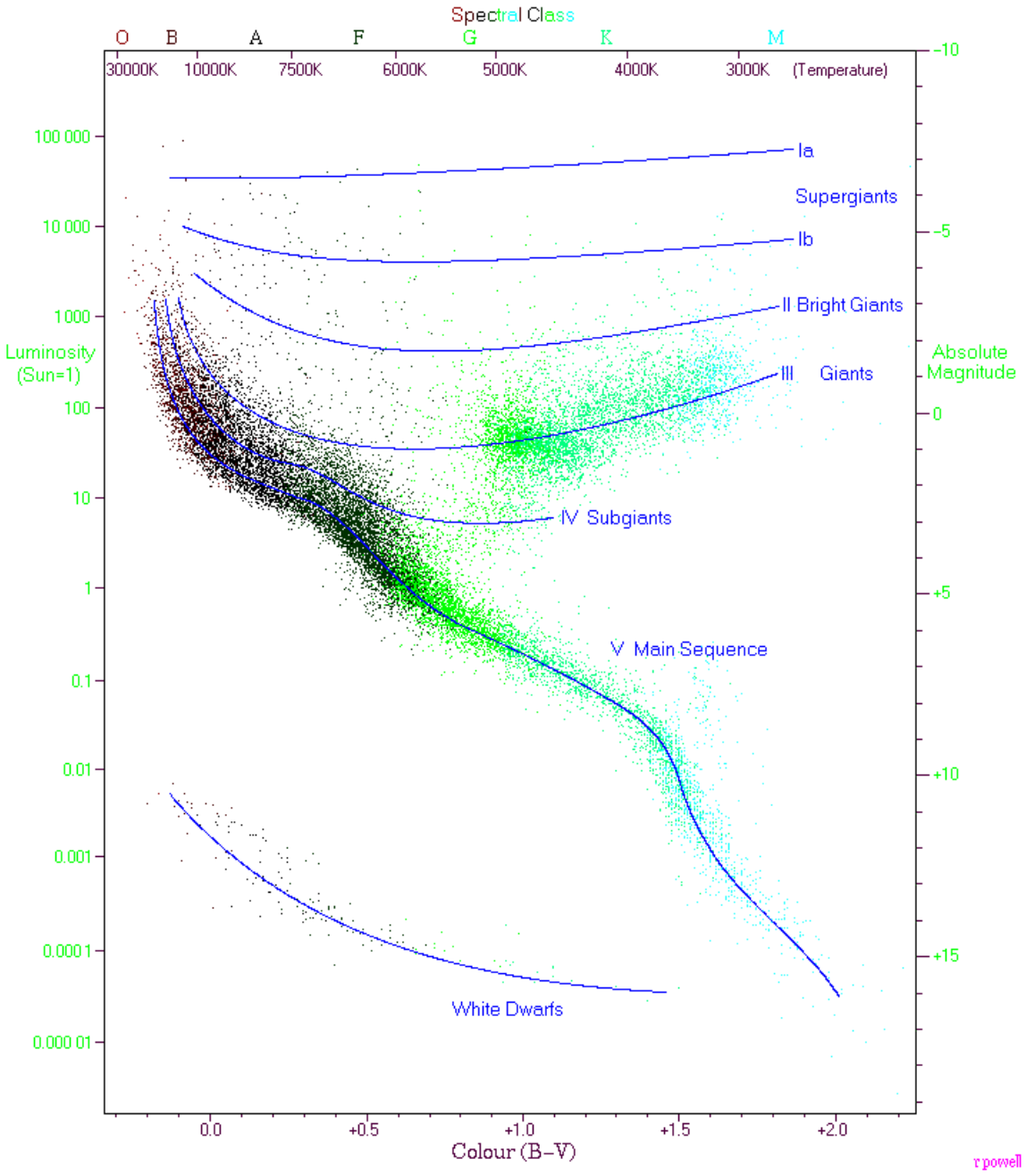

Figure 1.6 Sample stellar evolutionary tracks for single stars, zero initial rotational velocity, and solar metallicity, taken from `http://commons.wikimedia.org/w/index.php?title=File:Stellar_evolutionary_tracks-en-with-text.svg&page=1`.

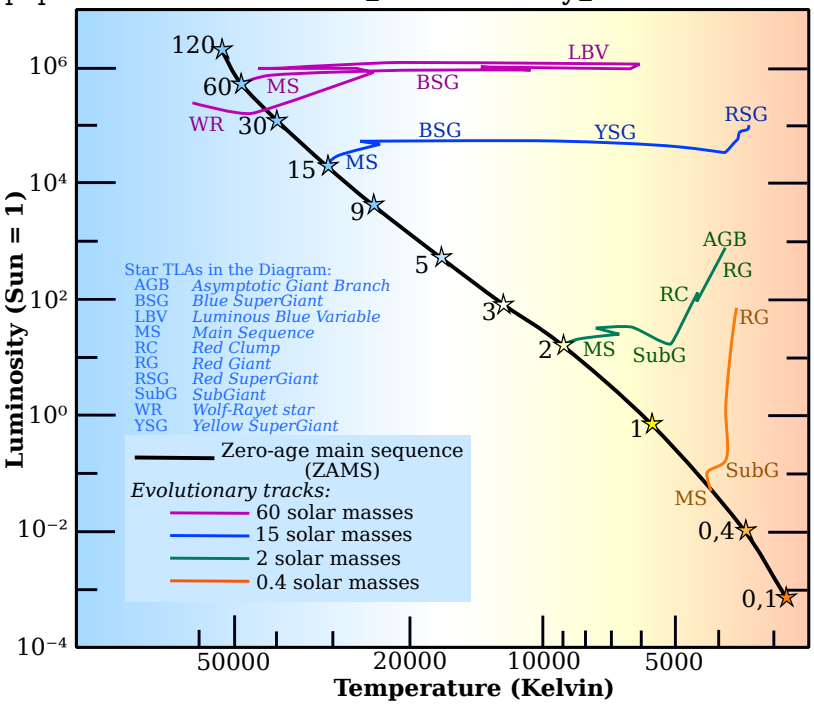

Stars evolves from main sequence to other positions in the H-R diagram. Figure 1.6 shows the evolutionary tracks of different masses of stars on the H-R diagram. In this figure, the color is substituted by the temperature, and the absolute magnitude is substituted by the luminosity. Figure 1.6 shows the evolution tracks of stars depend on their masses. The massive stars have distinct evolution from low-mass stars. Detailed calculations of stellar evolution models show that massive stars evolve faster than low-mass stars. The main sequence lifetime of a star scales roughly as M^{-3}.

1.4.2 The basic processes of star formation

Stars are born from the collapse of cold gas cloud. Studies show that giant molecular clouds (GMC) are the sites of star formation. The basic processes of the formation of individual stars contain the following steps:

1. The effects of turbulence and activity of new stars cause the density fluctuation

of the gas clouds. The higher density regions become "cores".

2. The protostars form as a result of the collapse of cores that are dense enough. The accretion disk forms and the bipolar outflows begin.

3. The mass is accumulated by the accretion, and reduced by the outflows.

4. when the protostar starts nuclear reaction, it becomes a real star. The accretion process is terminated by strong radiation (Mo et al. 2010).

However, there are still many open questions on the details of how stars form, especially for massive stars. A large amount of researches related to this topic are still in process. Considering the broad content of this topic, we omit the detailed discussion about the formation process. In this section we focus on introducing more global properties of star formation in galaxy-scale, which is better related to our research.

1.4.3 Kennicutt-Schmidt law

It has been already mentioned that we have a limited understanding of the physical process involved in the star formation. Therefore, theoretically it is hard to determine the relation between the mass in stars formed per unit time per unit area ($\dot{\Sigma}_*$) and the physical conditions of the interstellar medium (ISM). Nevertheless, from the observations astronomers can obtain empirical star formation laws to describe how $\dot{\Sigma}_*$ depends on certain properties of ISM.

Schmidt (1959) found a power law relation between $\dot{\Sigma}_*$ and the surface density of gas (Σ_{gas}):

$$\dot{\Sigma}_* \propto \Sigma_{gas}^N, \tag{1.16}$$

where N is around 2 with a variation between 1 to 3. Kennicutt (1998b) extended the study by including starburst galaxies in the analysis. The best fitting gives

$$\dot{\Sigma}_* \ = \ (2.5 \pm 0.7) \times 10^{-4} \left(\frac{\Sigma_{gas}}{\mathrm{M_\odot pc^{-2}}} \right)^{1.4 \pm 0.15} \mathrm{M_\odot yr^{-1} kpc^{-2}}, \tag{1.17}$$

and is referred as the Kennicutt-Schmidt law. This law relates SFRs with the properties of interstellar gas.

1.4.4 Star formation rate and its diagnostic method

The SFR in galaxies is not a directly observable quantity. Therefore, calculating SFRs in galaxies from observation data is very important. Because massive stars are short-lived ($\leq 10^8$ yr), the amount of the massive stars is directly related to the current SFR. On the other hand, low-mass stars can live in a long time, and thus it is difficult to distinguish between the young and the old low-mass stars. Therefore, we trace SFR by tracing the amount of massive stars. Through an empirical function that describes the distribution of initial masses for the population of stars (initial mass function, *abbr.* IMF, see also 1.6), we can then obtain the SFR.

Another advantage of massive stars is that they are hot and bright, and therefore it is easy to observe them. Emissions from massive stars can be converted into SFRs using the method of spectral synthesis (see 1.6). These emissions are used as SFR indicators. A review of these indicators can be found in Kennicutt (1998a). Here we summarize the most important indicators.

1. **UV continuum** UV emission is dominated by young massive stars. Therefore, the emission is directly related to the star formation rate. The optimal range of wavelength to trace SFR is $1250 \sim 2500$ Å, which is longer than the Lyα forest that absorbed largely by interstellar medium, and shorter enough to avoid the contamination from the emission of old stellar populations.

   The advantages of UV continuum are that it is directly related to the photospheric emission of young, massive stars and it can be applied to galaxies for a wide range of redshifts. However, this indicator is sensitive to the correction of dust extinction and the assumption of IMF, and therefore the uncertainties of the calculated SFR are relatively large.

2. **Recombination Lines** Lyman continuum photons produced by young massive stars can ionize the gas surrounding the stars. Then the ionized gas can

re-emit the energy in the form of Hydrogen recombination lines. Therefore, the strength of these lines can be a good indicator of SFRs. The most frequently used line is the Hα line. Other lines, such as Hβ, Pα, Pβ, Brα and Brγ are also used.

Since only stars with masses of $> 10\ M_{\odot}$ and lifetimes of less than 20 Myr contribute significantly to the integrated flux of ionization, the recombination lines are directly coupling with the massive SFR. Another advantage of using the recombination lines is the high sensitivity of the observations. The limitation of this method is also due to the uncertainties of extinction and the IMF.

3. **Forbidden lines** [OII]λ3727 forbidden-line doublet can also be used as a tracer of SFRs. Although the excitation is sensitive to the metal abundance and the ionization state of the gas, and thus the luminosities of these emissions are not directly related to the ionizing luminosity, the [OII] emission is found to behave well when tracing the SFR.

   [OII] is preferred for optical observations when the object is at redshift $z > 0.5$, where the Hα line moves out of the visible window. [OII] is less precise than Hα, and may also have considerable uncertainties due to dust extinction and variations in the diffuse gas fraction.

4. **FIR continuum ($8 \sim 1000\ \mu$m)** Dust absorbs photons at short wavelengths (UV and optical), and re-emits them into IR bands. The ISM surrounding young massive stars can be quite dusty. Therefore, UV photons emitted by the stars can be efficiently absorbed by the dust. Therefore, IR emissions can be a fairly good tracer of SFRs, especially for starburst galaxies, which are thought to be very dusty.

   Using IR emission can effectively reduce the sensitivity to the correction of dust extinction. However, there are still limits for this indicator. An important limitation is that the IR emission can also be due to cirrus emission, which is not related to SFR, but due to the emission of more extended dust heated by the interstellar radiation field produced by old stellar populations.

5. **Radio continuum** Radio emission can also be used to trace star formation rate. The connection between centimeter radio emission and star formation can be seen from similar morphology between Hα maps and radio maps in individual galaxies and the tight correlation between far-IR and 6-20 cm fluxes for various galaxies. The connection is not as direct as other indicators we mentioned before. The radio spectra of these systems are not flat, thermal free-free spectra of individual HII regions, but nonthermal such as in synchrotron radiation. Therefore, these emissions are dominated by supernova remnants which are generated by the death of massive stars, and hence the radio emissions trace SFR by tracing the supernova rate.

   With the very high ability of VLBI (Very-Long BaseLine) and VLA (Very Large Array) radio observations, radio emissions are good tracers of the SFR. However, when the galaxy is very distant, the emissions will move to longer wavelengths, and make the observation difficult.

Combinations of different indicators are also used to calculate SFRs (e.g. Buat & Xu 1996; Meurer et al. 1999; Gordon et al. 2000; Buat et al. 2005; Kennicutt et al. 2009, see also Chapter 4). To find a well-behaved SFR tracer is still a task remaining to be completed. In Chapter 2, we will discuss the SFR tracers again.

1.5 Multiwavelength observation

Since galaxies contain several components radiating the bulk of their energy at different wavelengths, galaxies present quite distinct features at different bands of observations (Figure 1.7). Therefore, it is necessary to use multiwavelength data to have a panoramic view of galaxies.

Nowadays, with the advancement of techniques, more and more data are obtained at different wavelengths. Here we give an introduction to observations that are related to this thesis from UV to IR.

After IUE and FUSE, the Galaxy Evolution Explorer (GALEX) now is the major source of UV data. GALEX provides images in the near-UV (NUV) and far-UV

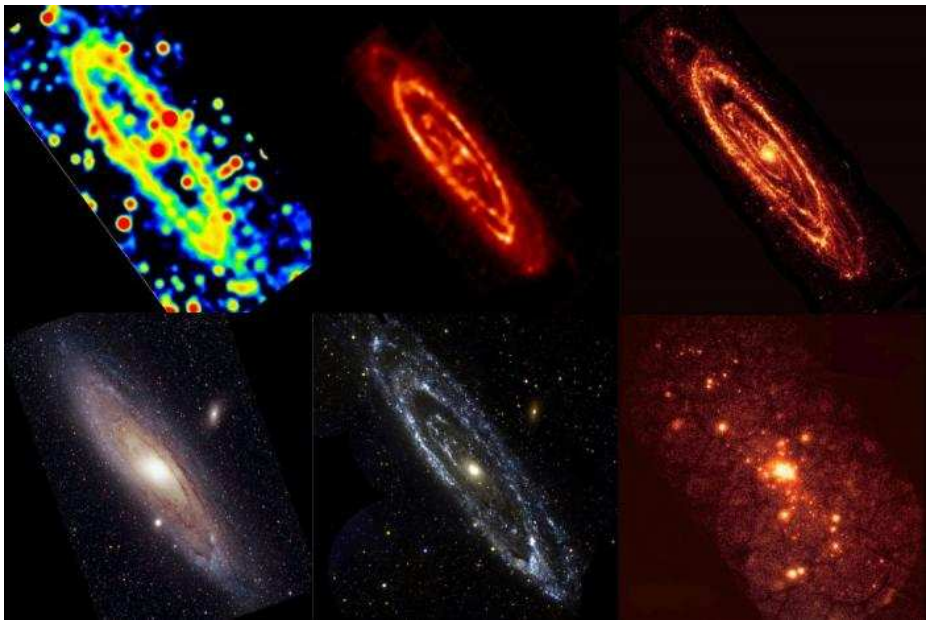

Figure 1.7 The multiwavelength view of M31 (the Andromeda Galaxy), taken from the website: `http://thebeautifulstars.blogspot.jp/2011/08/multi-wavelength-views-of-stuff.html`

(FUV) using microchannel plate detectors, and also provides low resolution spectroscopy using a grism. GALEX imaging studies include the Nearby Galaxy Survey (NGS), Deep (DIS), Medium (MIS), and All Sky Surveys (AIS: imaging). The GALEX AIS covers more than 2/3 of the sky. The data can be retrieved via the GALEX website (`http://galex.stsci.edu/GR6/`).

Sloan Digital Sky Survey (SDSS) is one of the most important sources for optical observation. SDSS covers more than 1/4 of the sky and obtained deep, multi-color images. The telescope has five bands, u, g, r, i, z, covering wavelengths from $\sim$ 3500Å to $\sim$ 9000Å. SDSS provides numerous spectral and image data of quasars, stars and galaxies. These data have been widely used in studies on formation and evolution of galaxies.

IR observations are of essential importance for nowadays astronomy. The Two Micron All Sky Survey (2MASS) provides near-IR (NIR) data at J-, H- and K_s-bands with a coverage of $\sim$70% of the sky. At mid-IR (MIR) and far-IR (FIR) bands,

the Infrared Astronomical Satellite (IRAS) carried out the first all sky survey (> 96% sky coverage). The IRAS survey provides numerous data at 12, 25, 60 and 100 μm. The AKARI mission attempted to make an all-sky survey with a much better sensitivity, spatial resolution and a wider wavelength coverage than IRAS. It provides MIR all-sky survey data at 9 and 18 μm (InfraRed Camera, IRC), and FIR all-sky survey data at 65, 90, 140 and 160 μm (Far-Infrared Surveyor, FIS). The Spitzer Space Telescope achieved higher sensitivity and resolution at IR bands. It contains three instrumnents, the InfraRed Array Camera (IRAC), the InfraRed Spectrograph (IRS), and the Multiband Imaging Photometer (MIPS). IRAC provides imaging capabilities at 3.6, 4.5, 5.8 and 8 μm, IRS provides both high- and low- resolution spectroscopy at MIR wavelengths, and MIPS provides imaging and limited spectroscopic data at FIR wavelengths (24, 70, 160 μm). A recent MIR survey is carried out by the Wide Infrared Survey Explorer (WISE). WISE has very high sensitivity and spatial resolution at MIR bands. It provides a huge amount of data at its 3.4, 4.6, 12, 22 μm bands. The survey is still continuing, and more data are expected to be released soon. Herschel, Europe Space Agency's giant infrared observatory, is equipped with a large telescope (prior mirror has a diameter of 3.5 m). Herschel covers the wavelength from 55 to 672 μm, and thus it will give very important information of the IR sky. Although we do not use Herschel data in the present study, the importance of Herschel must be stressed here. Its data will be used in our future study on mergers and high redshift galaxies.

1.6 Spectral Energy Distribution fitting

The distribution of energy (i.e. luminosity) over wavelengths is called the spectral energy distribution (SED). Figure 1.8 shows an example of a galaxy SED. The UV data are from GALEX, optical data are from SDSS, NIR data are from 2MASS, MIR data are from AKARI/IRC, and FIR data are from AKARI/FIS.

The information of the physical properties of a galaxy can be obtained from the SED we observe. However, the information the SED contained is highly degenerated. To understand these properties, we need to fit the SED using model predictions.

Figure 1.8 Example of galaxy SED. Blue dots are observation data from UV to FIR by GALEX, SDSS, 2MASS and AKARI, red line is the best fit for the data.

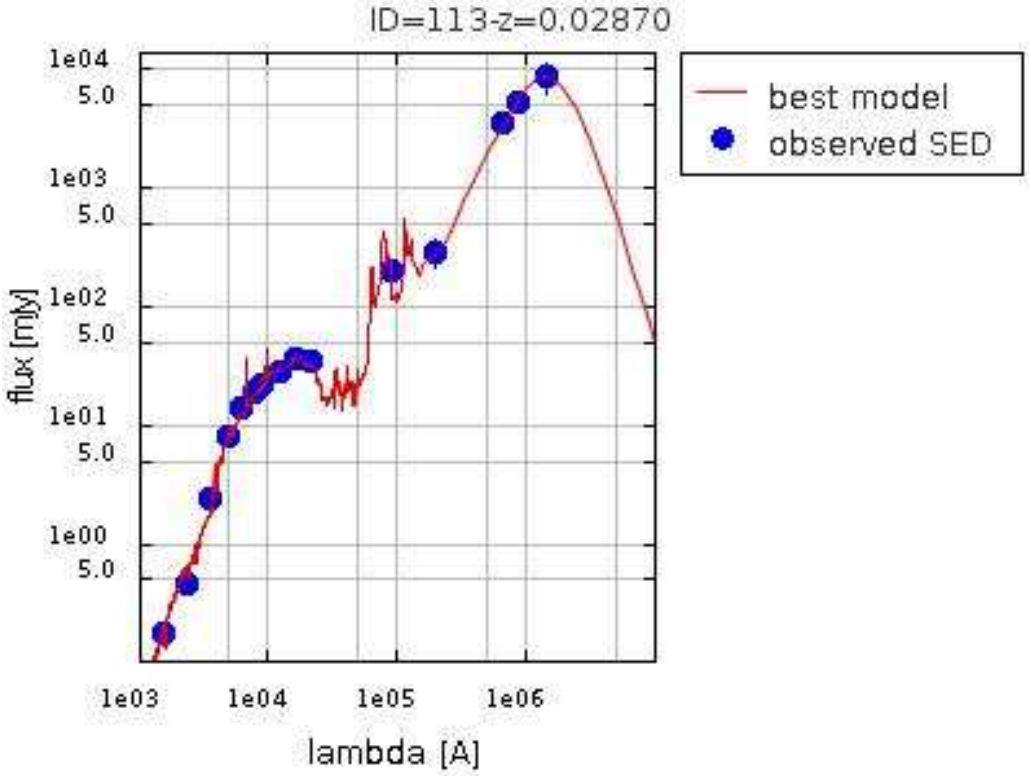

With the improvement of the ability of telescopes and computers, we can obtain many physical properties, such as star formation rate, stellar mass, etc., in high precision from SED fitting. Here we introduce the basic concepts and method used in SED fitting. More detailed information can be found in Walcher et al. (2011).

1.6.1 Modeling

Galaxies are composed of stars, gas, dust, dark matters, etc. We first consider stars, which are the major source of light of galaxies except active galactic nuclei (AGNs).

Stellar population synthesis

The technique to construct galaxy SED models is based on the stellar population synthesis. As we mentioned in Section 1.4.4, a group of stars born at the same time will have an initial mass distribution, which can be described by IMF $\phi(M)$. This group of stars evolve, and at time t after they are born, the luminosity of this group $L_\lambda(t)$ can be obtained by integration:

$$L_\lambda(t) \;=\; \int \phi(M) L_\lambda(M,t)\,\mathrm{d}M, \tag{1.18}$$

where $L_\lambda(M,t)$ is the SED of a star with an initial mass M at age t.

The IMF $\phi(M)$ is still a topic under debate. There are several forms of IMFs, such as Salpeter IMF (Salpeter 1955), Kroupa IMF (Kroupa 2001), Chabrier IMF (Chabrier 2001), etc.. In this thesis, we are going to use two of these IMFs. One is Salpeter IMF, the other is Kroupa IMF.

Salpeter IMF has a simple power-law form

$$\phi(m)dm \propto m^{-2.35}, \tag{1.19}$$

Kroupa IMF has a broken power-law form,

$$\phi(m) \propto \begin{cases} m^{-2.3} & (0.5M_\odot < m < 100M_\odot) \\ m^{-1.3} & (0.1M_\odot < m < 0.5M_\odot) \end{cases}$$

To compute $L_\lambda(M,t)$, i.e., the SEDs of stars at time t, a library of stellar spectra is necessary.

These spectra can be either theoretical or empirical. Both have pros and cons. The empirical approach uses observed stellar spectra from the Solar neighborhood. These spectra avoid complicated modeling of the structure of the atmosphere and have small uncertainties. However, the parameter space covered is limited. On the other hand, the theoretical approach uses stellar atmosphere models to construct stellar spectra, and these theoretical spectra cover a large parameter space and can achieve any resolution required, but there are still problems such as the incomplete line lists (Kurucz 2005), the modeling of the IR emission (Lançon et al. 2007), etc.

If there were only stars in galaxies, the luminosity of a galaxy at time t would be the sum of luminosities of all stars with different ages:

$$L_\lambda^{gal}(t) \;=\; \int_0^t \Psi(t')L_\lambda(t-t')\;\mathrm{d}t', \tag{1.20}$$

where $\Psi(t')$ is the star formation rate at time t'.

However, in galaxies there are not only stars but also interstellar medium(ISM), which can absorb and re-emit emissions from stars and change the form of the spectra. Therefore, the ISM, namely gas and dust, must be considered when modeling the galaxy spectra.

Gas

The gas component considered in the SED fitting is atomic gas. The contribution of molecular gas to the SED of a galaxy is not significant (Young & Scoville 1991; Hollenbach & Tielens 1997). On the other hand, atomic gas is rather important in the case of young, actively star-forming galaxies. It absorbs high energy photons at extreme-UV (EUV) bands and re-emits them at UV, optical and IR bands in the form of recombination lines.

Dust

Dust absorption and emission can change the form of an SED substantially. Dust absorption causes two effects: the reddening and the obscuration. The reddening can

be quantitatively described using the color excess $E(B-V)$ or the Balmer decrement Hα/Hβ. The obscuration is expressed as A_V. The amount (obscuration) and wavelength dependence (reddening) of dust absorption can be described by the attenuation law. The attenuation law has been calculated in empirical and theoretical approaches. The empirical calibrations are convenient in use, whereas these calibrations overlook the details (e.g. Calzetti et al. 1994; Calzetti 1997; Charlot & Fall 2000). The theoretical calibrations, on the other hand, use radiative transfer (RT) code and thus are more close to the true physical process (e.g. Bruzual A. et al. 1988; Ferrara et al. 1999; Pierini et al. 2004; Tuffs et al. 2004). However, the RT code uses too many free parameters which are hard to determine when we only have broad-band SEDs. In SED fitting with only broadband photometry data, the simple attenuation law empirically obtained is preferred.

In this thesis, we use a modified Calzetti Law. The illustration of this attenuation law is shown in Figure 1.9. The original Calzetti Law has the form

$$\begin{aligned} k(\lambda) = 2.659(-2.156 + 1.509/\lambda - 0.198/\lambda^2 + 0.011/\lambda^3) + R_V, \\ \text{when} 0.12 \leq \lambda \leq 0.63\ \mu\text{m}, \\ k(\lambda) = 2.659(-1.857 + 1.040/\lambda) + R_V, \\ \text{when} 0.63 \leq \lambda \leq 2.2\ \mu\text{m}, \end{aligned} \tag{1.21}$$

where $R_V = 4.05$.

This attenuation law is modified by changing the slope of this relation by a factor of $(\lambda/5500\text{Å})^\delta$. The attenuation curves for $\delta = 0.3$ and $\delta = -0.3$ are shown in Figure 1.9.

Dust emits the absorbed energy at longer wavelength (i.e. IR). The dust emission is commonly modeled using blackbody or greybody spectrum. In the simplest model, dust achieves thermal equilibrium and has only one temperature. More complicated and realistic models assume that small grains are heated stochastically and have a certain temperature distribution. The mass of dust is also needed in order to calculate the total emission. The mass is often given by $\mathrm{d}M = f(U)\,\mathrm{d}U$, where $f(U)$ is a function of the radiation field intensity U, and is usually assumed to have a power-law form $f(U) \propto U^\alpha$. Practically, the IR emission is hard to predict by the simplified

Figure 1.9 Illustration of the modified Calzetti law.

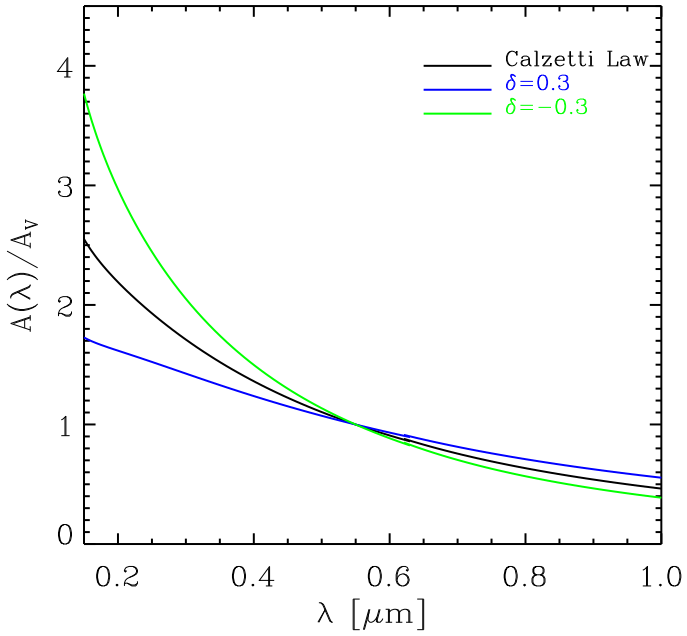

theory, and the empirical templates are often used. Those of Chary & Elbaz (2001); Dale & Helou (2002); Lagache et al. (2004), and Rieke et al. (2009) are examples of well known templates.

Contributions from stars and dust need to be combined to give the whole SED model of a galaxy. The simplest solution is to assume that the energy that the dust emitted is just the energy it absorbed. Then, from the attenuation law and the IR emission model, the stellar and dust emission can be related. Figure 1.10 gives an example of this connection. We can see that when attenuation A_V increases, the short wavelength part of spectra becomes fainter, while the infrared part which is contributed by dust emission becomes brighter.

This way is quite efficient to compute the SEDs, but it must be stressed that since it only balances the total amount of energy, it does not constrain the physical properties such as dust temperature directly by the optical-UV absorption in the model. More realistic and complicated way is using the radiative transfer calculation to compute the details of absorption and emission.

Figure 1.10 Illustration of the connection between dust attenuation and emission. When the A_V becomes higher, the flux of the UV and optical becomes lower, while the flux of IR part becomes higher. This figure is taken from Noll et al. (2009).

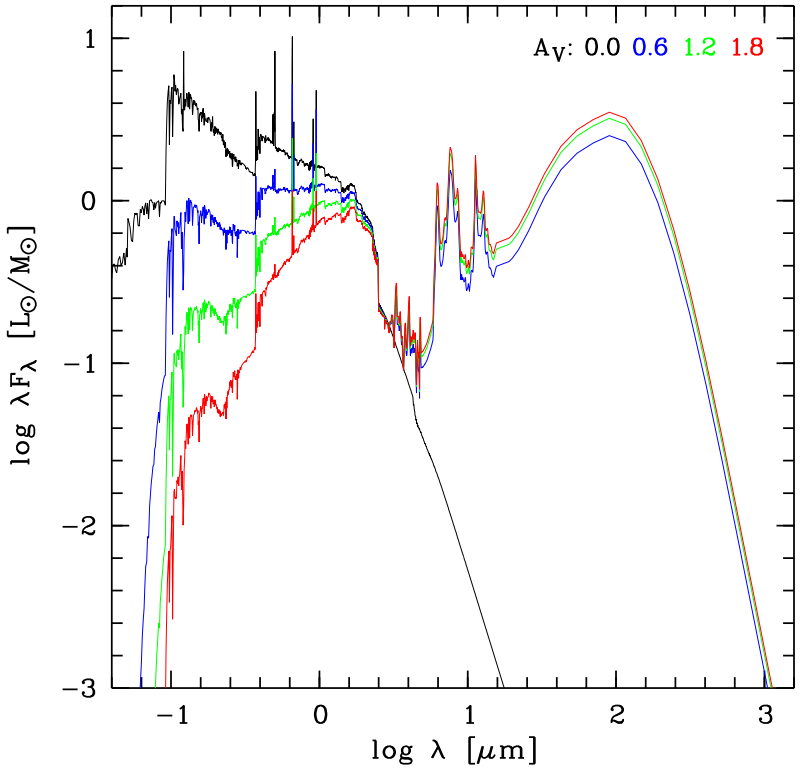

After the combination of the stellar and dust emission, the galaxy SED models are built.

1.6.2 Methods of SED fitting

From the models, the observed SEDs of galaxies can be fitted to obtain the physical parameters. This is a process reverse to construction of SED models. The commonly used method is Bayesian inference. Assuming that the data are randomly drawn from a distribution that is a member of a model family characterized by a parameter vector $\mathbf{P}$, what we want to know is the likelihood of a particular value of parameter $\mathbf{P}$ given the observed data. In statistics, this is the posterior probability density function $f(\mathbf{P}|\mathbf{d})$, i.e., the probability of parameter $\mathbf{P}$ given observed data $\mathbf{d}$. In Bayesian statistics, this probability can be calculated by

$$f(\mathbf{P}|\mathbf{d})\,\mathrm{d}\mathbf{P} \;\propto\; f_p(\mathbf{P})Pr(\mathbf{d}|\mathbf{P})\,\mathrm{d}\mathbf{P}, \tag{1.22}$$

where $f_p(\mathbf{P})$ is the prior probability distribution, i.e., the probability of $\mathbf{P}$ without any condition. $Pr(\mathbf{d}|\mathbf{P})$ is the likelihood, i.e., the probability of the data observed given the parameter $\mathbf{P}$. Practically, $f_p(\mathbf{P})$ is usually assumed to be a flat distribution. $Pr(\mathbf{d}|\mathbf{P})$ can be calculated using χ^2 method assuming Gaussian uncertainties: $Pr(\mathbf{d}|\mathbf{P}) \propto e^{-\chi^2/2}$. The χ^2 of model i is given by:

$$\chi_i^2 = \sum_X \left[\frac{F_{obs,X} - a_i F_{mod_i,X}}{\sigma(F_{obs,X})}\right], \tag{1.23}$$

where $F_{obs,X}$ is the observed flux at different wavelengths X, and $\sigma(F_{obs,X})$ is its error. a_i is scale factor making the model closest to the data. Practically, fluxes of models have some arbitrary zero point, therefore, the scale factor a_i should be decided first by minimize the χ^2 for the model. The best matches a_i^* can be derived by

$$a_i^* = \sum_X \left[\frac{F_{obs,X}F_{mod_i,X}}{\sigma^2(F_{obs,X})}\right] \Big/ \sum_X \left[\frac{F_{mod_i,X}}{\sigma(F_{obs,X})}\right]^2. \tag{1.24}$$

After the a_i^* is obtained, the χ_i^2 for each model can be derived, and then the likelihood of each model is obtained. From the likelihood, we can derive the best

estimate and confidence interval for any model property $Y(\mathbf{P})$. The likelihood of the parameter we are interested in is given by

$$f(Y|\mathbf{d}) \;=\; \int_Y f(\mathbf{P}|\mathbf{d})\,\mathrm{d}\mathbf{P}. \tag{1.25}$$

The most probable value of Y can be estimated as the value at the peak of this distribution, the most typical value of Y can be taken as the median value of this distribution, and the 95% confidence interval for Y can be defined by excluding 2.5% tails at each end of the distribution. More details about the Bayesian inference in this context can be found in Kauffmann et al. (2003) and Salim et al. (2007).

There are many codes that deal with SED fitting, using different models and methods. The SED fitting code we used will be introduced in Chapters 2 and 3.

1.7 The Cosmic Star Formation History

After we obtain SFR of galaxies at different redshifts, the cosmic star formation density at redshift z can be calculated by

$$\dot{\rho}(z) \;=\; \int \langle \mathrm{SFR} \rangle(L,z)\,\phi(L,z)\,\mathrm{d}L, \tag{1.26}$$

where $\langle \mathrm{SFR} \rangle(L,z)$ is the average star formation rate for galaxies with luminosity L at redshift z. $\phi(L,z)$ is the luminosity function at redshift z. The luminosity function $\phi(L)$ is defined as

$$\phi(L) \;=\; \mathrm{d}n(L)/\mathrm{d}L, \tag{1.27}$$

where $\mathrm{d}n$ is the comoving number density of galaxies with luminosity between L and $L + \mathrm{d}L$. The luminosity function is commonly fitted by a Schechter function (Schechter 1976) with the form

$$\phi(L)\mathrm{d}L = \phi^* \left(\frac{L}{L^*}\right)^{\alpha} \exp\left(\frac{L}{L^*}\right) \frac{\mathrm{d}L}{L^*}, \tag{1.28}$$

where L^* is a characteristic luminosity that separates the low and high luminosity part. At the faint end ($L < L^*$), the relation approximates a power law, and $\phi(L)$ is proportional to L^{α}. The parameter α gives the slope of this power law, and has the

Figure 1.11 SFR at different redshift traced by different SFR indicators, taken from Borch et al. (2006). The data are adapted from Hopkins (2004). The stellar IMF has been adjusted to be consistent with Chabrier (2003). The lines show different assumptions for the evolution of the cosmic star formation history and the associated growth of cosmic stellar mass: the dotted line shows the fit optimized to reproduce the growth of stellar mass, the dashed line fits the star formation rate better, and the solid line is a reasonable compromise between the two.

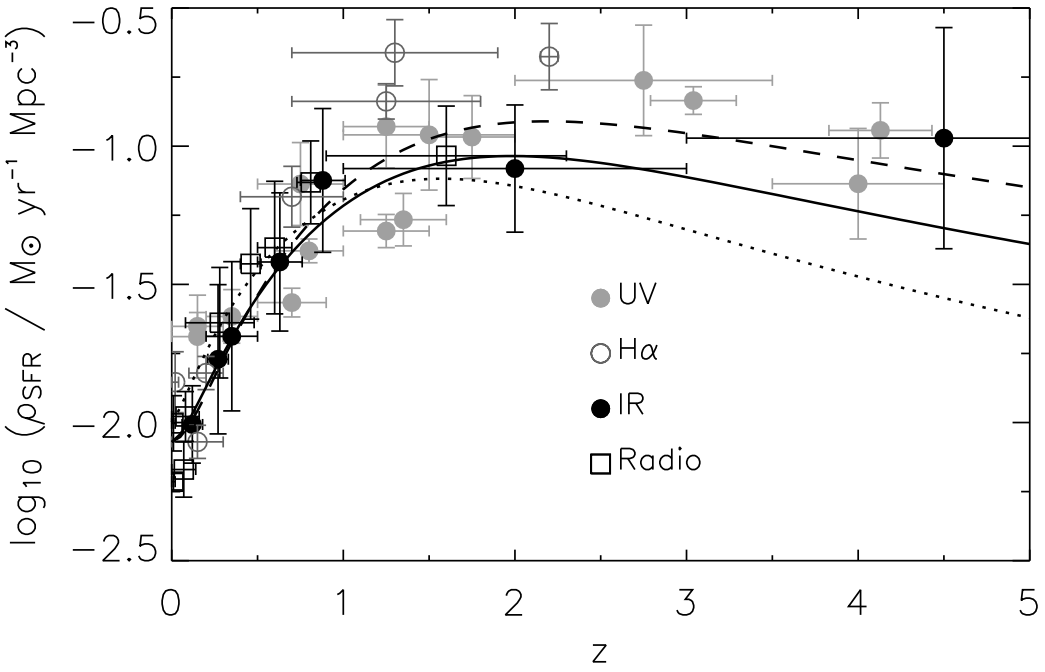

value between -0.8 and -1.3. At the bright end ($L < L^*$), the relation approximates an exponential form, $\phi(L) \propto e^{-L}$. The parameter ϕ^* is an overall normalization.

Figure 1.11 shows the cosmic star formation rate at different redshifts traced by different SFR indicators. The cosmic SFR is very important for the studies on the structure formation and galaxy evolution. Through investigating the different SFRs at different distance, we can look into how the stellar mass of galaxies are built at different cosmological time, and then understand the formation process of the observable universe.

It has been well established by now that the cosmic star formation rate has dropped by roughly an order of magnitude from $z \sim 1 - 2$ to the present epoch. The origin of the cosmic star formation history can be explained using CDM galaxy formation senario and a simple star formation model (Mo et al. 2010). However, the details of the mechanism that drives the evolution are still under debate. Merger process can induce gas in the galaxies center and increase the SFR in galaxies. Therefore, if the merger induced SFRs are the main contribution to cosmic SFRs at redshift $z \sim 1$, and the merger rate is reduced from then to present epoch, then the change of merger rate may be the reason of the SFR dropping. However, whether this is true still remains to be solved. We will come back to this topic again in Chapter 4.

Another question about the cosmic star formation rate is related to accumulation of stellar mass. The star formation rate history should be consistent with the stellar mass assembly. However, astronomers found discrepancy between these two. In Figure 1.11, the dotted line is derived from stellar mass at different redshift, and the dashed line is the best fit for the cosmic star formation rate. We can see clear difference between these two lines, especially at the high redshift end. One of the causes of this difference may due to the inaccurate calculation of SFRs. From Figure 1.11, we can see that the SFRs are calculated by different indicators. These SFRs have large uncertainties and are not uniform at different redshifts. For high redshifts ($z > 1$), there are almost only IR and UV derived results, and the discrepancy between them is quite significant. Therefore, to understand the discrepancy between stellar mass assembly and SFRs, we should first improve the measurement of the SFR.

Investigating SFRs also help us understand the feedback process of galaxy for-

mation. If the cooling mechanism is efficient, the theory of galaxy formation gives much more masses of stars as it is presented now. Therefore, there must be certain mechanisms which stop the star formation activity. Possible mechanisms include the supernova feedback and AGN feedback. Since the consequences of star formation, gas content, supernova rate, and AGNs are entangled with each other, calculating SFRs is necessary to quantitatively study the feedback processes.

Measuring the SFR is also important for understanding the reionization of the universe. Figure 1.2 shows that the early universe was once in a neutral state. However, now the intergalactic medium of the universe is mostly ionized. Therefore, there must be some mechanism which caused the reionization of the universe. The ionized photons generated by star formation activity and escaped from the galaxies are thought to be a dominant source for reionization. However, there are also optional mechanisms such as the collapsing of materials onto early black holes that power AGNs and decaying elementary particles (Robertson Brant E. et al. 2010). Therefore, it is necessary to find out how much the photons from star formation contribute to the reionization. In this sense, an accurate measurement of SFR is also dispensable.

1.8 Structure of this thesis

The goal of this thesis is to use the GALEX-SDSS-2MASS-AKARI multiwavelength sample to study the star formation and dust attenuation of galaxies. In the first part of this research (Chapter 2 and 3) we attempt to built more accurate SFR calibrations, and in the second part (Chapter 4) we study the dust attenuation in major merger galaxies and their contribution to local SFR density. The structure of this thesis is as follows:

Chapters 2 and 3 introduce the work on mid-infrared star formation rate indicators. In Chapter 2, we first introduce the method of constructing the multiwavelength sample. Then, we correct the AKARI FIS catalogue data using diffuse maps. The SED fitting code CIGALE is also introduced in this Chapter. We present SFR calibrations using AKARI/IRC mid-infrared data and compare the results with those derived from Spitzer data. The influence of inclusion of UV emission when calculating

SFRs, and the calibrations for AGNs are also discussed.

Chapter 3 presents our work on Wide Infrared Survey Explorer (WISE) bands. We applied the data used in Chapter 2 to construct models to investigate the correlation between WISE bands and star formation rate from local to higher redshift universe. The model predictions are compared with results based on real data and with previous studies.

Chapter 4 focuses on the work about local major merger galaxies. This work applies results from (Buat et al. 2011), which is based on the same multiwavelength sample. We investigate the star formation and dust attenuation of major mergers from both UV and IR views in this chapter.

Chapter 5 summarizes our work and presents our future researches.

Chapter 2

AKARI/IRC MIR luminosities as SFR indicators

2.1 Introduction

The star formation activity is fundamental for the studies on the formation and evolution of galaxies. Numerous efforts have been made to find reliable and convenient SFR indicators so far (e.g. Kennicutt 1998a; Hirashita et al. 2003; Bell 2003; Hopkins et al. 2003; Calzetti et al. 2007). Among most frequently used indicators, the ultraviolet (UV) and the optical recombination lines (e.g. Hα, Paα) give direct measures of light from young stars. However, UV and Hα emissions are strongly affected by dust extinction (Kennicutt 1998a), and Paα as well as other optical recombination lines were also shown to underestimate SFRs for luminous galaxies (Rieke et al. 2009). On the other hand, since dust absorbs UV/optical light and re-emits the bulk of the energy at the far-infrared (FIR) band (25 μm $\sim$ 350μm), FIR emission efficiently traces SFR for dusty galaxies. However, FIR emission is unable to trace the dust-unobscured radiation and includes part of dust emission heated by old stellar populations. Therefore the energy balance method combining the FIR and UV derived SFRs were induced to complement the emission from young stars not traced by FIR (e.g. Buat & Xu 1996; Gordon et al. 2000; Buat et al. 2005). Although this method could trace SFRs with considerable accuracy, it is difficult to obtain the total

dust emission especially for high redshift objects since the wavelength range of dust emission is quite wide (see Figure 1.8).

The MIR monochromatic fluxes are also investigated as SFR indicators. The MIR emission is contributed by several components, including the polycyclic aromatic hydrocarbon (PAH) features (prominent at 6.2, 7.7, 8.6, 11.3, 12.7 and 17 μm), the continuum from the stochastic heating of very small grains, silicate absorption at 9.7 and 18 μm, molecular hydrogen lines and fine-structure lines (Leger & Puget 1984; Leger et al. 1989; Desert et al. 1990; Draine & Li 2007; Smith et al. 2007b; Treyer et al. 2010). The MIR-SFR relation was intensively studied using Spitzer IRAC 8 μm and MIPS 24 μm photometry data and spectral data (Förster Schreiber et al. 2004; Calzetti et al. 2005, 2007; Kennicutt et al. 2009; Rieke et al. 2009; Treyer et al. 2010). Nevertheless, there is still a debate on the reliability of MIR indicators because of the complicated features it contains. Attempts to combine the optical and IR indicators show that this combination could trace the SFR effectively, and notably reduce the scatter (e.g. Calzetti et al. 2007; Zhu et al. 2008; Kennicutt et al. 2009). However, factors of the combination are different in each work.

The AKARI/IRC Point Source Catalogue Version β-1 (hereafter IRCPSC) provides positions and fluxes of all-sky survey at *S9W* (9 μm) and *L18W* (18 μm) bands (Ishihara et al. 2010). For numerous MIR data, it would be useful if there is a benchmark of SFR measurement. Comparing with Spitzer 8 and 24 μm bands, the AKARI IRC *S9W* and *L18W* bands cover wider wavelength ranges, including silicate absorption features at both bands and emission contributed by large PAH molecules at the *L18W* band.

This part of the thesis is dedicated to investigate whether and to what degree AKARI broadband MIR data could trace the SFR, and how strong the inclusion of silicate absorption and longer wavelength PAH features would be.

Starting from a sample with multi-wavelength observed flux, we derive the SFR for each galaxy by the spectral energy distribution (SED) fitting. MIR data were correlated with the SFRs to built the SFR calibrations. Then the results were compared with those from the Spitzer observations. The present chapter is organized as follows: Section 2.2 introduces the GALEX-SDSS-2MASS-AKARI sample. Section 2.3 gives

a short introduction to methods for calculating the SFR. The MIR-SFR relations and some comparisons between AKARI and Spitzer are reported and discussed in Section 2.4. Conclusions are given in Section 2.5.

2.2 Data

2.2.1 Construction of the multi-wavelength sample

Far Infrared Selection

The parent sample is selected at FIR bands using the AKARI/FIS Bright Source Catalog (hereafter FISBSC) data (Yamamura et al. 2009), (Yamamura 2008) and IRAS-PSCz (Saunders et al. 2000) data. We start from AKARI FISBSC.

- **AKARI satellite** AKARI(ASTRO-F) is designed to carry out the second generation all-sky surveys after IRAS. AKARIs telescope is Richey-Chretien system. The focal length is 4200 mm and effective aperture is 68.5 cm. The telescope is cooled to 6K. It is composed of a primary mirror made of SiC with an effective diameter 67cm, a secondary mirror, trusses, and baffles which prevent stray light.

  The telescope is equipped with two imaging instruments, the FIS (Far-infrared Surveyor) (Kawada et al. 2007) for far-IR observations and the IRC (Infrared Camera) (Onaka et al. 2007) for near- and mid-IR observations. FIS has continuous spectral coverage from 50 to 180 μm with its four photometric bands: *N60* (65 μm), *WIDE-S* (90 μm, *WIDE-L* (140 μm) and *N160* (160 μm)). IRC is composed of three independent camera systems. The NIR camera (bands: *N2, N3, N4*) is assigned to near-infrared wavelengths in the 1.7-5.5 μm range. The MIR-S camera (bands: *S7, S9W, S11*) is assigned to shorter mid-infrared wavelengths over the 5.8-14.1 μm range. The MIR-L camera (bands: *L15, L18W, L24*) is assigned to longer mid-infrared wavelengths of 12.4-26.5 μm.

FISBSC contains 64311 sources using 90 μm band as the reference for the source detection. It provides the data about a huge amount of FIR sources, with wider

wavelength coverage and better resolution than IRAS.

We need to separate galaxies from other objects to obtain a pure galaxy catalog, considering that the AKARI FISBSC contains not only galaxies, but also many Galactic sources, such as AGBs, HII regions, planetary nebulae, etc. (e.g. Pollo et al. 2010). With this goal, we cross-identify the FISBSC with the IRAS PSCz catalog, which presents a redshift survey of galaxies selected at the IRAS 60 μm with a flux limit of $S_{60} > 0.6$ [Jy]. The search radius is set at $36''$, considering the position accuracy of these two catalogs. After cross-identification, 5890 matches are found. Adjusting the radius does not affect this result much: We change the searching radius from 20 to 60 arcsec, and find that the difference of the number of matches is less than 5%.

The AKARI and IRAS flux densities are compared in order to examine our sample selection. Figure 2.1 gives the comparison of IRAS 60 and 100 μm bands with AKARI 65, 90 and 140 μm bands. The upper left panel, which compares the flux densities at IRAS 60 μm band with AKARI 90 μm band, shows that the limits of both IRAS and AKARI are well-definded, and neither of them strongly restricts the sample. The effective limit of 90 μm densities can be estimated from the upper left panel, which is ~ 0.8 Jy.

In order to use optical data from Sloan Digital Sky Survery (SDSS), we confine the our data to the survey area of SDSS, which is 8378.015 deg^2. In this area, our sample contains 1186 galaxies. Then we include the GALEX UV data into the sample.

Cross-matching with GALEX UV data

The GALEX images are taken from GR4/GR5 database of all sky imaging survey (AIS). The process to carry out the photometry is shown in Figure 2.2. We summarize the major steps as follows (Iglesias-Páramo et al. 2006):

1. We cut out images from GALEX tiles including the target galaxy. The cutouts give images centered at the target galaxy with the size of $30' \times 30'$. Sometimes GALEX tiles cannot cover the target source in the images, so these images are discarded.

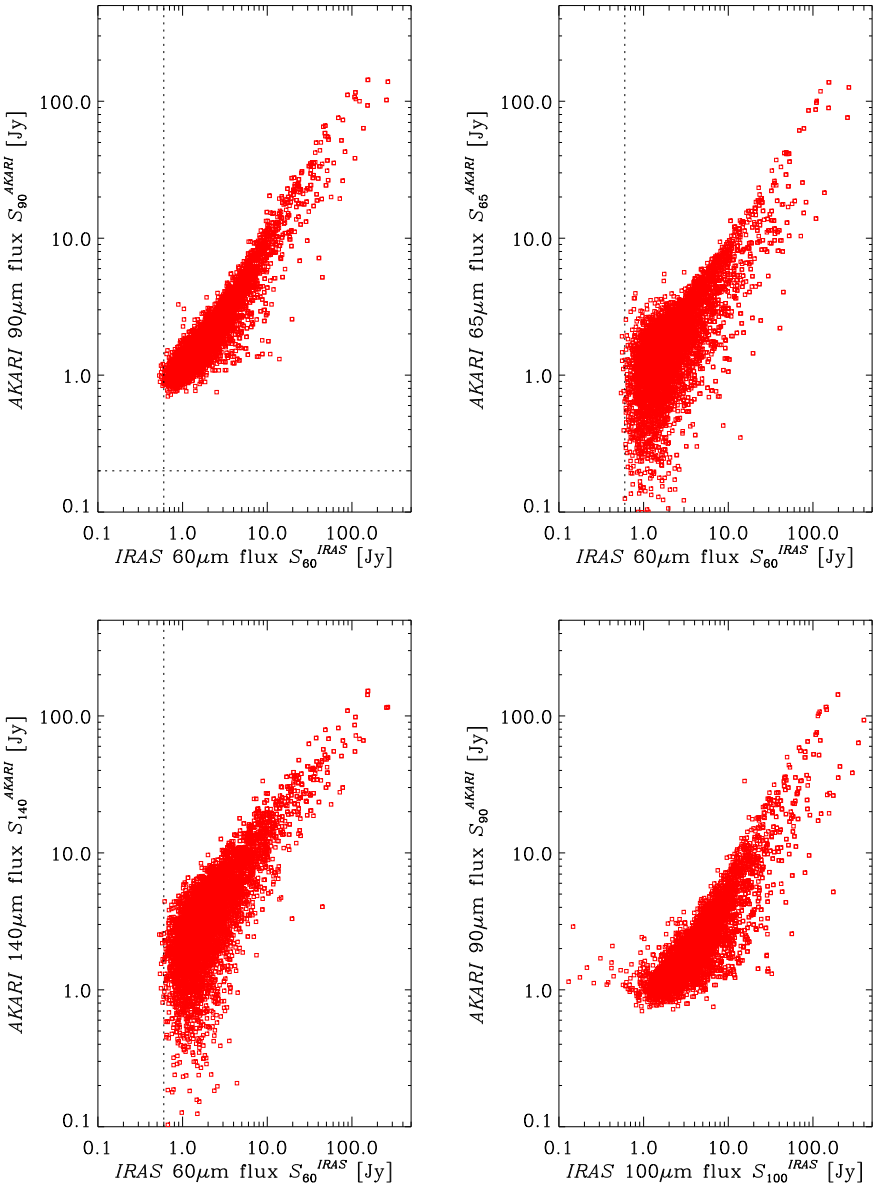

Figure 2.1 The comparison between AKARI FIS 65, 90 and 140 μm and IRAS PSCz 60 and 100 μm. The vertical dotted lines represent the flux density limit of IRAS PSCz. The horizontal line in the upper left panel represents the expected detection limit of AKARI 90 μm band.

2. Comparing the exposure time of cutouts for the same object, we keep the cutout with longest exposure time considering the quality of the image. These cutouts are used to carry out the photometry.

3. The NUV images are used as the reference for source detection. First the outline of the source is detected by eye to give an initial constraint for the area. We manually circle the initial values of the area of the source.

4. The program then searches the region outside the initial profile defined by our hand. The background is calculated at a far enough distance from the source.

5. Inside the area, our program automatically defines a set of elliptical apertures and calculates the flux inside each aperture. Then the growth curve from the inner to outer apertures is plotted and the flux at which the growth curve converges is taken as the result.

6. The Galactic extinction is corrected using the Schlegel map (Schlegel et al. 1998) and the Galactic extinction curve of Cardelli et al. (1989). The Schlegel map gives the extinction map of Galactic dust for V band. Then by using the extinction curve, which describe the variation of extinction at different wavelength, we can derive the Galactic extinction for each of our galaxies.

The GALEX pipeline may identify a well resolved source with patchy light distribution as several small sources ('*shredding*'). Our manual measurement allows to avoid this disadvantage by introducing initial constraints by hand. This program is also used by Buat et al. (2007), Takeuchi et al. (2010), as well as the studies of mergers which will be presented in Chapter 4, and has been proved to be able to generate stable and reliable photometry results.

After matching our previous dataset with the GALEX data, there are 776 galaxies left.

Cross-matching with SDSS and 2MASS

First, 2MASS all-sky extended Source Catalog (XSC) is used to cross match with our sample to provide photometry at NIR bands (*J, H,* K_s). The searching radius

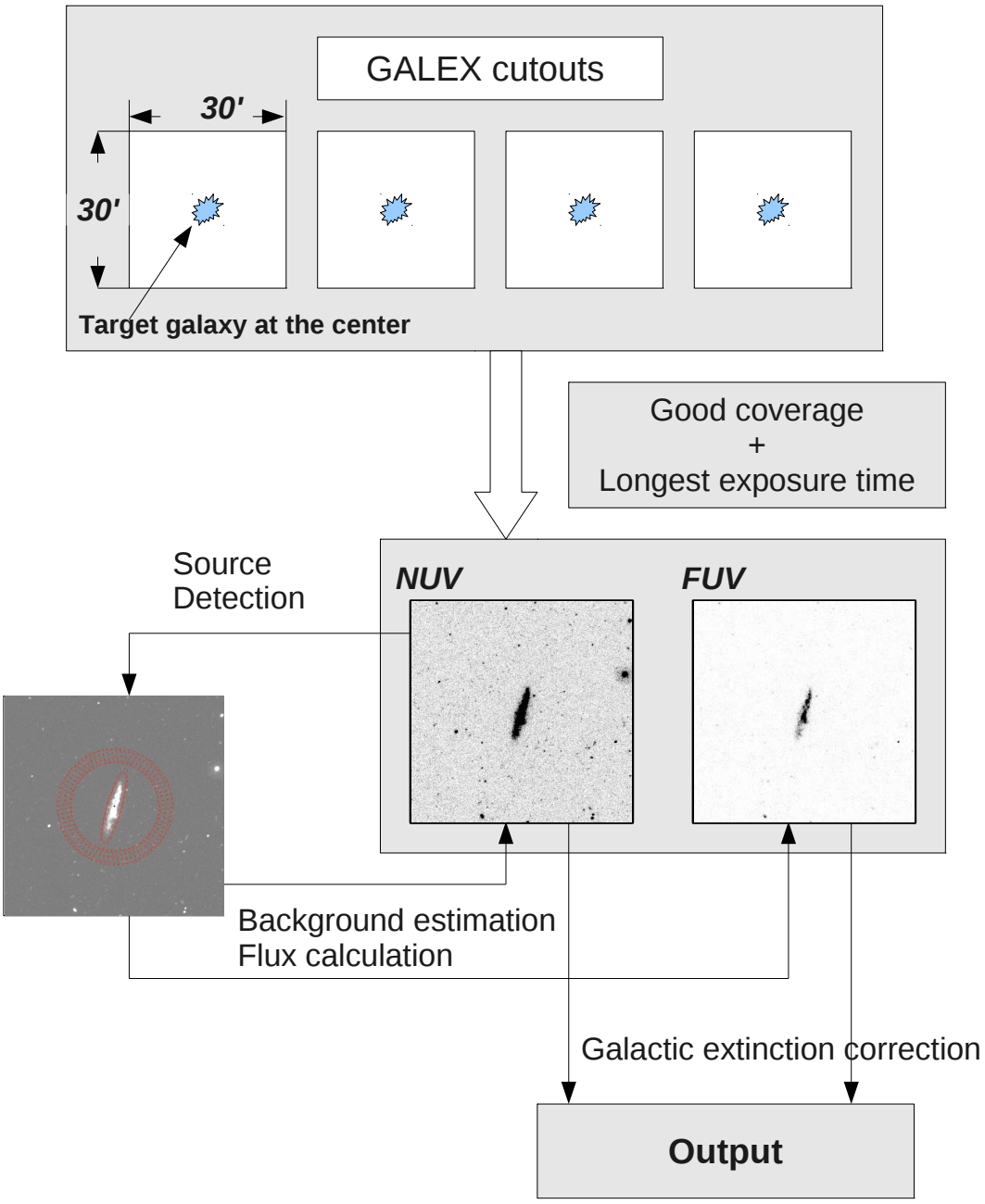

Figure 2.2 The scheme of the process of GALEX photometry.

is first taken as 20″. When there are multiple matches the brightest source is taken. Seven galaxies in our sample are found to have no counterpart in XSC. For these seven galaxies, we increase the searching radius to 30″. However, still no match was found. Therefore, the detection limits of 2MASS XSC are taken as the upper limit for the fluxes of these sources. The detection limits at *J, H* and K_s bands are 14.7, 13.9 and 13.1 mag, respectively (Jarrett et al. 2000).

Then, all the galaxies are matched with SDSS database using a searching radius of 15″. The closest sources are taken when multiple matches appear. The sources are inspected to check whether they are contaminated by nearby stars, artifacts, etc. Removing the star contamination requires careful masking of the SDSS images. For convenience, we just removed the sources with star contamination from our sample.

After all these procedures, we got a sample of 607 galaxies, with photometry information at UV, optical, NIR and FIR bands, which is the parent sample of the following study (Takeuchi et al. 2010).

2.2.2 Adding MIR information

The AKARI Infrared Camera All-Sky Survey has been done by two channels of the infrared camera (IRC): MIR-S channel and MIR-L channel. Photometric bands used in the survey are S9W (6.7 – 11.6 μm) and L18W (13.6 – 25.6 μm) with effective wavelength of 9 and 18 μm, respectively (Ishihara et al. 2010).

AKARI IRCPSC contains flux data at 9 μm and 18 μm with the detection limit 50 mJy and 90 mJy, respectively (Ishihara et al. 2010). After cross-identification with the parent sample, there are 162 galaxies with either 9 μm or 18 μm flux. However, nine galaxies are found to have inconsistent fluxes at GALEX, SDSS or 2MASS bands according to their SEDs, possibly due to the measurement error or the misidentification of objects caused by the inhomogeneous resolution of each observation, and thus these objects are discarded from our sample. We also discard one galaxy with too low redshift ($z \sim 0.0008$), which does not allow a successful SED fitting with our codes. The summary of the sample is listed in Table 2.1. Searching in SIMBAD database, we find most of galaxies in our sample are normal star forming galaxies:

Table 2.1 A brief summary of the sample. Data with an asterisk (*) are not used for SED fitting in Section 2.3.

Survey	Band	Wavelength (μm)	N
GALEX	FUV, NUV	0.153, 0.231	153
SDSS	*u*, *g*, *r*, *i*, *z*	0.355, 0.469, 0.617, 0.748, 0.893	153
2MASS	*J*, *H*, *Ks*	1.244, 1.655, 2.169	153
IRAS*	band-1, 2, 3, 4	12, 25, 60, 100	153
AKARI IRC	*S9W*	9	126
AKARI IRC	*L18W*	18	106
AKARI FIS	*N60*, *Wide-S*, *Wide-L*, *N160**	65, 90, 140, 160	153

only 15 galaxies are classified as AGNs (including Seyfert 1 and Seyfert 2 galaxies). All the galaxies in our sample are nearby galaxies. The distribution of their redshifts is shown in Figure 2.3.

2.2.3 The Re-estimation of the AKARI FIR Flux

The FISBSC flux density for extended sources is not accurate because of the point source extraction procedure. In our sample, a considerable fraction of galaxies are the extended sources. Therefore, it is questionable whether the catalog data of these sources are reliable. This is confirmed by making a comparison between FISBSC fluxes and IRAS co-added fluxes (Figure 2.4), which were specially calculated for extended sources (Saunders et al. 2000). In order to investigate the dependence of FISBSC flux on the angular size of the galaxy, the sample was divided into three sub-samples according to the size of the galaxy (Table 2.2).

The lines in Figure 2.4 show predictions of the difference between two different bands by Dale & Helou (2002) (hereafter DH) one-parameter constrained SED templates. The parameter α is related to IRAS flux ratio f_{60}/f_{100}[1]. The values of $\log(f_{60}/f_{100})$ for our galaxies range from -0.60 to 0.25, and most of the galaxies have $\log(f_{60}/f_{100})$ between -0.5 and 0.0, corresponding to an α value between

[1]We define $f_\lambda = \nu f_\nu$ at λ μm.

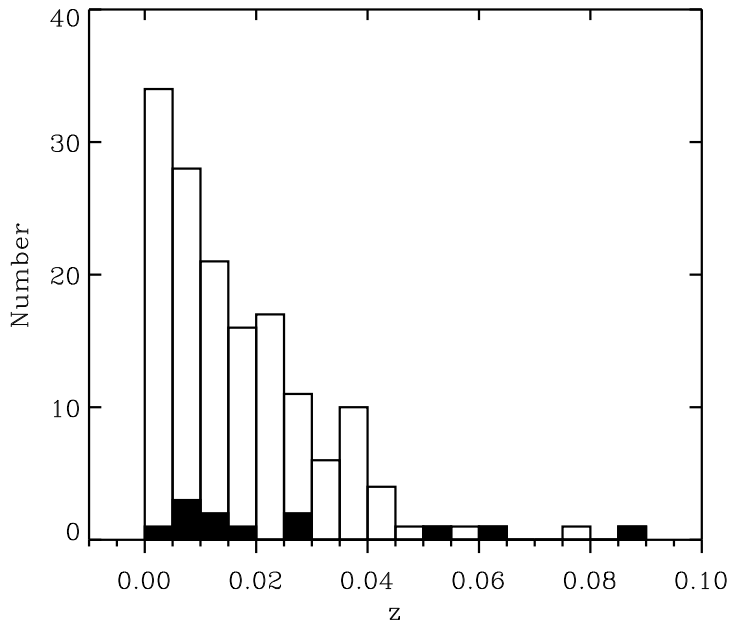

Figure 2.3 The redshift distribution of our sample. The filled area corresponds to AGNs.

Table 2.2 Criteria to divide the sample into three sub-samples. The length of major axis a and minor axis b of each galaxy is obtained from the SDSS image. The $40''$ is taken as the separating value considering the PSF size of AKARI/FIS.

Sub-sample	Criteria
Small	$a < 40''$ and $b < 40''$
Medium	$a > 40''$ or $b > 40''$
Large	$a > 40''$ and $b > 40''$

2.625 and 1.375. Accordingly, the model predictions with $\alpha = 1.375$, 2.625 and its median value 2.0 are presented in Figure 2.4. Table 2.3 presents the median values of $\log(f_{\rm AKARI}/f_{\rm IRAS})$ for each sub-sample. Compared with the model predicted values, there are clear discrepancies between FISBSC and IRAS data, especially for $60-65$ μm and $90-100$ μm. Also note that the large galaxies show larger discrepancies than small ones, indicating that the PSF photometry is less reliable for larger galaxies, because a considerable part of their flux is left out by the relatively small beam size.

Aiming to obtain more reliable flux data, the photometry of the diffuse maps provided by the AKARI group was conducted using Source Extractor. Source Extractor (SExtractor) is a photometry program that can be used for reduction of large scale galaxy-survey data. It is efficient and can automatically detected the edge of the source, and hence not affected by the extension of the galaxy. We use the "AUTO" flux given by the outputs of SExtractor. This flux is intended to be the most precise measure of the total flux.

Figure 2.5 gives diffuse maps for one galaxy at the *N60* (65 μm), *Wide-S* (90 μm), *Wide-L* (140 μm) and *N160* (160 μm) bands as an example. The obtained "AUTO" fluxes were also compared with IRAS co-added fluxes.

In the 90 μm band, the result shows a great improvement of the consistency with the IRAS flux according to the DH model (Figure 2.6 and Table 2.3) for all galaxies in our sample. At 65 and 140 μm bands, the consistency is improved for those galaxies in 'Medium' and 'Large' subsamples, whereas the dispersion increases for the galaxies

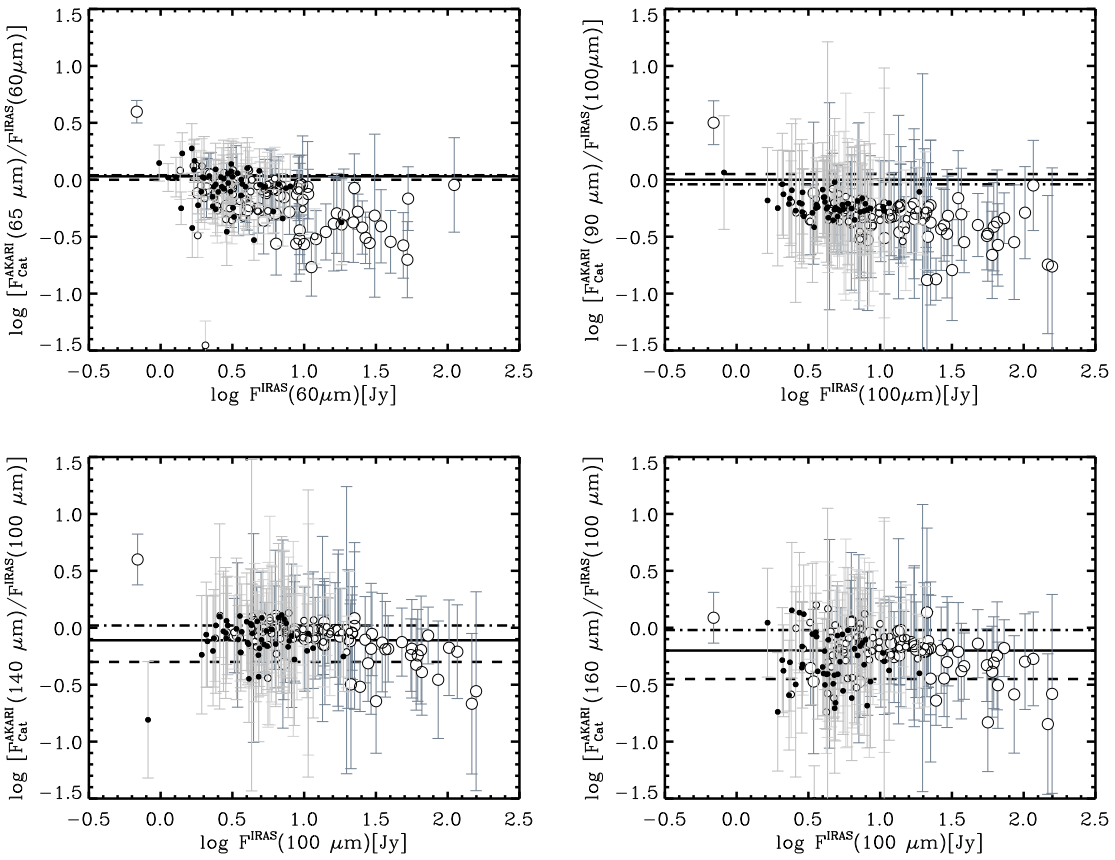

Figure 2.4 Comparison between the FIS catalog flux and the IRAS flux. Galaxies in different sub-samples are shown as symbols of different sizes (large open circles: large; small open circles: medium; dots: small). The DH models with three different α are shown as different lines (dashed: $\alpha = 1.375$; solid: $\alpha = 2.0$; dash-dotted: $\alpha = 2.625$).

Table 2.3 Comparison between AKARI and IRAS fluxes. The mean values of the difference between AKARI and IRAS fluxes according to AKARI FISBSC fluxes (Catalog), fluxes derived from diffuse maps (Map) and DH model prediction (Model) are listed for each subsample of galaxies ('L', 'M' and 'S' represent large, medium and small group in Table 2.2, respectively).

		$\log(f_{65}/f_{60})$	$\log(f_{90}/f_{100})$	$\log(f_{140}/f_{100})$	$\log(f_{160}/f_{100})$
Catalog	L	-0.18	-0.33	-0.09	-0.20
	M	-0.09	-0.27	-0.04	-0.17
	S	-0.03	-0.24	-0.09	-0.32
Map	L	-0.10	-0.13	0.03	0.01
	M	-0.12	-0.12	0.01	0.00
	S	-0.01	-0.11	-0.02	0.07
Model	$\alpha = 1.375$	0.00	0.05	-0.30	-0.45
	$\alpha = 2$	0.03	0.00	-0.11	-0.20
	$\alpha = 2.625$	0.04	-0.04	0.02	-0.02

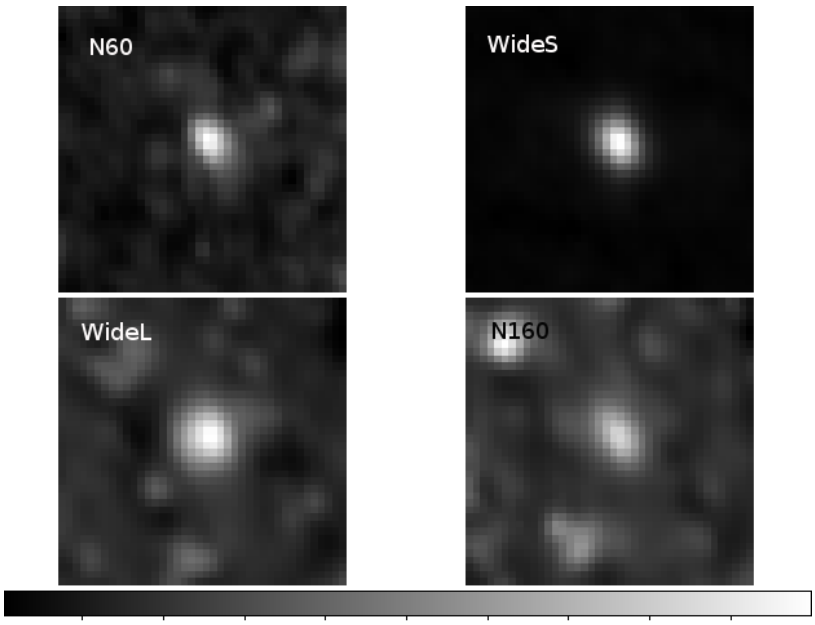

Figure 2.5 Diffuse maps for one galaxy in our sample at the *N60*, *WideS*, *Wide-L* and *N160* bands.

in the 'Small' subsamples. Less improvement is found at 140 μm band, which can be explained by a relatively large PSF FWHM at this band ($\sim 60''$, as compared with $\sim 39''$ for the 65 and 90 μm bands, see Kawada et al. 2007). At the 160 μm band, neither fluxes derived from the diffuse maps nor those from the IRCPSC are satisfying, which is due to the poor quality of this band; for this reason 160 μm data were not used in the following discussion. Therefore, we kept IRCPSC flux values for 'Small' sources at the 60 and 140 μm bands, and applied fluxes derived from diffuse maps to the other sources. In addition, fluxes derived from AKARI diffuse maps showed notably smaller measurement errors than the IRAS fluxes, greatly improving the data quality. Considering that the IRAS fluxes provide information similar to that given by the AKARI bands, we omitted IRAS fluxes when fitting the SEDs.

Note that the MIR data provided by IRCPSC were little affected by an extension of the source, since it applies "AUTO" fluxes by SExtractor, which are suitable for both point sources and extended sources.

2.3 SED fitting and SFR Calculation

2.3.1 CIGALE SED fitting code

The SED fitting program CIGALE (Noll et al. 2009) was used to calculate the SFR for our sample. CIGALE was developed to derive highly reliable galaxy properties by fitting the UV/optical SEDs and the related dust emission at the same time, i.e., the stellar population synthesized models are connected with infrared templates by the balance of the energy of dust emission and absorption. A detailed description of CIGALE can be found in Noll et al. (2009); Buat et al. (2011); Giovannoli et al. (2011). Here we give a brief introduction to its main features.

CIGALE allows one to use the stellar SEDs from models given either by Maraston (2005) or by Fioc & Rocca-Volmerange (1997, PEGASE). The difference between these models is the contribution of the thermally pulsating asymptotic giant branch (TP-AGB) stars. In PEGASE models, the contribution from TP-AGB stars is low (Maraston et al. 2006). Maraston (2005) increased the contribution from TP-AGB

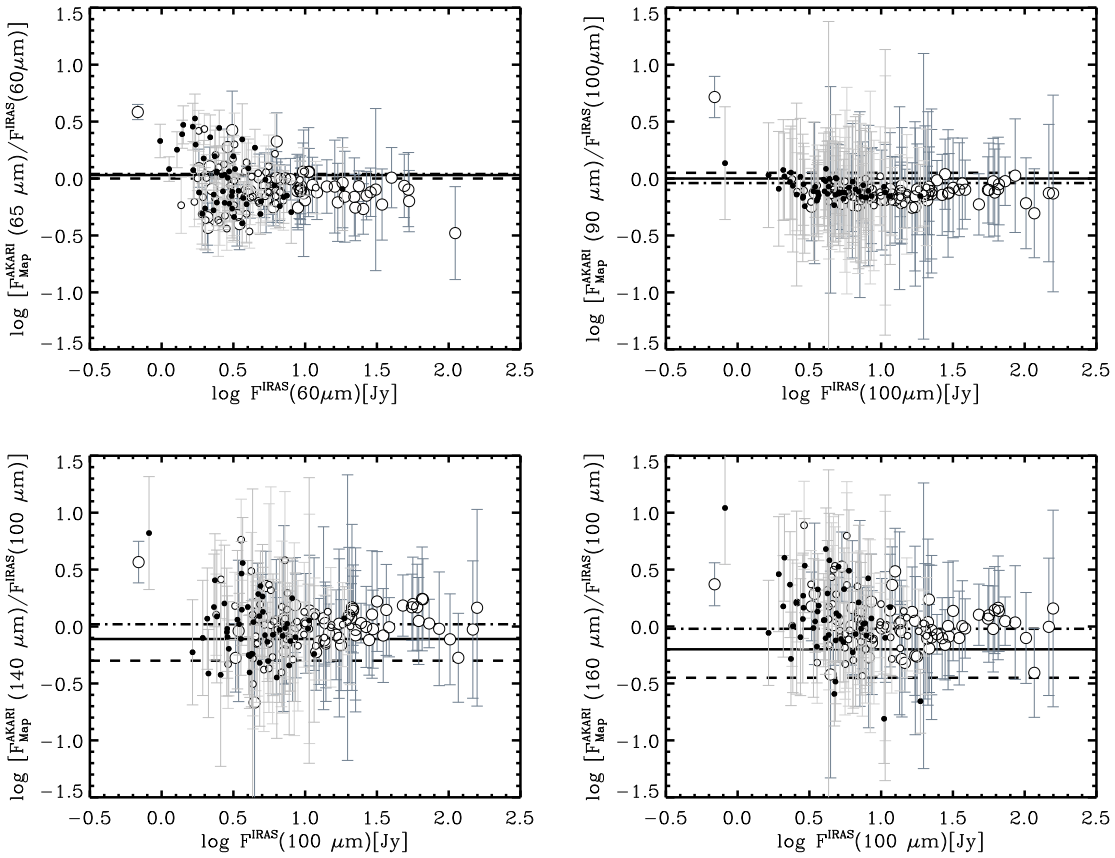

Figure 2.6 Comparison between FIS diffuse map fluxes and the IRAS fluxes. The meaning of the symbols is the same as in Figure 2.4

Figure 2.7 Illustrations of Kroupa IMF and Salpeter IMF.

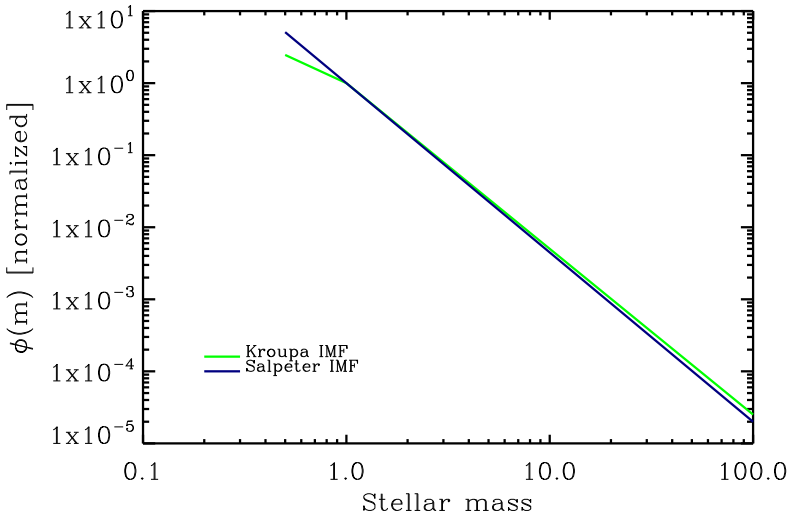

stars adopting the 'fuel consumption' approach. Maraston et al. (2006) have shown that the insufficient consideration of TP-AGB stars overestimates the stellar mass by 0.2 dex and worsens the consistency with IR observation data at a redshift of $z \sim 2$. At lower redshifts, it is found that using different models hardly affects the results (Rettura et al. 2006; Eminian et al. 2008). Therefore, the models from Maraston (2005) were preferred in this work. The Kroupa IMF (Kroupa 2001) was used to calculate the complex stellar populations (CSPs). Figure 2.7 shows the normalized Kroupa IMF and Salpeter IMF.

CIGALE provides two scenarios of star formation: one is "box models" with a constant SFR, the other is "τ models", for which SFR decreases exponentially with a typical decay time, τ. SFR is calculated as

$$\mathrm{SFR}_{\mathrm{box}} = M_{\mathrm{gal}}/t \tag{2.1}$$

for "box models", and

$$\mathrm{SFR}_{\tau} = M_{\mathrm{gal}}/[\tau(e^{t/\tau} - 1)] \tag{2.2}$$

for "τ models", where M_{gal} is the galaxy mass (Noll et al. 2009). CIGALE also allows one to apply different scenarios for young and old populations. The input

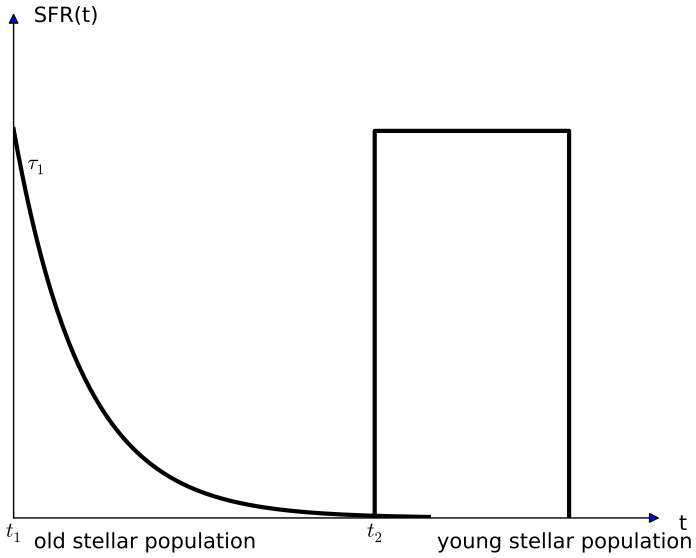

Figure 2.8 Illustration of the scenario of star formation history (SFH) adopted in our work. The old stellar population is assumed to have an exponentially decreasing trend. The decreasing rate can be changed by modifying the e-folding time τ_1. The young stellar population represents a recent burst of star formation. This population is created in t_2 years at a constant and adjustable rate.

SFH here is a constant burst SFH for young stellar populations, and an exponentially decreasing one for old stellar populations. Thus SFRs were calculated using the formula $f_{\rm ySP} \cdot {\rm SFR}_{box} + f_{\rm oSP} \cdot {\rm SFR}_{\tau}$, where $f_{\rm ySP}$ and $f_{\rm oSP}$ are fractions of young stellar populations and old stellar populations, respectively.

The attenuation curve adopted by CIGALE is based on a law given by Calzetti et al. (2000), with modification of the slope and/or adding a UV bump. The modification of the slope is controlled by the factor $(\lambda/\lambda_V)^{\delta}$, i.e., by changing δ, the slope of the attenuation curve can be modified. We only considered a modification of the slope of the attenuation law here, and no bump was introduced. CIGALE allows one to consider different effects of attenuation for old and young stellar populations by adding the reduction factor f_{att} of the dust attenuation for the old stellar populations as an input parameter. For the IR part, CIGALE uses DH models, which are

Figure 2.9 DH models for dust emission. The figure is taken from `http://physics.uwyo.edu/~ddale/research/seds/seds.html`.

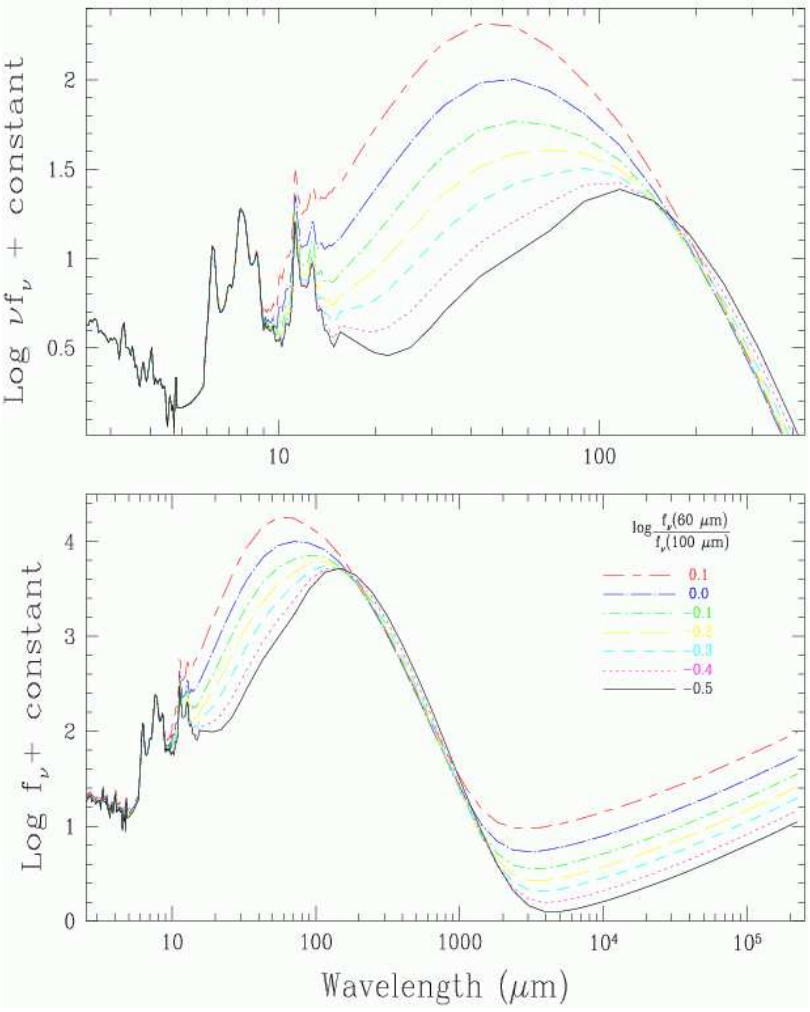

described in Section 2.2. The sample templates of DH models are shown in Figure 2.9 Then the dust emission was calculated, and by balancing the energy emitted and absorbed, the short and long wavelength parts of the model were connected.

Output parameters can be computed by two methods provided by the code: "sum" and "max". The former calculates the probability density functions (PDFs) by taking the sums of the probability ($\propto\ e^{-\chi^2/2}$) of the models in given bins of parameter space.

The χ^2 of model i is given by:

$$\chi_i^2 = \sum_X \left[\frac{F_{obs,X} - a_i F_{mod_i,X}}{\sigma(F_{obs,X})} \right], \tag{2.3}$$

where $F_{obs,X}$ is the observed flux at different wavelengths X, and $\sigma(F_{obs,X})$ is its error (see also Section 1.6.2).

The "sum" approach might cause an unintentional bias when the input parameter values are badly chosen. The "max" introduces a fixed number of equally sized bins for each parameter and searches the maximum probability $P_i(x)$ of models in bin i by

$$P_i(x) = max(p_j a_{ji}), \tag{2.4}$$

where p_j is the probability of each model. The value $a_{ji} = 1$ if the model j belongs to the bin i, otherwise $a_{ji} = 0$. Then these maximum probabilities are taken as weights for individual bins to calculate the expectation value of the parameter. The advantage of this method is that it alleviates the dependence on the choice of parameters (see Noll et al. 2009, for detail). Therefore, we applied the "max" method in this work.

The expectation value of each parameter $\langle\ x\ \rangle$ is given by:

$$\langle\ x\ \rangle\ =\ \frac{\Sigma_{i=1}^{b} P_i x_i}{\Sigma_{i=1}^{b} P_i}, \tag{2.5}$$

and the standard deviation σ is obtained by:

$$\sigma_x\ =\ \sqrt{\frac{\Sigma_{i=1}^{b} P_i (x_i\ -\ \langle\ x\ \rangle)^2}{\Sigma_{i=1}^{b} P_i}}, \tag{2.6}$$

where b is the number of bins in the parameter space.

The input parameters applied in this study were adopted from Buat et al. (2011) in order to obtain a stable and reliable output (Table 2.4). Since CIGALE is unable to trace the unobscured emission of an AGN, for Seyfert 1 galaxies, the output decreases the reliability (Buat et al. 2011). For dust-obscured AGNs, CIGALE provides models to fit the SED, and can avoid introducing any severe bias. Therefore, five Seyfert 1 galaxies were rejected from our sample, and remaining AGNs are marked during analysis. In order to keep the accuracy of derived SFRs, galaxies with relatively large discrepancies between observed and output spectra (reduced $\chi^2\ >\ 10$) were

Table 2.4. List of input parameters for CIGALE (Buat et al. 2011).

parameter	Symbol	input values
metallicities (solar metallicity)	Z	0.02
τ of old stellar population models [Gyr]	τ_1	1; 3.0; 5.0; 10.0
ages of old stellar population models [Gyr]	t_1	13
ages of young stellar population models [Gyr]	t_2	0.025; 0.05; 0.1; 0.3; 0.5; 1.0
fraction of young stellar population	f_{ySP}	0.001; 0.01; 0.1; 0.999
Slope correction of the Calzetti law	δ	-0.3; -0.2; -0.1; 0.0; 0.1; 0.2
V-band attenuation for the young stellar population	$A_{V,ySP}$	0.15; 0.30; 0.45; 0.60; 0.75; 0.90; 1.05; 1.20; 1.35; 1.5; 1.65; 1.8; 1.95; 2.1
Reduction of A_V basic for old SP model	f_{att}	0.0; 0.5; 1.0
IR power-law slope	α	1.0; 1.5; 1.75; 2.0; 2.25; 2.5; 4.0

discarded as being unreliable. At the first run, we had 25 such galaxies. By updating the SDSS data using Navigator of SDSS DR7/8 instead of the original pipeline data from SDSS DR7, the reduced χ^2 values of 17 galaxies decreased to less than 10. [2] Four of the eight remaining galaxies had very poor quality of AKARI diffuse maps. The other four are very extended and brightness, which could cause incomplete flux derivation or saturation in the optical plates. Considering that the number was small ($\sim$ 6%), these eight galaxies and five out of the other 17 galaxies were discarded. Therefore, reliable SFRs were derived for 140 galaxies, out of which there are 112 with available 9 μm fluxes and 97 with 18 μm fluxes.

2.3.2 The reliability of the results

For SED fitting, the accuracy of the output depends on the input parameters. To give proper estimates of the SFRs, the robustness of the results must be tested.

[2]There is no modification for other sources which are fitted well.

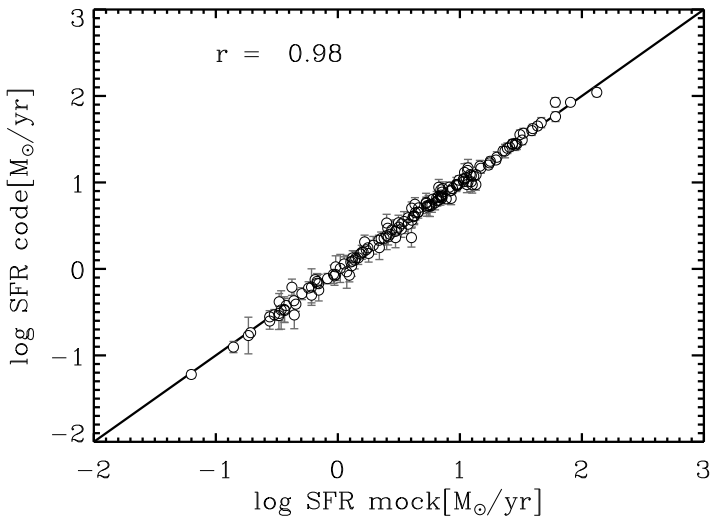

Figure 2.10 The comparison between SFRs derived by CIGALE and from the mock galaxies.

A straightforward way to check the reliability of the output of CIGALE is to use a sample of mock galaxies with comprehensively known physical parameters. Mock galaxies can be generated following a recipe in Giovannoli et al. (2011): 1. Run CIGALE on the data of real galaxies. For each galaxy, the best model is selected by a χ^2 minimization. Then, from these models, the flux at each band can be estimated. 2. Add to each flux a random relative error, which is normally distributed with $\sigma = 0.1$. Thus, we obtain a mock catalog with flux information at each photometric band used in this study. 3. The last step is to run the code on the mock catalog and then to compare the output parameters with the exact values provided by the best models. The result of the comparison in the case of our data is shown in Figure 2.10. We only present the results concerning SFRs because in this work the SFR is the only parameter about which we are concerned. Figure 2.10 shows that the two quantities are well related, indicating that the SFR derived here is reliable.

As discussed in Noll et al. (2009), CIGALE could provide stable results of SFRs as long as one constraint beyond PAH band is given. We ran CIGALE with and

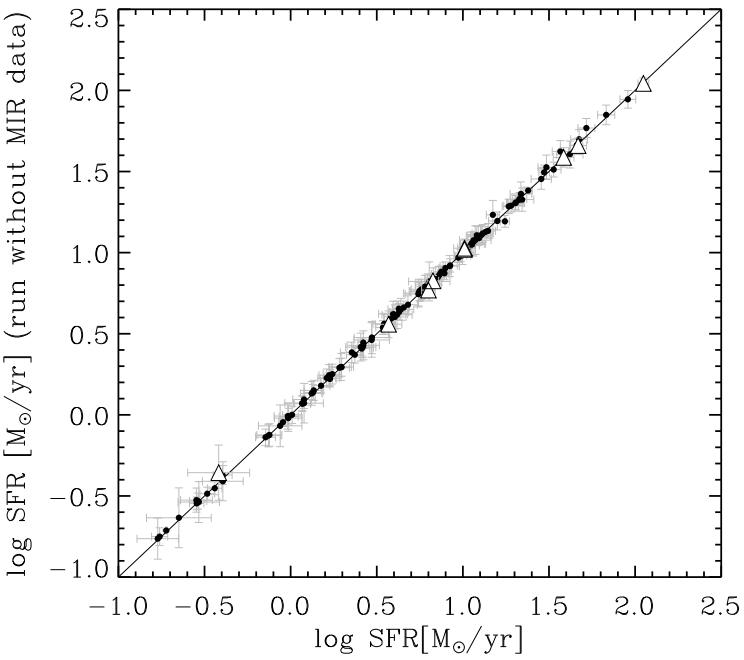

Figure 2.11 The comparison between SFR derived with and without MIR data. AGNs are shown as triangles.

without MIR data to examine the influence of including MIR photometric data on the output SFR. The result shows that adding the MIR data or not has almost no influence on the resulting value of SFR (Figure 2.11), while not using FISBSC data introduces large uncertainties to the output, consistent with the conclusion of Noll et al. (2009) who was using SINGS sample.

2.4 Results and Discussion

Apparently, the luminosity at 9 μm and 18 μm, namely L_9 and L_{18}[3], both correlate with SFRs (Figure 2.12 and Figure 2.13); the Spearman's correlation coefficients are 0.943 for the L_9-SFR relation and 0.956 for the L_{18}-SFR relation[4]. The linear

[3] L_λ refers to νL_ν at wavelength λ.

[4] Pearson's correlation coefficient is 0.944 for L_9-SFR relation and 0.951 for L_{18}-SFR relation

regressions following the method provided by Kelly (2007) give:

$$\log \frac{\mathrm{SFR}}{M_\odot/\mathrm{yr}} = (0.99 \pm 0.03) \log \frac{L_9}{L_\odot} - (9.02 \pm 0.32) \quad (2.7)$$

and

$$\log \frac{\mathrm{SFR}}{M_\odot/\mathrm{yr}} = (0.90 \pm 0.03) \log \frac{L_{18}}{L_\odot} - (8.03 \pm 0.30). \quad (2.8)$$

The scatter of the data points around the regression lines of Equations 2.7 and 2.8 is approximately the same, with $\sigma = 0.18$ dex for 9 μm and 0.20 dex for 18 μm. These tight correlations also hold for the surface densities of luminosities and SFRs (Figures 2.14 and 2.15). The correlation coefficients are 0.961 for 9 μm and 0.945 for 18 μm. The areas of galaxies were calculated from g-band images of SDSS. The regression gives:

$$\begin{aligned} \log \frac{\Sigma_{\mathrm{SFR}}}{M_\odot \mathrm{yr}^{-1} \mathrm{kpc}^{-2}} &= (1.02 \pm 0.03) \log \frac{\Sigma_9}{L_\odot \mathrm{kpc}^{-2}} \\ &- (9.30 \pm 0.19) \end{aligned} \quad (2.9)$$

with $\sigma = 0.18$, and

$$\log \frac{\Sigma_{\mathrm{SFR}}}{M_\odot \mathrm{yr}^{-1} \mathrm{kpc}^{-2}} = (0.98 \pm 0.04) \log \frac{\Sigma_{18}}{L_\odot \mathrm{kpc}^{-2}} \quad (2.10)$$

$$- (8.89 \pm 0.25). \quad (2.11)$$

with $\sigma = 0.22$.

Figures 2.12 and 2.13 show that AGNs share a MIR-SFR relation similar to normal star-forming galaxies, although the radiation mechanism of AGNs is different from normal galaxies. The slopes of the $\log L_9$-logSFR and $\log L_{18}$-logSFR relations derived here are almost equal to one, indicating the MIR-SFR relations are close to linear.

2.4.1 Comparison with SFR calibrations from Spitzer data

Spitzer 8 μm and 24 μm data were investigated as SFR tracers by several authors (e.g Wu et al. 2005; Pérez-González et al. 2006; Calzetti et al. 2007; Relaño et al. 2007; Zhu et al. 2008; Rieke et al. 2009). The 24 μm fluxes were found to be tightly related to the emission of the warm dust, and thus more intensively investigated, whereas

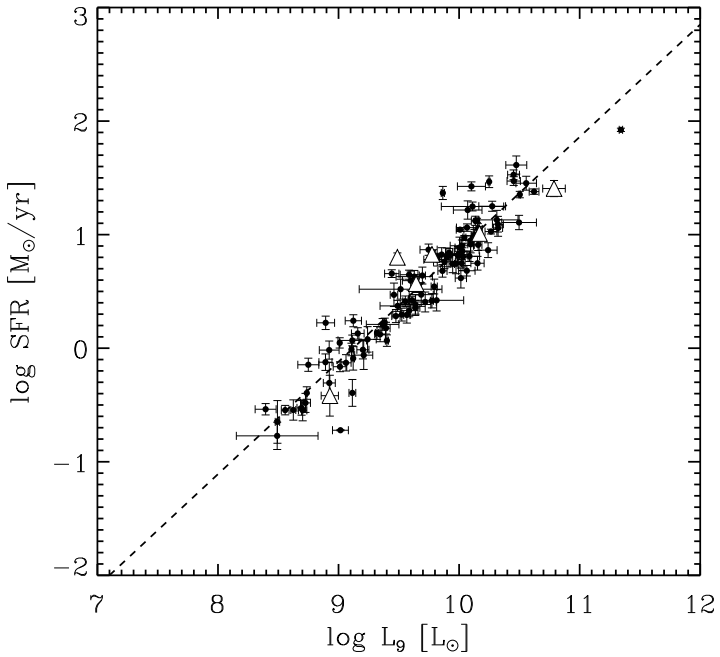

Figure 2.12 The 9 μm luminosity-SFR relation. The dashed line shows the fitting result. The triangles are AGNs.

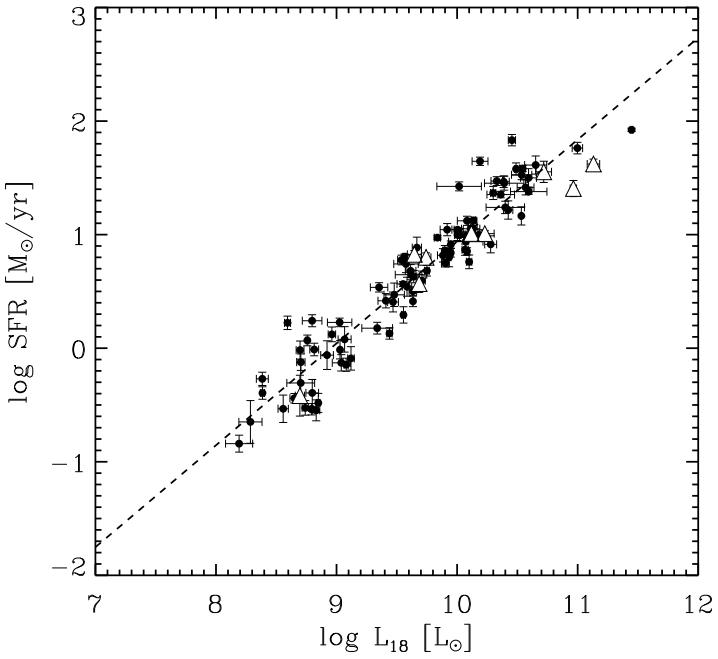

Figure 2.13 The 18 μm luminosity-SFR relation. Lines and symbols are the same as in Figure 2.12.

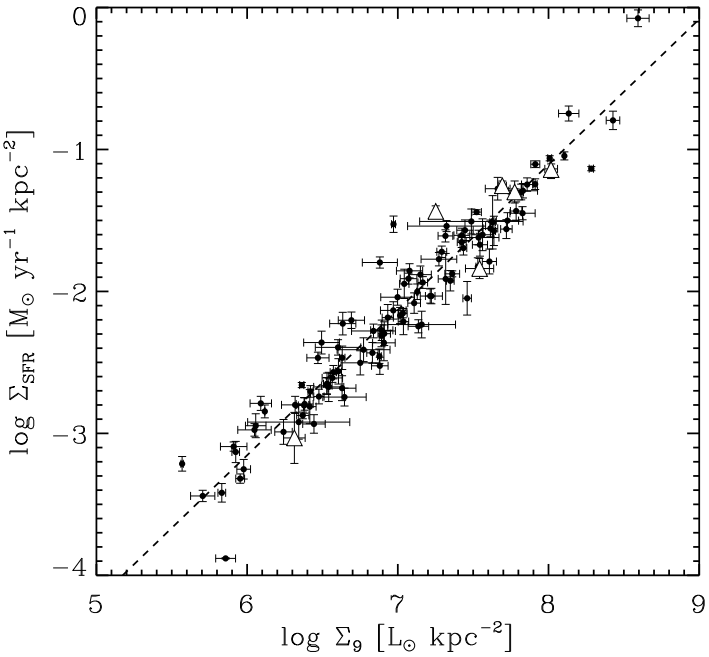

Figure 2.14 The surface densities of 9 μm luminosity-SFR relation. The dashed line shows the best fit. The triangles are AGNs.

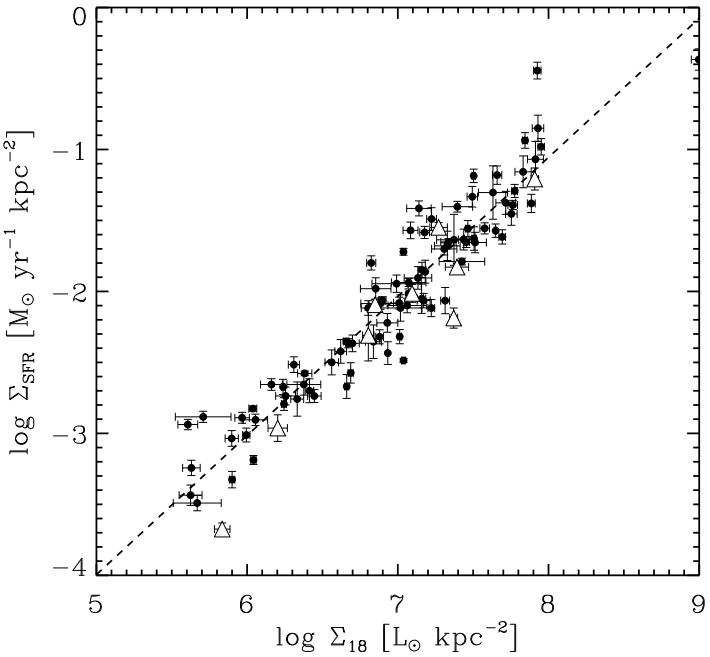

Figure 2.15 The surface densities of 18 μm luminosity-SFR relation. Lines and symbols are the same as in Figure 2.12.

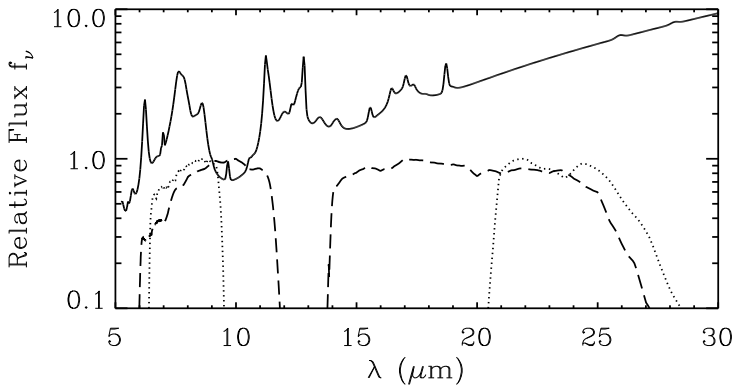

Figure 2.16 The filter response curves of AKARI 9 μm and 18 μm bands (dashed line) and Spitzer 8 μm and 24 μm bands (dotted line). The solid line is the luminosity weighted average spectrum of star forming galaxies from Smith et al. (2007b).

the 8 μm-SFR relation is more complicated, strongly depending on parameters such as the metallicity, size and star-formation history (Calzetti et al. 2007). Therefore, there are fewer calibrations.

The main difference between the AKARI and Spitzer filters is their bandwidth. Due to the wider band, AKARI 9 μm and 18 μm fluxes are more affected by silicate absorption, PAH and molecular hydrogen line emissions (Figure 2.16). In order to check the reliability of our calibrations, the SFRs derived from Equations 2.7 and 2.8 were compared with those given by Spitzer calibrations. The work to compare was chosen to keep the luminosity range close to the present sample (Table 2.5). The calibrations given by Wu et al. (2005) and Zhu et al. (2008) are based on the equation given by Kennicutt (1998a) in which Salpeter IMF was used. The use of Salpeter IMF will cause the SFR lower by $\sim$ 0.18 dex than some other IMF with a more shallow slope at low masses (Rieke et al. 2009). Therefore this effect was corrected for the results of Wu et al. (2005) and Zhu et al. (2008).

Comparison between SFRs derived from 9 μm **and from** 8 μm

Spitzer 8 μm fluxes were computed from the output spectra of the CIGALE and filter response curves of Spitzer IRAC and MIPS. Since the 8 μm fluxes used in the calibration given in Table 2.5 correspond to the dust emission with the stellar contribution subtracted following the recipe of Helou et al. (2004), the 3.6 μm flux was also calculated in order to compute the stellar composition contained at 8 μm, and thus 8 μm dust emission could be obtained (hereafter, we refer to 8 μm dust emission as 8 μm emission for conciseness). Note that here the stellar contribution is very small, which can only affect the result by $\sim$ 0.02 dex. The obtained flux is then converted to SFR by formulae given by previous work (Table 2.5). The results are plotted in Figure 2.17 (The typical 1σ uncertainty for the galaxy of a median luminosity is $\sim$ 0.5 dex). The statistical information about the comparison is summarized in Table 5.

The discrepancy between our results and Wu et al. (2005) may be due to several reasons. Wu et al. (2005) listed factors such as the accuracy of fiber aperture corrections, the validity of the estimation of the obscuration in galaxies by using Balmer decrement, the possible contamination to radio and MIR emission from obscured weak AGNs. The larger capacity of our sample (79 for 8 μm in Wu et al. (2005) compared with 112 in our sample) and the wider coverage of 9 μm band may also cause such difference. Another possible reason is that the oversimplification of PAH emission in DH models underestimates the 8 μm flux and therefore results lower SFRs. However, this level of discrepancy is well within the scatter given by Equation 2.7.

The discrepancy between Wu et al. (2005) and Zhu et al. (2008) results is attributed to the fact that Zhu et al. (2008) included 8 μm-weak HII galaxies with low MIR luminosity (Zhu et al. 2008). Since no such galaxies were included in present sample, it is reasonable that the present result agrees with Wu et al. (2005) better.

Comparison between SFRs derived from 18 μm **and** 24 μm

For a 18 μm–24 μm SFRs comparison, more reference calibrations are available (Table 2.5). The 24 μm fluxes are also derived from the output spectra of the SED

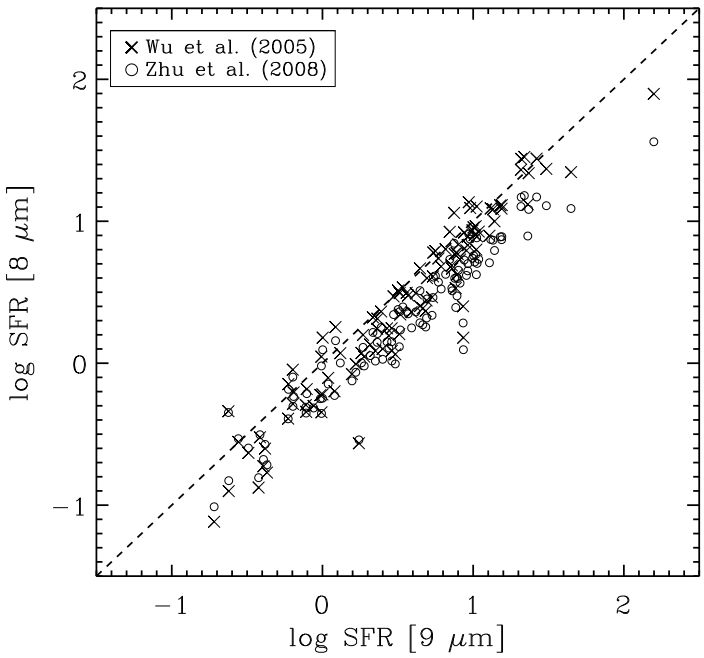

Figure 2.17 Comparison between the SFRs derived from 9 μm emission (Equation 2.7) and from 8 μm emission by Wu et al. (2005) (crosses) and Zhu et al. (2008) (circles).

fitting by CIGALE. The statistical information about the comparison is given in Table 2.7. The converted SFRs are plotted in Figure 2.18. Since the SFRs derived from Wu et al. (2005) are quite close to those from Zhu et al. (2008) and the luminosity range in Wu et al. (2005) is closer to this work, the results from Zhu et al. (2008) are omitted for the sake of brevity.

The results of Wu et al. (2005) and Zhu et al. (2008) agree well with our result after the correction of IMF. Rieke et al. (2009) assembled SED templates for local luminous and ultraluminous infrared galaxies and combined the result of Dale et al. (2007) and Smith et al. (2007b) to produce templates at lower luminosities. Their result is applicable to galaxies with 24 μm luminosity higher than $6 \times 10^8\ L_\odot$, corresponding to $\log\ \mathrm{SFR} = -0.33$, which is shown by the dotted line in Figure 2.18. The present result agrees very well with Rieke et al. (2009) above the limit.

Our result is a little higher than the one given by Calzetti et al. (2007). A possible reason is that the result of Calzetti et al. (2007) was derived for HII clouds by Paα emission, which might be poorly applied to galaxy-wide calculations, because the diffuse MIR or Paα emissions in the whole galaxy are not included (Alonso-Herrero et al. 2006; Calzetti et al. 2007; Kennicutt et al. 2007; Rieke et al. 2009).

2.4.2 Combination of FUV and MIR indicators

At lower IR luminosity, the IR indicator may fail to trace part of the UV photons from young stars due to the increased transparency of the ISM. A combination of unobscured FUV and MIR luminosities, (FUV + αMIR), may efficiently compensate for the lost energy, and could trace the SFR linearly (Zhu et al. 2008). However, upon converting SFRs to dust obscuration-corrected FUV fluxes by eq. [1] from Kennicutt (1998a), we find that $\alpha = 2.53$ with a scatter of 0.17 dex for 9 μm, and $\alpha = 3.33$ with a scatter of 0.20 dex for 18 μm. The scatter is not reduced significantly. This fact indicates that the origin of the scatter in MIR-SFR diagram is complicated: it results not only from the untraced UV photons, but also other unknown factors, such as the variation of the physical conditions within each galaxy, the distribution of dust and photo dissociation regions (PDRs), etc.

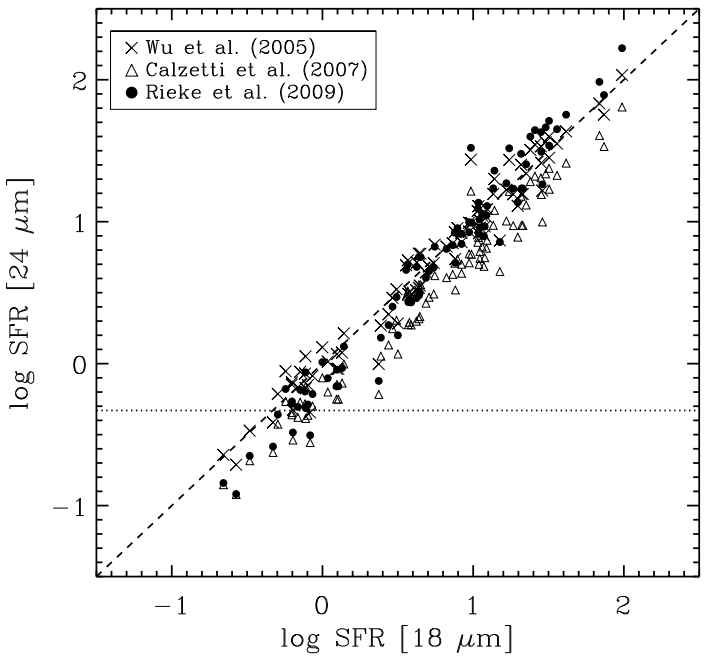

Figure 2.18 Comparison between the SFRs derived from 18 μm (Equation 2.8) and from 24 μm emission by Wu et al. (2005) (crosses), Calzetti et al. (2007) (triangles) and Rieke et al. (2009) (dots). The dotted line indicates the lower limit where the calibration of Rieke et al. (2009) applies.

2.4.3 Metallicity

We made an attempt to investigate the gas-phase metallicity range of our sample by searching in the metallicity database measured by Tremonti et al. (2004) for SDSS galaxies. Unfortunately, the 12 + log (O/H) values are given for only 33 galaxies (the metallicity of all these galaxies is higher than 8.75). Therefore, we applied a compromised method: we investigate the stellar mass M_* of our sample. Measured by CIGALE, the stellar mass M_* of all the galaxies in the sample is larger than $10^{8.5}$ $M_\odot$. Thus, from mass-metallicity relation given by Tremonti et al. (2004):

$$\begin{aligned} 12 + \log(\mathrm{O/H}) = & - 1.492 + 1.847(\log M_*) \\ & - 0.08026(\log M_*)^2, \end{aligned} \tag{2.12}$$

the metallicity 12 + log (O/H) for all galaxies in our sample is higher than 8.4. This is not surprising because the initial sample from Takeuchi et al. (2010) is IR selected, which means a considerably high luminosity in IR and thus sufficient dust content and relatively high metallicity range. Thus, the MIR-SFR relations derived here could only be extrapolated to other high-metallicity galaxies. The situation for low metallicity galaxies is rather complicated; since the opacity of the galaxy decreases, MIR would be unable to trace most of the UV/optical photons and thus lose the ability as an SFR indicator (Calzetti et al. 2007).

2.4.4 AGNs

Although AGNs have distinct features from normal galaxies in various physical properties, they share the same trend in the MIR-SFR diagrams (Figures 2.12 and 2.13). A possible reason is that the contribution from AGN component is minor (from SED fitting, less than 15%), therefore the host galaxy component dominates the spectrum. To investigate the effect of AGNs on MIR emission, we plot average SEDs for AGNs and normal galaxies in Figure 2.19. On average, AGNs are brighter than normal galaxies at all bands, whereas with a lower MIR/90 μm ratio (Table 2.8). There are two possible reasons: 1. silicate absorption occurs more strongly in AGNs. 2. PAH molecules are destroyed by the harsh radiation field in AGNs. The

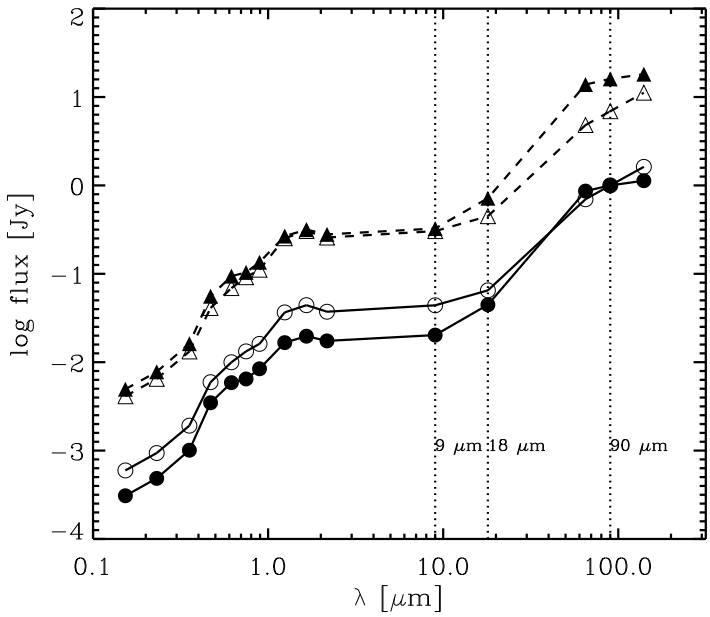

Figure 2.19 The average SED (dashed lines) and the SED normalized at 90 μm (solid lines) of AGNs (solid symbols) and normal galaxies (open symbols).

latter is more convincing. Studies show that small PAH molecules which contribute to shorter wavelength MIR emission are destroyed more easily than the large ones which contribute to longer wavelength MIR emission (Smith et al. 2007b; Treyer et al. 2010, and references therein), which is consistent with the lower 9 μm flux value than 18 μm one in Figure 2.19. Nevertheless, these differences between AGNs and normal galaxies are only on their average level, and they can not be used to distinguish AGNs from normal galaxies in individual cases.

2.5 Conclusions

We combined AKARI/IRC 9 μm and 18 μm data with a previous sample to construct a FIR-selected multi-wavelength sample with MIR photometric measurements. The FIR data of AKARI/FIS in the original sample were re-estimated by photometry

of AKARI diffuse maps to correct the bias of PSF photometry for extended sources. Then, the SEDs of the sample were fitted by CIGALE, and the SFRs were obtained. Regression analysis was conducted to investigate MIR-SFR relations. SFRs converted from AKARI MIR fluxes were compared with those from the Spitzer MIR fluxes to test the reliability of the AKARI MIR-SFR calibrations. From the results, we draw the following conclusions:

1. Both 9 μm and 18 μm luminosities correlate with SFRs, and thus could be converted to SFRs.

2. A combination of FUV and MIR luminosities barely reduces the scatters, indicating that the unobscured UV photons are not the only reason of the variation of the MIR-SFR relation.

3. A comparison of the SFRs derived from Equations 2.7 and 2.8 with the ones derived from the Spitzer MIR-SFR relations shows that the silicate absorption included in *S9W* (9 μm) and *L18W* (18 μm) bands little affects the results. The discrepancies, if any, are well within the uncertainties.

4. AGNs in the sample show no discrepancy with normal galaxies in the MIR-SFR diagrams. The smaller average MIR fluxes for AGNs than normal galaxies might indicate the small PAH molecules are destructed by harsh radiation from AGNs.

In summary, for IR selected galaxies the rest frame 9 μm and 18 μm emissions are efficient tracers of SFRs, and the equations derived here should be applicable to other dust-rich galaxies.

Table 2.5 SFR calculations based on Spitzer data. The luminosity is expressed in $L_\odot$ and SFR in $M_\odot$/yr.

Work	SFR calculation
Wu et al. (2005)	$\log \mathrm{SFR} = (1.09 \pm 0.06) \log L_8 - (10.03 \pm 0.16)$
Zhu et al. (2008)	$\log \mathrm{SFR} = (0.93 \pm 0.03) \log L_8 - (8.59 \pm 0.08)$
Wu et al. (2005)	$\log \mathrm{SFR} = (0.89 \pm 0.06) \log L_{24} - (7.82 \pm 0.17)$
Calzetti et al. (2007)*	$\log \mathrm{SFR} = 0.8850 \log L_{24} - 8.17$ (1 σ uncertainty 0.03)
Zhu et al. (2008)	$\log \mathrm{SFR} = (0.85 \pm 0.01) \log L_{24} - (7.47 \pm 0.06)$
Rieke et al. (2009)	$\mathrm{SFR} = 7.8 \times 10^{-10} L_{24}$ for $6 \times 10^8 \leq L_{24} \leq 1.3 \times 10^{10}\ L_\odot$ $\mathrm{SFR} = 7.8 \times 10^{-10} L_{24} \times (7.76 \times 10^{-11} L_{24})^{0.048}$ for $L_{24} > 1.3 \times 10^{10}\ L_\odot$

* For galaxies with 12 + log(O/H) > 8.35, i.e., "high metallicity" galaxies in Calzetti et al. (2007).

Table 2.6 Regression coefficients between SFRs derived from AKARI 9 μm and from Spitzer 8 μm: $\log \mathrm{SFR}(8\ \mu\mathrm{m}) = a + b \log \mathrm{SFR}(9\ \mu\mathrm{m})$ and the mean value of the difference: $\Delta\,\mathrm{SFR} = < \log \mathrm{SFR}(8\ \mu\mathrm{m}) - \log \mathrm{SFR}(9\ \mu\mathrm{m}) >$. C.c is the value of the correlation coefficient.

8 μm calibration	a	b	C. c	$\Delta\,\mathrm{SFR}$
Wu et al. (2005)	-0.17 ± 0.02	1.05 ± 0.03	0.968	-0.14 ± 0.18
Zhu et al. (2008)	-0.20 ± 0.02	0.90 ± 0.02	0.968	-0.25 ± 0.16

Table 2.7 Regression coefficients between SFRs derived from AKARI 18 μm and from Spitzer 24 μm: $\log \mathrm{SFR}(24\ \mu\mathrm{m}) = a + b \log \mathrm{SFR}(18\ \mu\mathrm{m})$ and the mean value of the difference: $\Delta\,\mathrm{SFR} = < \log \mathrm{SFR}(24\ \mu\mathrm{m}) - \log \mathrm{SFR}(18\ \mu\mathrm{m}) >$. C.c is the value of the correlation coefficient.

24 μm calibration	a	b	C. c	$\Delta\,\mathrm{SFR}$
Wu et al. (2005)	-0.02 ± 0.02	1.00 ± 0.02	0.982	-0.01 ± 0.12
Calzetti et al. (2007)	-0.23 ± 0.02	1.00 ± 0.02	0.982	-0.23 ± 0.12
Zhu et al. (2008)	-0.02 ± 0.02	0.96 ± 0.02	0.982	-0.05 ± 0.11
Rieke et al. (2009)	-0.14 ± 0.02	1.14 ± 0.02	0.982	-0.04 ± 0.17

Table 2.8 The MIR to 90 μm flux ratio for AGNs and normal galaxies.

Gal.	$\log(f_9/f_{90})$	$\log(f_{18}/f_{90})$	$\log(f_9/f_{18})$
AGN	-1.69	-1.35	-0.34
Normal	-1.35	-1.19	-0.16

Chapter 3

SFR calibrations using WISE luminosities: A Theoretical Study from UV to FIR Data by CIGALE

3.1 Introduction

The Wide-field Infrared Survey Explorer (WISE) funded by NASA provides all-sky mid-infrared data at ∼3.4, 4.6, 12 and 22 μm (named as W1, W2, W3, and W4) with extremely high sensitivity and resolution (Wright et al. 2010): It has a sensitivity of 0.08, 0.11, 1 and 6 mJy and an angular resolution of 6.1″, 6.4″, 6.5″, and 12.0″ in the four bands. With these properties, WISE can observe much deeper and fainter objects than previous IR surveys. The data of WISE are being released since April 2011, and soon the all-sky data will be open to public. WISE is expected to produce exciting results about the most luminous galaxies. The ability of WISE can observe ultra-luminous infrared galaxies (ULIRGs) till redshift ~ 3. WISE also provides an unprecedented opportunity to study the star formation and galaxy evolution in the universe. Therefore, SFR calibrations using WISE filters are necessary to interpret WISE data, and have important applications when investigating the evolution of galaxies.

In this chapter, we use multiwavelength data and spectral energy distribution

(SED) fitting method to construct spectral templates and obtain calibrations of SFR for WISE bands from local to high redshift universe. We then compare the template predictions with observational data to examine the reliability and efficiency of our method.

3.2 Data

3.2.1 The Local Sample

For the local galaxy sample, we make use of the sample of star forming galaxies built in Chapter 2. Here, we update the AKARI BSC and IRC fluxes with the newest version. IRC fluxes are not changed in the newest version. Figure 3.1 shows a comparison of IRAS fluxes with those from old version BSC, new version BSC and diffuse maps. The horizontal lines are the differences between IRAS and AKARI bands predicted by Dale & Helou (2002) (hereafter DH, see also Chapter 2) models. Lines in Figure 3.1 show $\alpha = 1.375$, 2.625 and the median value 2.0. Apparently, IRAS fluxes agrees better with the newest version than with the previous version. The sample is divided into two groups according to the SDSS g-band images. The one with major axis less than the point spread function (PSF) size is considered as a point source, otherwise it is an extended source. At 65 and 90 μm bands, there are apparent discrepancies between IRAS and AKARI BSC measurements for the extended sources even for the newest version. These discrepancies are due to the underestimation of extended fluxes by PSF fitting method. The corrections for the extended sources are still necessary. Therefore, fluxes for extended sources at 65 and 90 μm are adopted from the diffuse map fluxes. A summary of the data is listed in Table 3.1.

3.2.2 The High Redshift Samples

The higher redshift samples are taken from the COSMOS multiwavelength data constructed by Kartaltepe et al. (2010). The COSMOS field is the largest contiguous

Figure 3.1 A comparison of IRAS fluxes with fluxes from the old version of BSC (black), the new version of BSC (red) and the diffuse maps (blue). Point sources are shown as small circles, and extended sources are shown as large circles.

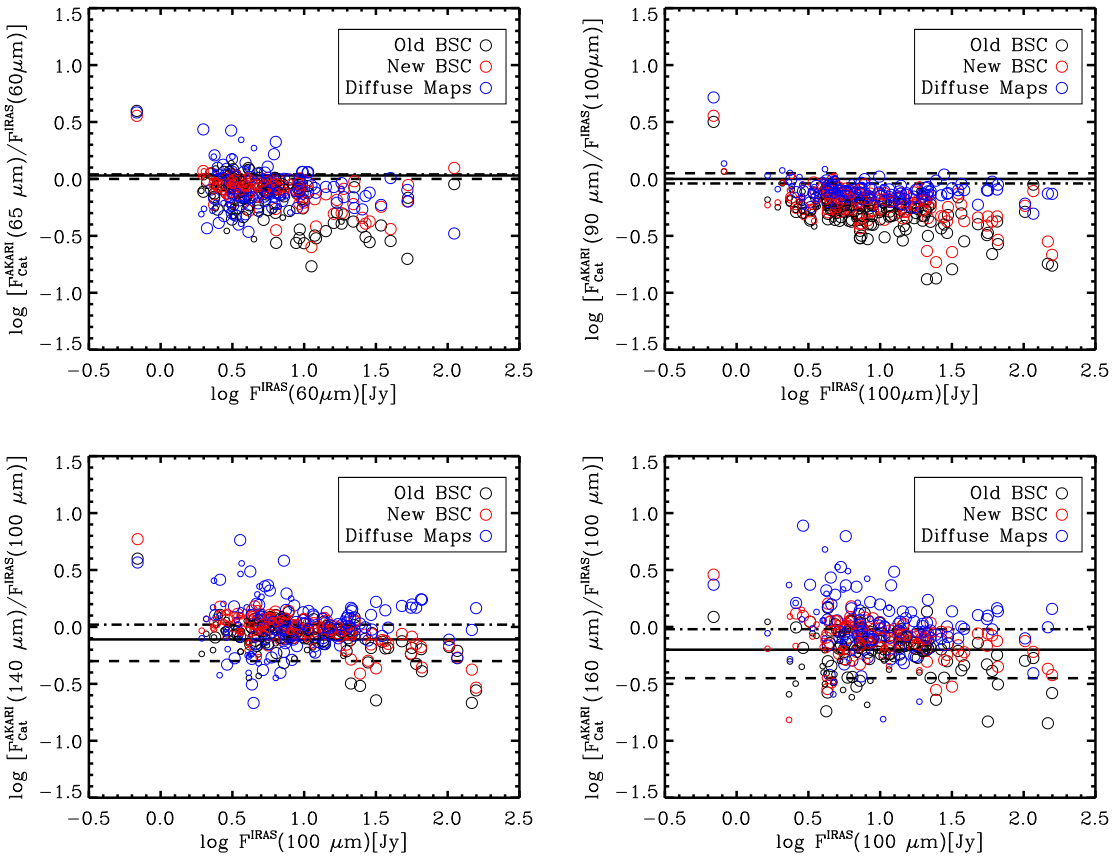

Table 3.1 A brief summary of the local sample. The numbers of galaxies observed in each band are different from Table 2.1 in Chapter 2 is due to the updating of the BSC.

Survey	Band	Wavelength (μm)	number
GALEX	FUV, NUV	0.153, 0.231	156
SDSS	*u*, *g*, *r*, *i*, *z*	0.355, 0.469, 0.617, 0.748, 0.893	156
2MASS	*J*, *H*, *Ks*	1.244, 1.655, 2.169	156
AKARI IRC	*S9W*	9	126
AKARI IRC	*L18W*	18	108
AKARI FIS	*N60*, *Wide-S*	65, 90	156
AKARI FIS	*Wide-L*	140	154
AKARI FIS	*Wide-L*	160	155

field (2 square degree) ever observed by Hubble Space Telescope (HST), and has rich data covering the whole spectrum because of the follow-up observations (Scoville et al. 2007; Kartaltepe et al. 2010). These observations include the VLA radio telescope, ESO's VLT in Chile, ESA's XMM X-ray satellite, and Japan's 8-meter Subaru telescope in Hawaii. COSMOS will detect over 2 million objects with $I_{AB} > 27$ mag, over 35,000 Lyman Break Galaxies (LBGs), extremely red galaxies out to $z \sim 5$. These data will provide huge amount of information on formation and evolution of galaxies and large scale structure of the universe.

Galaxies in the sample are selected at 70 μm with the signal to noise ratio S/N > 3. There are 1503 galaxies in the original sample, 602 of which have spectroscopic redshifts. We choose galaxies at certain redshifts: around 0.5, 1.0, 1.5, 2.0, 2.5, in order to compare with the local templates extrapolated to high redshifts (see section 3.3). Tables 3.2 and 3.3 list the properties of the sample. Details on how the sample is constructed can be found in Kartaltepe et al. (2010).

Table 3.2 Photometric bands of the higher redshift sample.

Survey	Band	Wavelength (μm)
GALEX	FUV, NUV	0.153, 0.231
CFHT/MEGACAM	u^*	0.374
Subaru/SuprimeCam	$B_J V_J g^+ r^+ i^+ z^+$	0.448, 0.549, 0.481, 0.631, 0.771, 0.905
UKIRT/WFCAM	J	1.25
CFHT/WIRCAM	K_S	2.15
Spitzer/IRAC	band 1, 2, 3, 4	3.5, 4.5, 5.6, 8.0
Spitzer/MIPS	band 1, 2, 3	24, 70, 160

Table 3.3 The numbers and redshifts of galaxies in each subsample. For redshift greater than 1, we also add galaxies with photometric redshift only.

Group	Redshift	Number
1	$0.4 < z < 0.6$	88
2	$0.9 < z < 1.1$	47
3	$1.4 < z < 1.6$	6+45
4	$1.9 < z < 2.1$	6+13
5	$2.4 < z < 2.6$	1+3

3.3 Method

3.3.1 SED templates

We use CIGALE to fit the galaxies. CIGALE has already been introduced in Section 2.3. Here we introduce stellar populations used in this work, which are different from those in Chapter 2.

As mentioned in Section 2.3, CIGALE allows one to apply different SFH and dust attenuation parameters for two different stellar populations. In order to test the effect of introducing these parameters, we apply two senarios to fit the data. First, we assume there is only one stellar population with an exponetially decreasing star formation; second, we take two stellar populations, i.e, a burst component which forms stars continually for a certain period is added. We find that the WISE fluxes at each band predicted by these two methods are closely correlated with each other, and the output parameters are also consistent with each other. Although using two stellar populations can give a closer fitting to the observation data, it also causes more degeneracy. Considering that using one stellar population is sufficient to give a satisfying fit, we choose to use one stellar population in the present work.

The input parameters used in this work are shown in Table 3.4.

Output parameters are computed by Bayesian approach. The code calculates probability distribution functions (PDFs) by taking sums of probability of the models in given bins of the parameter space. Similar as in Chapter 2, the expectation value of each parameter $\langle\ x\ \rangle$ is given by:

$$\langle\ x\ \rangle\ =\ \frac{\Sigma_{i=1}^{b} P_i x_i}{\Sigma_{i=1}^{b} P_i}, \tag{3.1}$$

and the standard deviation σ is obtained by:

$$\sigma_x\ =\ \sqrt{\frac{\Sigma_{i=1}^{b} P_i (x_i\ -\ \langle\ x\ \rangle)^2}{\Sigma_{i=1}^{b} P_i}}, \tag{3.2}$$

where b is the number of bins in the parameter space.

Table 3.4 List of input parameters for CIGALE.

parameters	input values
τ	0.001 0.01 0.1 1. 3. 5. 10.
ages	0.05 0.1 0.3 0.5 1. 3. 5. 10. 13.
δ	-0.3 -0.15 0. 0.15 0.3
A_V	0.0 .15 .30 .45 .60 .75 .90 1.05 1.20 1.35 1.5 1.65 1.8 1.95 2.1 2.25
α	1.0 1.25 1.5 1.75 2.0 2.25 2.5 2.75 3.0
AGN fraction	0. 0.05 0.1 0.25 0.3

3.3.2 Template construction and flux calculation

Apart from deriving physical properties of galaxies, SED fitting of CIGALE also gives the entire UV to FIR spectrum of the best fitting model (the model with minimum χ^2 value) of each galaxy. Hence, assuming a galaxy with a spectrum $S(\nu)$, we can obtain the flux observed at filter $R(\nu)$:

$$F(\nu) = \frac{\int S(\nu)R(\nu)\,d\nu}{\int R(\nu)\,d\nu}. \tag{3.3}$$

The redshifted spectra are calculated by transforming λ to $\lambda(1+z)$. The best models of local galaxies are used as templates to construct the mock samples at higher redshifts. Assuming there is no strong evolution in the characteristic temperature of the color distribution over $0 < z < 2.5$ for far-IR galaxies, we construct mock galaxy samples at z from 0.5 to 2.5 with a step of 0.5. This redshift range is chosen because the redshift limit of WISE for ULIRGs is ~ 3 (Wright et al. 2010).

3.3.3 The reliability of the results

After running CIGALE to obtain the best models for all galaxies, a mock sample of galaxies is generated based on the method from Giovannoli et al. (2011). Then, the output parameters of CIGALE for these mock galaxies are compared to the best models to check the reliability of the results (Figure 3.2). The method has been introduced in Section 2.3.

Figure 3.2 shows the correlations between parameters derived from CIGALE based

on the real and mock galaxies. Except δ, the slope of the modified Calzetti Law (see Section 2.3), other parameters are all well constrained by CIGALE.

3.4 Results and Conclusions

Figures 3.3 and 3.4 show the correlations between the WISE band luminosities and SFRs at different redshifts. It can be seen that the correlations are very tight from local to redshift 2.5 for mock galaxies, implying the W3 and W4 bands are good tracers of SFRs even at redshift $\sim$2.5. The SFR calibrations are shown in the lower right corner in each panel.

The results derived from mock galaxies show little discrepancy with those derived from the COSMOS galaxies at redshifts < 1. The discrepancy becomes larger at redshift higher than 1, where most of galaxies have only photometric redshifts. Further tests are necessary to check whether it is due to the insufficient accuracy of the photometric redshifts.

We also compare our SFR calibrations derived from templates with previous studies by Elbaz et al. (2002), Takeuchi et al. (2005b), Reddy et al. (2010) and Wu et al. (2005). Their calibrations are based on observation data at different redshifts. Table 3.5 shows their results. Figure 3.4 shows our calibrations are consistent with these results. Future work will focus on applying these calibrations to the observation data of WISE.

Figure 3.2 Correlations between CIGALE output parameters (code) based on the real data and mock galaxies.

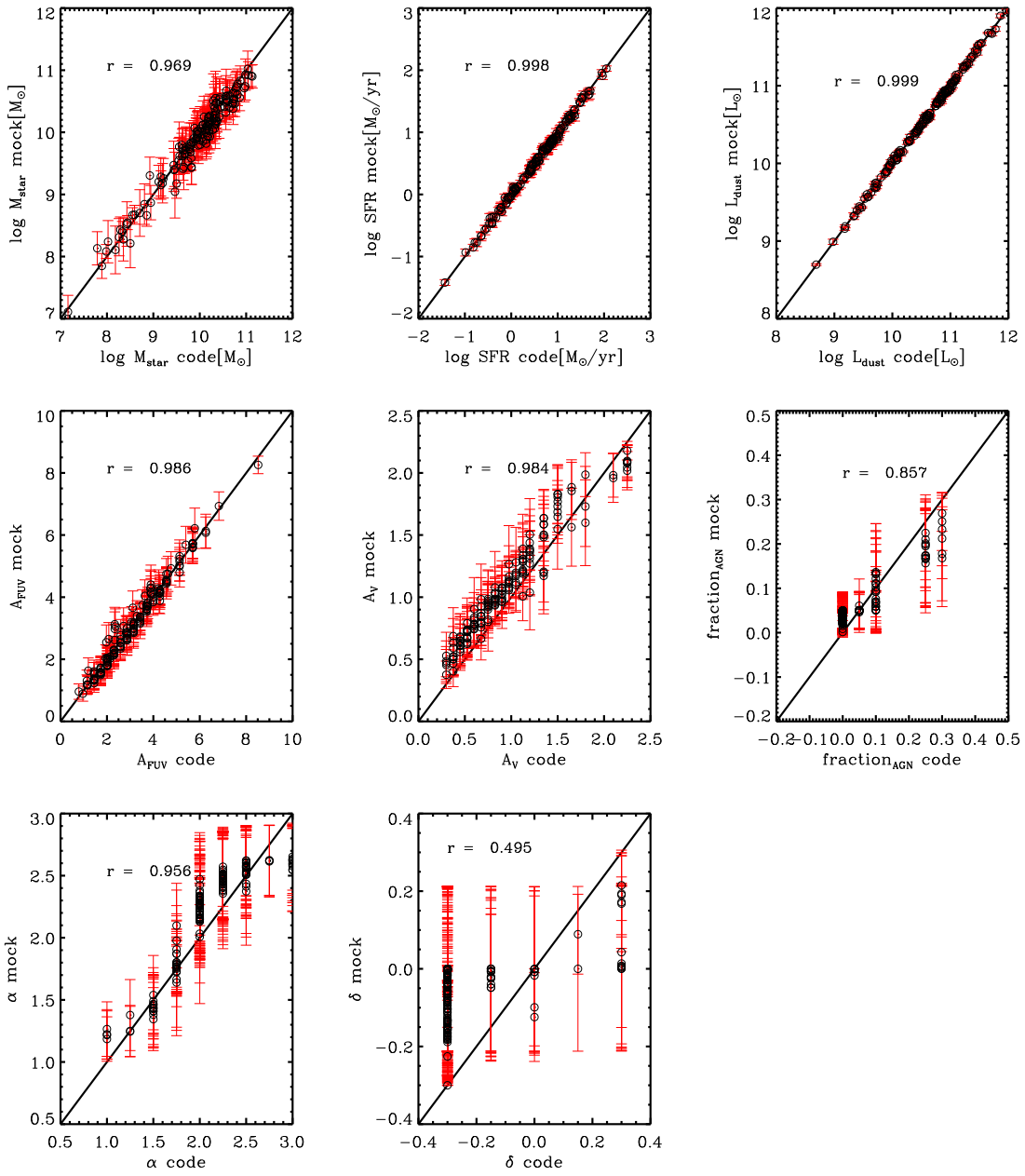

Figure 3.3 Correlations between the W3 band luminosities and SFRs at different redshifts for the mock galaxies based on the local GALEX-SDSS-2MASS-AKARI sample (black dots) and for the galaxies in the COSMOS field selected by Kartaltepe et al. (2010) having spectroscopic redshifts (green dots) and photometric redshifts (red dots). The line in each figure presents the best fitting result.

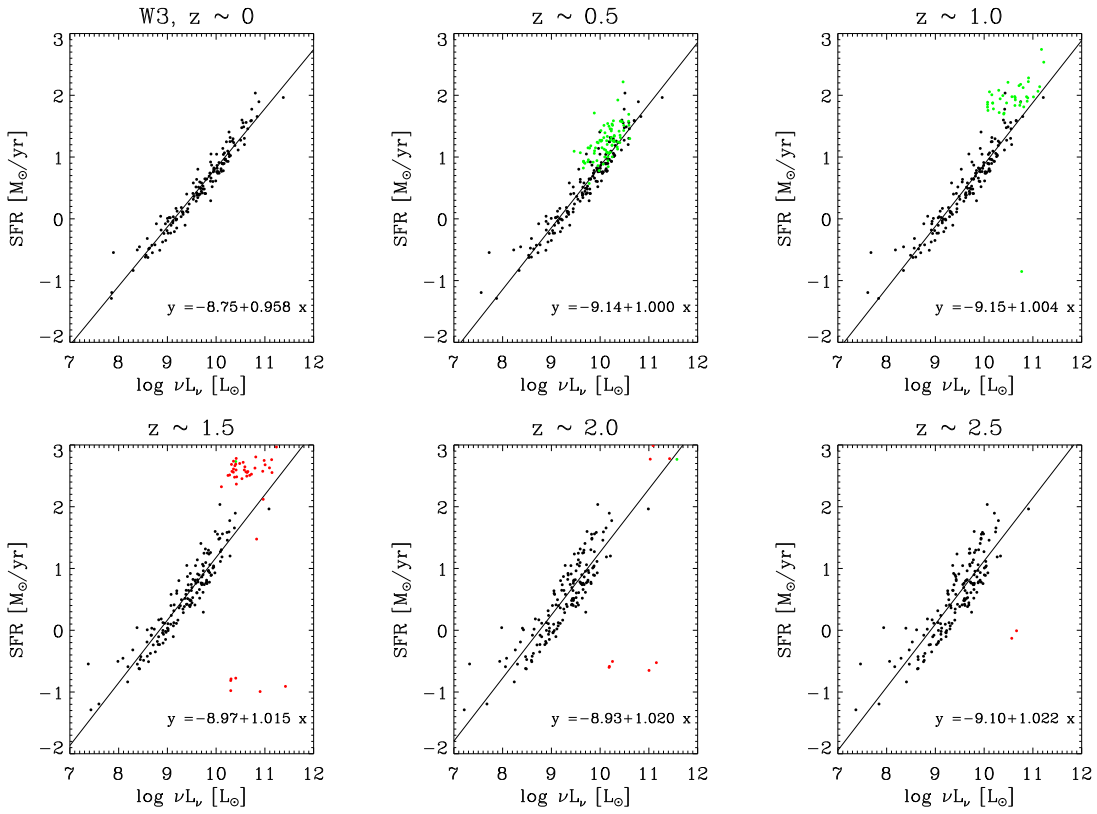

Figure 3.4 Correlations between the W4 band luminosities and SFRs at different redshifts. Symbols are similar to those in Figure 3.3. Previous results by Elbaz et al. (2002), Takeuchi et al. (2005b), Reddy et al. (2010) and Wu et al. (2005) are given as comparison.

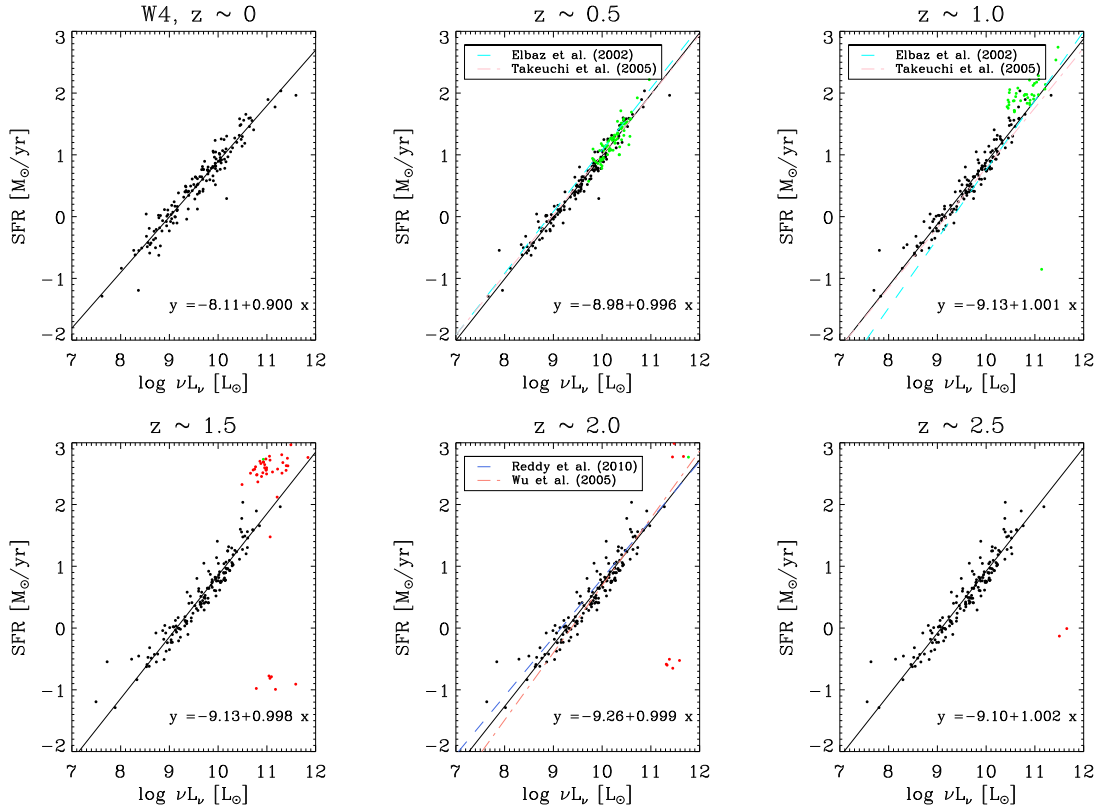

Table 3.5 SFR calibrations from previous studies. These calibrations are used to compare with our results at redshift 0.5, 1 and 2 in Figure 3.4. The luminosity is expressed in $L_\odot$ and SFR in $M_\odot$/yr.

Work	SFR calibrations	sample
$z \sim 0.5$		
Elbaz et al. (2002)	$\log \mathrm{SFR} = 0.998 \log L_{12} - 8.722$	ISO 15 μm, local
Takeuchi et al. (2005b)	$\log \mathrm{SFR} = 0.972 \log L_{12} - 8.54$	ISO 15 μm, local
$z \sim 1$		
Elbaz et al. (2002)	$\log \mathrm{SFR} = 1.12 \log L_{12} - 10.26$	ISO 12 μm, local
Takeuchi et al. (2005b)	$\log \mathrm{SFR} = 0.972 \log L_{12} - 8.75$	ISO 12 μm, local
$z \sim 2$		
Wu et al. (2005)	$\log \mathrm{SFR} = 1.09 \log L_8 - 10.03$	Spitzer 8 μm, local
Reddy et al. (2010)	$\log \mathrm{SFR} = 0.95 \log L_{24} - 8.52$	Spitzer 24 μm, $z \sim 2$

* For galaxies with $12 + \log(\mathrm{O/H}) > 8.35$, i.e., "high metallicity" galaxies in Calzetti et al. (2007).

Chapter 4

Dust Attenuation and Star Formation in Major Merger Galaxies

Merger processes play an important role in galaxy formation and evolution. In order to study the influence of merger processes on the evolution of dust properties and cosmic star formation rate, we investigate a local sample of major merger galaxies and a control sample of isolated galaxies using GALEX ultraviolet (UV) and Spitzer infrared (IR) images.

4.1 Introduction

In the hierarchical scenario of galaxy and structure formation, interactions between galaxies and their associated dark matter halos happen frequently (e.g Cole et al. 2000; Wechsler et al. 2002; Li et al. 2007; Freedman Woods et al. 2010), and can strongly affect galaxy properties such as morphology, luminosity, star formation rate (SFR), and dust properties (e.g. Struck 2006; Hwang et al. 2011). Hence, it is quite important to consider the effects of galaxy-galaxy interaction when studying the evolution of galaxies.

Merging of two galaxies occurs if the orbital energy of the two interacting galaxies

is low enough. Mergers play a very important role in the formation and evolution of galaxies and their dark matter halos. Simulations show that during the merging process of gas-rich galaxies, the gas flows inward and causes a starburst in the nuclear region (e.g. Toomre & Toomre 1972). Although mergers are thought to be connected with starburst and AGN activity, the details are still not clear, and several key questions related to mergers still remain to be solved (Mo et al. 2010).

One of the questions is related to the strong evolution of the cosmic star formation density from $z = 0$ to $z = 1$ (e.g. Lilly et al. 1996; Madau et al. 1998; Hopkins 2004; Takeuchi et al. 2005a)). A change of merger rate at higher redshift could be responsible for this evolution (Zheng et al. 2004; Hammer et al. 2005; Bridge et al. 2007). However, there are also works against this conclusion. These works found that the merger rate does not evolve much from $z \sim 0$ to $z \sim 1$ and the properties that do not strongly affect galaxy morphology should be responsible for the evolution (Flores et al. 1999; Bell et al. 2005; Melbourne et al. 2005; Lotz et al. 2008). Therefore, a quantitative study is still necessary to solve this problem.

Xu et al. (2010) claim that the different results mentioned above may be caused by different selection methods. There are two common methods to select merger galaxies, both with pros and cons. One is to select peculiar galaxies. With images provided by high resolution telescopes (e.g *HST*), this method can select galaxies at a late stage of merging to quite high redshift. However, it is uncertain whether all peculiar galaxies are in a merging state: some of them are isolated galaxies showing irregular star formation regions. The patchy distribution of dust can strongly affect the light distribution and make this method of identification problematic, especially in ultraviolet (UV) bands (Burgarella et al. 2001). Another disadvantage of this method is that the signature of the disturbed features becomes harder to detect as one goes deeper in space (Mo et al. 2010; Xu et al. 2010).

The other approach is to select close pairs, assuming that these pairs will ultimately merge within a certain time scale. This method avoids the complex identification of morphological features, and thus is more objective. However, it suffers from biases such as: (1) the projection effect; (2) missing very close pairs due to the low resolution of the telescope; (3) missing less luminous components given a certain

magnitude limit ('missing the secondary') (Xu et al. 2004, 2010).

In order to reduce these biases, Xu et al. (2010) (hereafter Xu10) built a local sample of close pairs selected from near-infrared bands by carefully choosing selection criteria (See Section 4.2.1). Using this sample and Spitzer observation data, they found an apparent enhancement of star formation rates in mergers and discussed in detail the dependence of the enhancement on morphology, mass, and separation of these galaxies. Their work is less affected by dust extinction compared with previous studies based on UV and optical bands (e.g. Barton et al. 2000; Woods et al. 2006; Ellison et al. 2008), and has better resolution than previous infrared (IR) works (e.g. Kennicutt et al. 1987; Telesco et al. 1988; Xu & Sulentic 1991). Compared with Smith et al. (2007a), which looked into interacting features such as bridges and tails in resolved pairs using Spitzer data, Xu10 sampled galaxies with and without strong interacting features.

Xu10's sample provides a good opportunity to study the physical properties of local merger galaxies. One important property is dust attenuation. It changes the spectral energy distribution of a galaxy and is correlated with SFR (e.g Burgarella et al. 2006; Iglesias-Páramo et al. 2006; Garn & Best 2010). Dust attenuation in major mergers can be quite complex and different from that in isolated galaxies: merging processes can inject gas into a galaxy and enhance the gas content (Hernquist & Barnes 1991; Barnes & Hernquist 1996), but it can also dissipate gas through hydrodynamic effects (Park & Choi 2009). Previous works about dust attenuation in merger galaxies are mostly based on theoretical modeling and numerical simulations (e.g. Bekki & Shioya 2000; Goldader et al. 2002). Although Hwang et al. (2011) study dust properties using Herschel data, their work is confined to IR bands. Since dust attenuation of galaxies can be accurately investigated usijng UV and IR data (e.g. Meurer et al. 1999; Buat et al. 2005; Burgarella et al. 2006; Cortese et al. 2008; Boquien et al. 2012), we aim to combine UV and IR data to statistically investigate the dust attenuation of major merger galaxies.

Meurer et al. (1999) found a tight correlation between the fraction of IR to UV luminosity $L_{\rm IR}/L_{\rm UV}$ and the slope of UV spectra β (IRX-β relation) for starburst galaxies. However, later studies show that this relation applies only to starburst

galaxies and changes for more quiescent galaxies (Kong et al. 2004; Cortese et al. 2008; Muñoz-Mateos et al. 2009, etc.). Recently, Takeuchi et al. (2012) found that the IRX-β relation needs to be corrected for the aperture effect. This relation can be used to calculate the dust attenuation when there is no IR data available, and therefore is of great importance. In this paper we also examine the application of this relation to major merger galaxies.

If dust attenuation in merger galaxies differs from isolated galaxies statistically, Xu10's result on SFRs may be biased because they used only IR data and ignored the effect of unobscured SFRs which can be obtained from UV observations. Takeuchi et al. (2005a) have shown that the SFRs indicated by UV emission contribute about 50% of the cosmic star formation density in the local universe, implying unobscured SFRs are quite important for local galaxies. Therefore, it is possible that Xu10's results are biased due to their not accounting for UV emission. To give an unbiased view of the SFR, it is necessary to consider both the obscured and unobscured emission from young stars, namely, IR and UV emission (see Buat & Xu 1996; Hirashita et al. 2003; Takeuchi et al. 2010, etc.). Hancock et al. (2008) studied the UV and mid-infrared properties of interacting galaxies, but they only focused on the single case of Arp82 and its merging features.

In this paper, we investigate dust attenuation of paired galaxies from Xu10's sample, and re-estimate the SFRs of paired galaxies by combining the IR and UV parts SFRs. The structure of our paper is as follows. First, we introduce the sample selection and the flux estimation of IR and UV images in Section 4.2. Then we discuss the results of dust attenuation, the dependence of the attenuation on different parameters, and the IRX-β relation in Section 4.3. In Section 4.4 we calculate SFRs and specific star formation rates (SSFRs) indicated by UV and IR, and compare the results with previous works. The nuclear contributions to SFRs are also discussed. Section 4.5 is a discussion on the importance of including SFRs indicated by UV. Our summary and conclusion are given in Section 4.6. In order to compare the results with Xu10, in this chapter the Λ-dominated flat cosmology is adopted: $\Omega_m = 0.3$, $\Omega_\Lambda = 0.7$, and $H_0 = 75\ \mathrm{km\,s^{-1}\,Mpc^{-1}}$.

4.2 Data

4.2.1 Pair selection

The pair and control samples are taken from Xu10. This pair sample includes all spectroscopically confirmed spiral-spiral (S-S) and spiral-elliptical (S-E) pairs in a parent sample that is complete for primaries brighter than K= 12.5 mag, projected separations between $5h^{-1}$ kpc and $20h^{-1}$ kpc and mass ratio $\leq$ 2.5. Here we give a short summary of their selection method. The details can be found in Xu et al. (2004), Domingue et al. (2009) and Xu10. The paired galaxies are selected from a parent sample of cross-matches between the 2MASS K_s Extended Source Catalog (XSC; Jarrett et al. (2000)) and the galaxy catalog of SDSS-DR3 (Abazajian et al. 2005). Then three steps are carried out to obtain the final sample. For the first step, the galaxies should satisfy the following conditions: 1) The magnitude $K_s > 13.5$ mag, where 13.5 mag is the completeness limit of XSC; 2) The selected galaxy should be in the region where SDSS-DR3 has good spectroscopic coverage: more than 50% of the galaxies within a 1 degree radius of a selected galaxy must have measured redshifts.

In the second step, the following criteria are used to select pairs: 1) The K_s magnitude of the primary is brighter than 12.5 mag; 2) The magnitude difference between the primary and the secondary is no greater than 1 mag. The first criterion ensures that the selected secondary is brighter than the magnitude limit and avoids the 'missing the secondary' bias. This criterion also confines the mass ratio between the primary and secondary, and thus ensures the selected pairs are in major mergers. 3) At least one component has a spectroscopic redshift; 4) The projected separation is between $5h^{-1}$ kpc and $20h^{-1}$ kpc. Limiting the projected separation to this range is to make our sample more comparable to high redshift samples. Too small a separation at high redshift will be hardly distinguishable, while a large separation will increase the possibility of including chance pairs (Kartaltepe et al. 2007). 5) The velocity difference is less than 500 km s^{-1}.

In the third step, a morphology selection is carried out to leave only spiral-spiral

(S-S) or spiral-elliptical (S-E) pairs in the sample. Elliptical-elliptical pairs are discarded because optical evidence shows that these galaxies have little star formation activity. To ensure the accuracy of the analysis, the pairs in which only one component has a measured redshift are also excluded after examining their SDSS images and finding no special characteristics compared to the total sample. Finally, there are 54 galaxies (27 pairs) left in the final sample, 39 of which are non-AGN spirals.

To find out how much difference the interaction between galaxies in pairs makes, a sample of isolated galaxies without such interactions needs to be constructed for comparison. Here we adopt Xu10's control sample. The criteria to select galaxies in the control sample are as follows: the isolated galaxies must be non-AGN late type galaxies in the local universe ($z \leq 0.1$) with both IRAC and MIPS data, and have K_s band magnitudes less than 13.5 mag. For each non-AGN spiral galaxy in a pair sample, one isolated galaxy with a similar mass ($\Delta \log M \leq 0.1$) and the closest redshift is matched to it. Although there is a difference in redshift between one galaxy in a pair sample and its isolated counterpart, Xu10 have already proved that the difference will not introduce any bias. We use Xu10's control sample based for the following reasons: 1) Xu10's control sample is matched to the non-AGN spiral galaxies in the pair sample one by one, which is very convenient to study the difference between each galaxy in the pair sample and its counterpart in the control sample; 2) by adopting their control sample, the comparison with their results is more direct, which makes it easier to see the influence of including the UV part of SSFRs. The redshifts z and stellar masses M of the galaxies in the control sample and the paired galaxies they are matched to are shown in Table 4.1.

Previous studies on S-E pairs (e.g de Mello et al. 1996; Domingue et al. 2003) have found that interactions with late-type galaxies can provoke star formation activity in an early-type galaxy. Indeed, there is one elliptical galaxy (J10514368+5101195) in our sample showing significant signs of star formation. However, since the number is small, we focus on spiral galaxies in this study.

Table 4.1 Physical properties of control galaxies and their counterparts in pairs (Xu10).

ID	z	$\log M$ ($M_\odot$)	Pair Galaxy ID	z	$\log M$ ($M_\odot$)	CAT	SEP	separation (kpc)
LCK-287434	0.0320	10.88	J00202580+0049350	0.0176	10.84	SE2	0.50	9.44
LCK-178064	0.0450	11.15	J01093517+0020132	0.0447	11.05	SE2	1.12	19.02
LCK-320371	0.0471	10.96	J01183556-0013594	0.0475	10.93	SS2	1.06	20.18
LCK-523686	0.0452	10.94	J02110832-0039171	0.0199	10.98	SS1	0.56	8.89
LCK-415950	0.0317	11.37	J09374413+0245394	0.0230	11.46	SE1	0.68	17.29
LCK-086596	0.0470	10.86	J10205188+4831096	0.0531	10.88	SE2	0.88	17.64
EN1-158103	0.0298	10.70	J10272950+0114490	0.0223	10.73	SE2	0.65	9.28
EN1-360222	0.0429	10.74	J10435053+0645466	0.0273	10.83	SS1	1.27	15.98
EN1-010947	0.0367	10.67	J10435268+0645256	0.0273	10.73	SS2	1.27	15.98
LCK-162208	0.0240	11.12	J10514450+5101303	0.0244	11.13	SE2	0.15	4.74
EN1-018834	0.0631	11.06	J12020424+5342317	0.0642	11.16	SE2	0.87	17.90
LCK-233199	0.0269	10.60	J13082964+0422045	0.0241	10.53	SS1	1.29	12.09
LCK-019297	0.0469	10.96	J13325525-0301347	0.0472	10.90	SS2	0.79	14.29
LCK-703238	0.0444	11.20	J13325655-0301395	0.0472	11.21	SS1	0.79	14.29
LCK-050667	0.0457	10.92	J13462001-0325407	0.0236	11.01	SE1	1.28	16.79
LCK-027930	0.0458	11.06	J14005782+4251207	0.0327	11.01	SS1	1.37	19.27
LCK-071868	0.0466	10.94	J14005882+4250427	0.0327	10.90	SS2	1.37	19.27
EN1-516050	0.0381	10.66	J14250739+0313560	0.0359	10.66	SE2	1.31	15.38
LCK-641925	0.0272	11.19	J14334683+4004512	0.0258	11.25	SS1	1.22	19.29
LCK-400414	0.0281	11.12	J14334840+4005392	0.0258	11.10	SS2	1.22	19.29
LCK-534543	0.0314	11.14	J15064391+0346364	0.0345	11.22	SS1	1.10	16.29
LCK-136060	0.0483	11.08	J15064579+0346214	0.0345	11.17	SS2	1.10	16.29
LCK-172179	0.0461	11.02	J15101587+5810425	0.0312	11.02	SS1	0.53	7.85
LCK-564807	0.0446	10.76	J15101776+5810375	0.0312	10.79	SS2	0.53	7.85
LCK-621286	0.0454	11.32	J15281276+4255474	0.0182	11.26	SS1	1.32	17.68
LCK-038716	0.0469	11.00	J15281667+4256384	0.0182	11.03	SS2	1.32	17.68
LCK-582705	0.0286	10.49	J15562191+4757172	0.0195	10.49	SE1	1.32	16.33
LCK-329416	0.0472	11.07	J16024254+4111499	0.0333	11.11	SS1	0.64	12.57
LCK-040350	0.0460	10.70	J16024475+4111589	0.0333	10.78	SS2	0.64	12.57
EN1-346329	0.0636	10.97	J17045089+3448530	0.0568	11.01	SS2	0.63	7.76
LCK-182514	0.0673	11.21	J17045097+3449020	0.0568	11.28	SS1	0.63	7.76
LCK-515902	0.0723	11.37	J20471908+0019150	0.0133	11.37	SE1	0.99	20.73
LCK-347435	0.0468	10.87	J13153076+6207447	0.0306	10.91	SS2	1.34	15.54
LCK-048281	0.0481	11.05	J13153506+6207287	0.0306	11.09	SS1	1.34	15.54
NGC0024	0.0019	9.63	J09494143+0037163	0.0063	9.71	SS2	2.04	15.49
NGC2403	0.0004	9.99	J09495263+0037043	0.0063	9.95	SS1	2.04	15.49
NGC0925	0.0018	10.06	J13082737+0422125	0.0241	10.15	SS2	1.29	12.09
NGC3049	0.0050	9.91	J14530282+0317451	0.0052	9.92	SS2	1.42	10.09
NGC3184	0.0020	10.31	J14530523+0319541	0.0052	10.17	SS1	1.42	10.09

4.2.2 Infrared data

The infrared fluxes of paired galaxies are taken from Xu10. The data are drawn from IRAC and MIPS observations. For IRAC images, they used two methods to calculate the fluxes. The first method is standard aperture photometry. The second method is to measure the total flux of the pair and that of the component that has a more regular morphology. The flux of the second component is thus the difference between the two fluxes. For MIPS, aperture photometry and point response function (PRF) fitting are used to calculate the fluxes.

The infrared luminosity $L_{\rm IR}$ is calculated using the 8 μm and 24 μm data:

$$\begin{aligned} \log(L_{\rm IR}[L_\odot]) &= \log(L_{24}[L_\odot]) + (0.87 \pm 0.03) \\ &\quad +(0.56 \pm 0.09)\log(L_8/L_{24}), \end{aligned} \tag{4.1}$$

where $L_\lambda = \nu L_\nu$ at λ μm. Although this estimation only uses mid-infrared data, it is consistent with the estimation given by Dale et al. (2005), where FIR data at 24, 70 and 160μm are used (Xu et al. 2010).

The infrared data of control galaxies are taken from Spitzer SWIRE fields (34 galaxies) and Spitzer SINGS samples (5 galaxies). The fluxes of galaxies in SWIRE fields are taken from the SWIRE Data Release 2 (Surace et al. 2005). Kron fluxes are adopted for both the 8 and 24 μm bands. For MIPS 24 μm fluxes, an additional 15% aperture correction is applied (Shupe et al. 2008). The fluxes of galaxies in SINGS sample are taken from Smith et al. (2007a).

4.2.3 Ultraviolet fluxes

Ultraviolet images are taken from the GALEX GR6 database using GALEXVIEW. We find FUV and NUV images for 24 of our pairs, but 3 pairs are not in the database. These images are shown in Figure 4.1. Two methods are carried out to measure the UV fluxes:

1. The method introduced in Section 2.2.1 is applied. An IDL photometry program is used to perform the GALEX photometry. Hereafter, we refer to this method

as manual photometry. The NUV images are used as the reference to detect sources. To carry out the photometry, one first needs to select a region by eye to confine the initial area where the photometry will be carried out. Then the program automatically searches for sources in this region and conducts aperture photometry using a set of elliptical apertures. The total flux density within the aperture is calculated where the growth curve converges. The NUV and FUV flux densities are corrected for Galactic extinction using a Schlegel map (Schlegel et al. 1998) and the Galactic extinction curve of Cardelli et al. (1989). A detailed description of this method can be found in Iglesias-Páramo et al. (2006).

2. As shown in Figure 4.1, the components in some pairs are extremely close to each other such that the manual program may not be able to rule out contamination from one component to the other when searching for the convergence radius. For these sources, classical aperture photometry is applied and elliptical apertures are used. In addition, source No.51 (upper right component of pair No.51-52) is quite extended. As a result, the manual photometry defines a smaller aperture which covers only about half of the entire source. Therefore, classical aperture photometry is also needed for this galaxy.

The results of the NUV and FUV photometry are shown in Table 4.2. The different methods of photometry applied to the sources are indicated as 'M' and 'A' for manual and aperture photometry, respectively. For the control sources, 38 sources are found in the GALEX image database. Manual photometry is applied and the results are shown in Table 4.3.

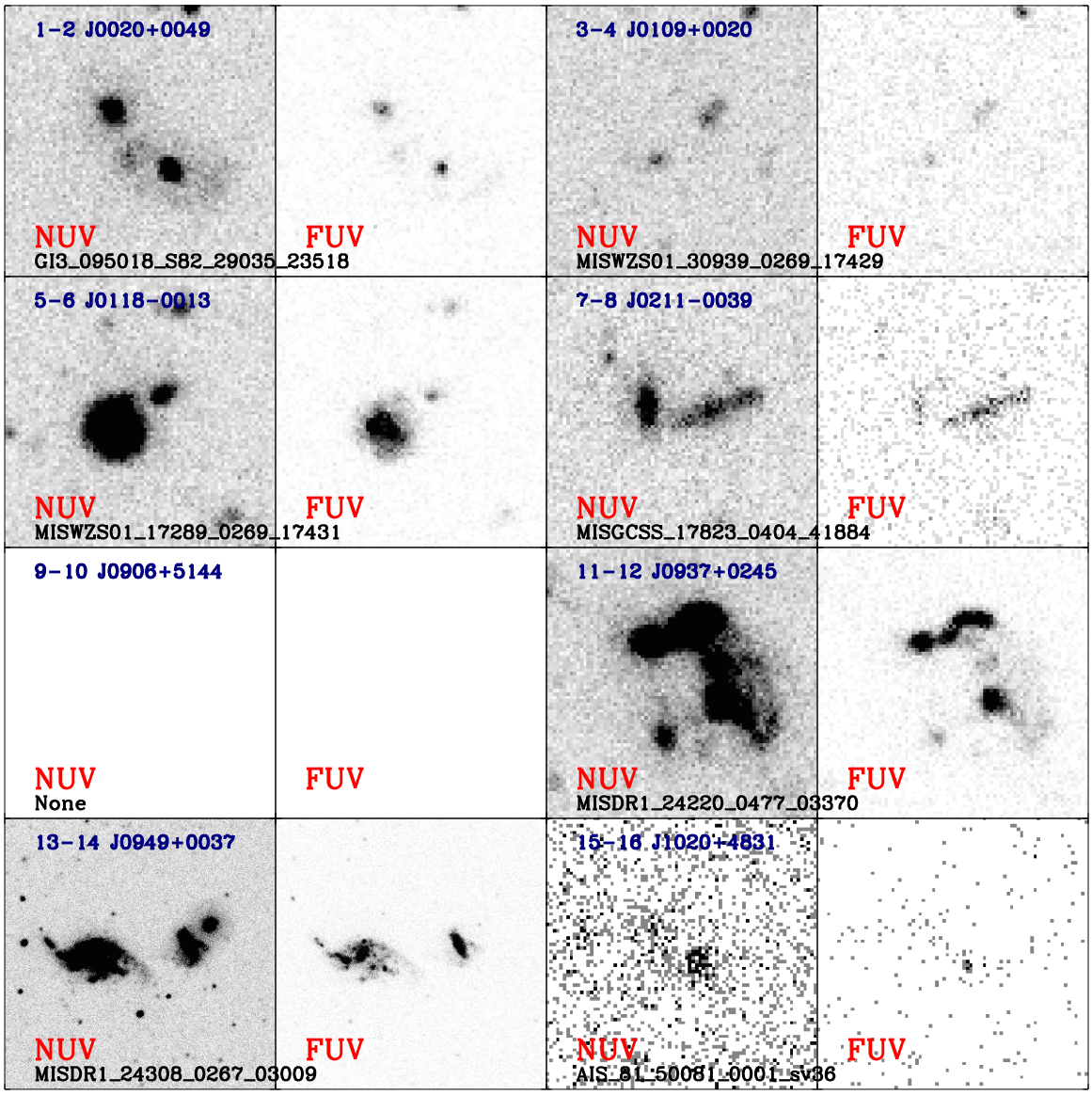

Figure 4.1 GALEX NUV and FUV images of paired galaxies. For pairs 13-14, 37-38 and 51-52, the scale of the images is $7.5' \times 7.5'$. For the other pairs, the scale of the images is $2' \times 2'$. The names of pairs are shown at the upper left of each image, and the names of the GALEX tiles are shown at the lower left.

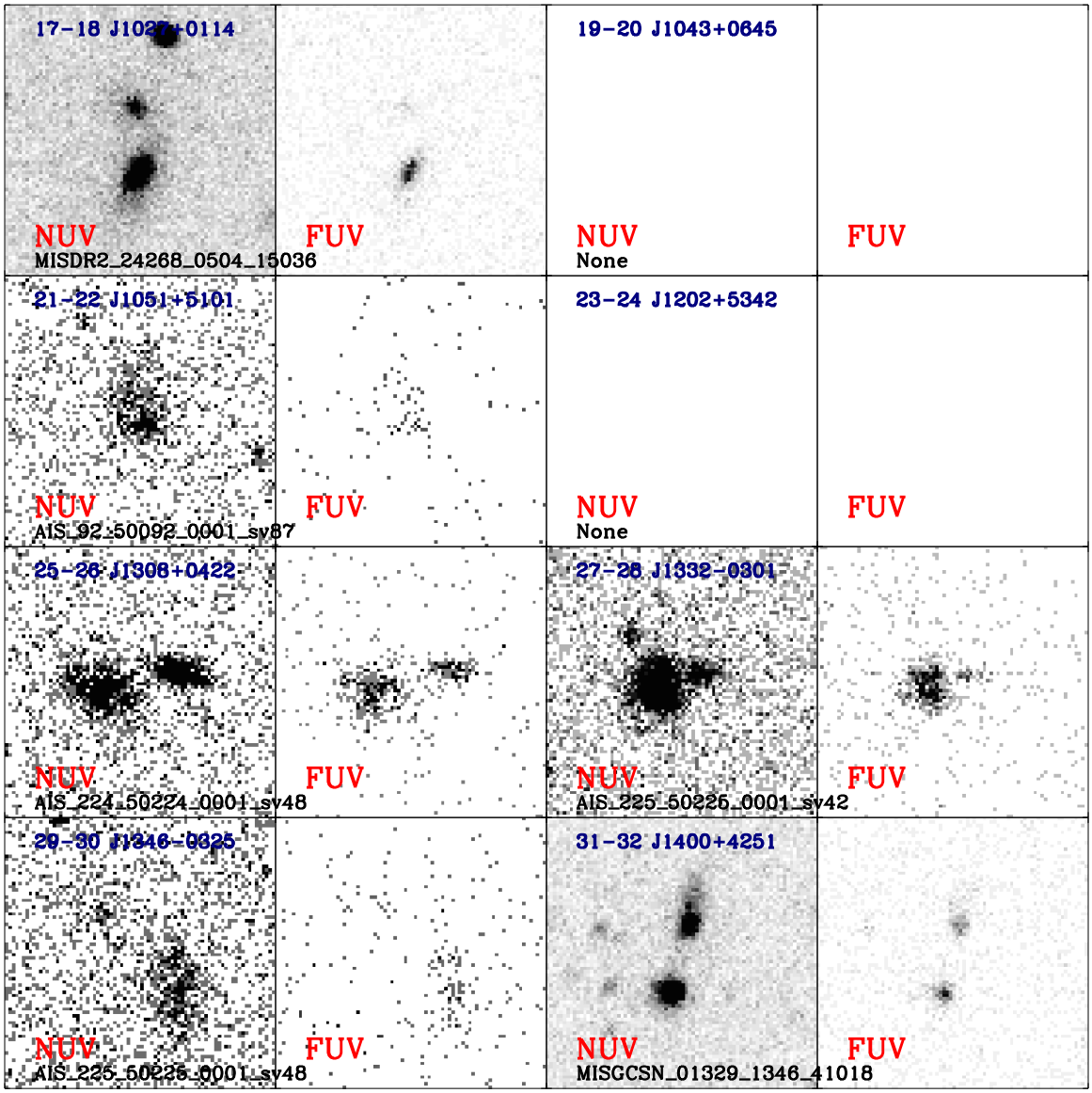

Figure 4.1 (Continued.)

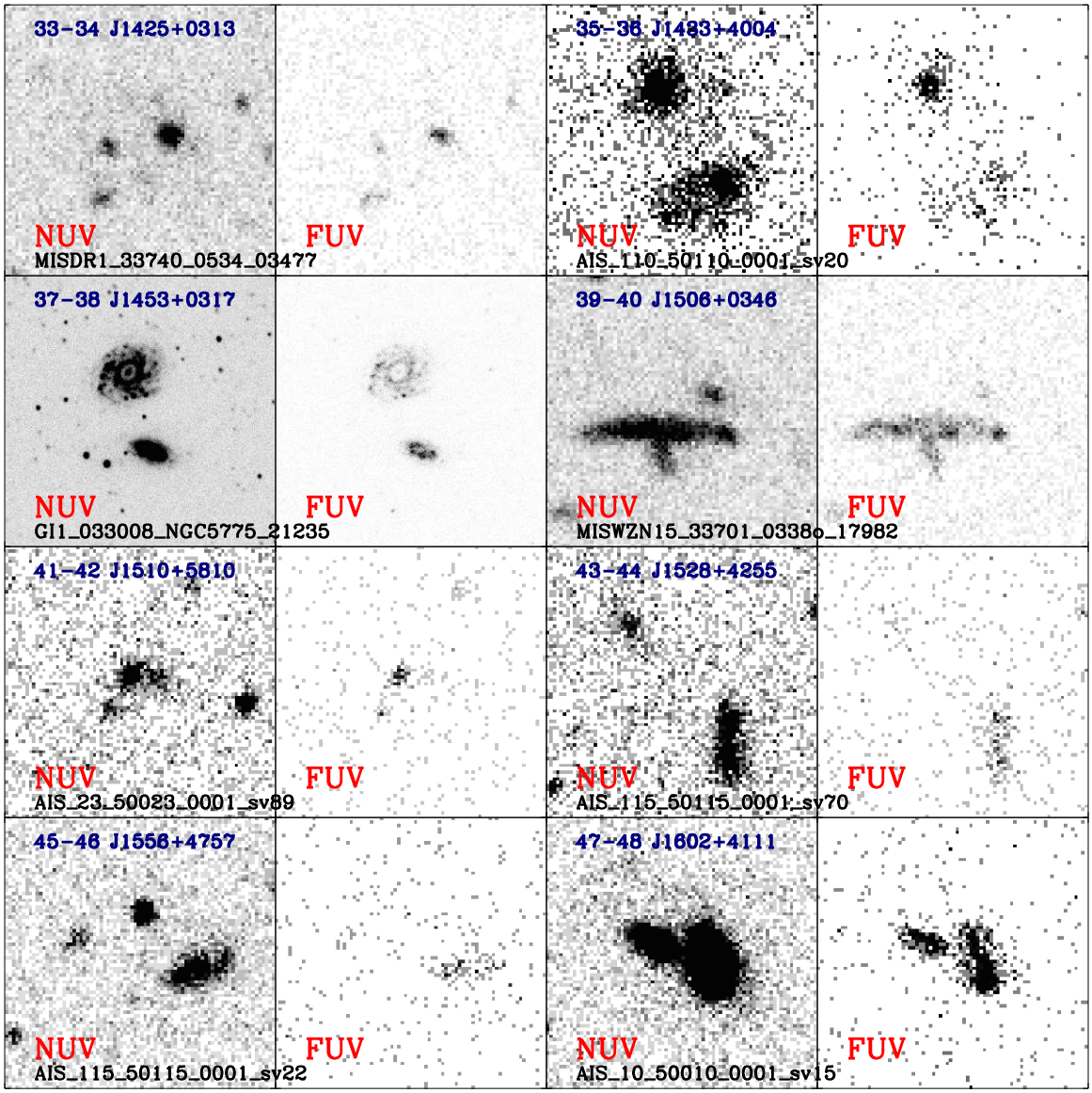

Figure 4.1 (Continued.)

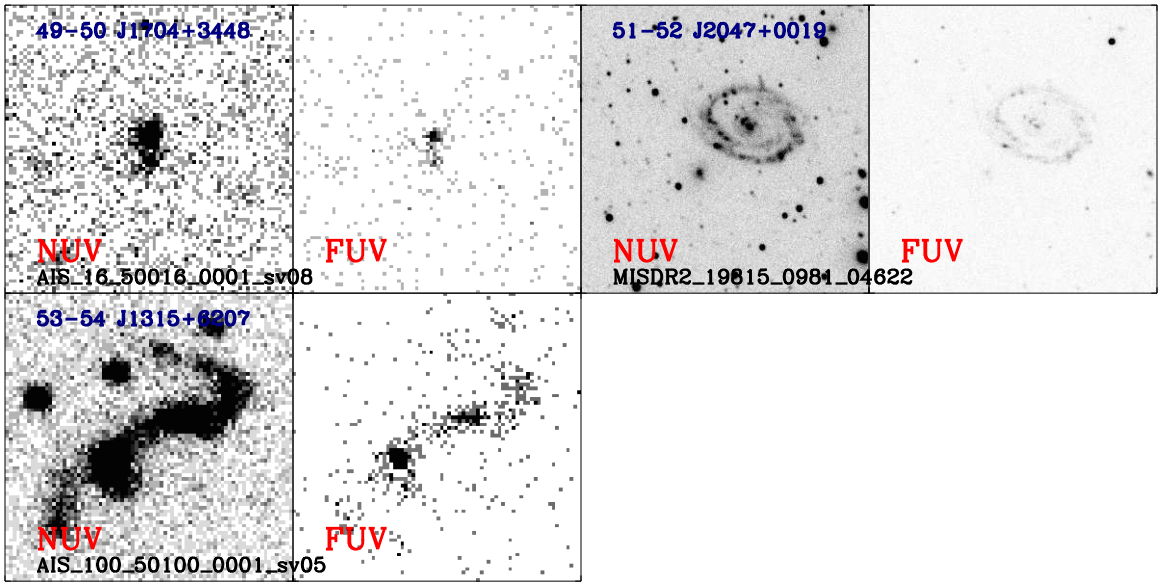

Figure 4.1 (Continued.)

Table 4.2. GALEX NUV and FUV fluxes for paired galaxies.

No.	Name.	NUV fluxes [μJy]			FUV fluxes [μJy]			Pho
		Total	4kpc	10kpc	Total	4kpc	10kpc	
(1)	(2)	(3)	(4)	(5)	(6)	(7)	(8)	(9)
1	J00202580+0049350	135.86±1.81	79.99±1.10	116.66±1.55	46.30±1.68	28.33±1.13	38.69±1.46	M
2	J00202748+0050009	62.39±1.18	45.85±0.88	82.32±1.47	31.26±1.26	25.74±1.08	38.63±1.48	M
3	J01093371+0020322	14.99±0.77	2.34±0.21	8.89±0.44	6.20±0.71	0.92±0.21	3.12±0.42	M
4	J01093517+0020132	9.42±0.73	2.43±0.22	6.74±0.42	3.16±0.62	1.04±0.23	2.62±0.40	M
5	J01183417-0013416	41.88±1.31	12.25±0.57	36.28±1.13	18.65±1.21	7.73±0.66	17.32±1.10	M
6	J01183556-0013594	643.75±3.50	24.73±0.63	167.72±1.63	423.20±4.60	15.01±0.84	108.57±2.27	M
7	J02110638-0039191	92.12±1.90	17.10±0.76	62.61±1.57	45.31±2.23	12.02±1.06	32.84±1.89	M
8	J02110832-0039171	92.94±1.93	35.69±1.06	83.52±1.82	10.63±1.44	5.37±0.77	10.84±1.34	M
9	J09060283+5144411	...	...	...	...	...	...	M
10	J09060498+5144071	...	...	...	...	...	...	M
11	J09374413+0245394	1604.41±5.75	15.92±0.59	120.81±1.58	990.88±9.45	8.05±0.87	65.12±2.44	M
12	J09374506+0244504	58.24±4.40	25.61±1.38	52.39±3.24	23.51±3.43	12.91±1.37	23.86±2.68	M
13	J09494143+0037163	3654.47±11.51	2484.03±8.70	3764.10±11.83	2406.68±14.94	1678.75±12.15	2432.11±15.06	M
14	J09495263+0037043	8222.12±16.51	1999.33±7.56	6423.39±13.79	6051.09±23.63	1388.66±10.92	4690.21±20.23	M
15	J10205188+4831096	46.47±5.72	3.31±1.08	17.78±2.48	26.10±5.95	4.35±2.03	11.00±3.27	M
16	J10205369+4831246	17.51±3.00	0.93±0.67	4.65±1.54	10.61±3.49	0.77±0.91	1.95±1.57	M
17	J10272950+0114490	196.57±2.94	68.00±1.40	148.24±2.22	82.45±3.10	34.35±1.71	67.14±2.51	M
18	J10272970+0115170	33.17±3.04	16.43±2.20	29.29±5.34	7.52±1.12	4.15±0.70	7.44±1.25	M
19	J10435053+0645466	...	...	...	...	...	...	M
20	J10435268+0645256	...	...	...	...	...	...	M
21	J10514368+5101195	159.89±9.03	30.16±3.38	82.13±5.83	58.98±9.58	15.68±4.26	35.80±6.68	M
22	J10514450+5101303	10.19±2.04	16.47±2.62	87.00±6.10	6.08±2.71	4.14±2.40	40.69±7.24	M
23	J12020424+5342317	...	...	...	...	...	...	M
24	J12020537+5342487	...	...	...	...	...	...	M
25	J13082737+0422125	220.22±9.96	53.73±4.56	177.91±8.53	147.73±13.59	38.83±6.72	120.69±12.01	M
26	J13082964+0422045	389.70±13.47	81.05±5.56	238.50±9.76	356.09±20.83	54.29±7.93	205.57±15.49	M
27	J13325525-0301347	16.53±2.16	13.77±1.97	51.32±3.90	13.46±3.27	11.05±2.97	23.42±4.44	M
28	J13325655-0301395	537.81±12.13	18.67±2.19	164.06±6.50	332.13±16.30	7.15±2.37	104.20±9.01	M
29	J13462001-0325407	163.96±10.50	12.73±2.81	84.38±7.15	104.15±13.43	9.25±3.87	56.96±9.59	M
30	J13462215-0325057	30.84±6.16	14.20±2.98	23.04±5.18	9.79±6.30	...	10.59±5.31	M
31	J14005782+4251207	71.52±1.74	15.36±0.61	44.64±1.10	38.37±2.46	9.21±0.97	26.23±1.70	M
32	J14005882+4250427	94.74±1.78	26.28±0.78	72.12±1.33	49.99±2.59	16.39±1.27	38.00±1.99	M
33	J14250552+0313590	62.01±1.68	15.34±0.67	49.48±1.30	28.97±1.85	9.27±0.89	25.22±1.55	M
34	J14250739+0313560	15.87±1.13	5.40±0.47	13.57±0.93	5.58±1.12	3.07±0.56	5.16±0.93	M
35	J14334683+4004512	387.57±13.72	15.51±2.46	98.20±6.17	219.93±17.53	7.97±3.09	46.35±7.47	M
36	J14334840+4005392	509.31±14.25	149.34±7.17	361.48±11.28	300.64±19.05	66.99±8.54	214.30±15.39	M
37	J14530282+0317451	1691.30±6.15	1021.81±3.68	1689.23±6.35	1039.03±8.30	626.87±6.09	1024.08±8.36	M

Table 4.2 (cont'd)

No.	Name.	NUV fluxes [μJy]			FUV fluxes [μJy]			Pho
		Total	4kpc	10kpc	Total	4kpc	10kpc	
(1)	(2)	(3)	(4)	(5)	(6)	(7)	(8)	(9)
38	J14530523+0319541	2562.27±6.82	436.93±2.36	2088.87±5.35	1667.60±11.10	220.25±3.77	1334.07±9.31	M
39	J15064391+0346364	2.17±0.45	7.16±0.60	21.26±1.21	0.81±0.44	2.68±0.61	5.21±1.08	M
40	J15064579+0346214	294.63±3.68	12.89±0.66	60.87±1.46	195.30±4.67	7.43±0.85	35.09±1.86	M
41	J15101587+5810425	6.46±1.25	8.11±1.55	33.97±3.55	1.93±1.08	2.84±1.32	8.93±2.53	A
42	J15101776+5810375	88.00±4.23	25.07±2.09	69.59±3.60	50.70±5.43	19.43±3.21	40.35±4.72	A
43	J15281276+4255474	261.10±8.47	61.55±3.70	199.60±6.99	105.60±9.32	18.70±3.60	73.22±7.36	M
44	J15281667+4256384	47.82±4.83	24.77±2.51	43.78±4.18	11.86±4.58	7.11±2.42	14.53±4.24	M
45	J15562191+4757172	155.66±4.45	38.89±1.95	121.53±3.62	77.24±9.38	21.54±4.44	67.72±8.15	M
46	J15562738+4757302	< 1.45	...	...	< 0.91	...	...	M
47	J16024254+4111499	932.13±10.04	91.58±3.11	376.17±6.33	607.65±22.66	66.52±7.42	253.73±14.54	M
48	J16024475+4111589	345.27±6.38	55.92±2.48	231.41±5.15	197.24±13.01	39.18±5.71	138.59±10.85	M
49	J17045089+3448530	14.98±2.02	1.59±0.73	30.36±2.86	8.81±2.65	2.72±1.47	13.36±3.29	A
50	J17045097+3449020	141.08±6.07	23.12±2.37	89.97±4.71	54.15±6.57	9.34±2.66	41.64±5.64	A
51	J20471908+0019150	2906.97±15.56	20.55±1.18	165.51±3.01	1644.18±14.13	11.75±1.10	71.46±2.72	A
52	J20472428+0018030	114.65±3.03	66.15±1.94	124.30±4.51	31.58±2.28	18.95±1.34	35.59±2.61	M
53	J13153076+6207447	329.93±6.00	30.69±1.86	171.58±4.47	191.07±15.65	12.72±4.05	89.59±10.73	A
54	J13153506+6207287	736.30±9.99	130.55±3.65	367.29±6.24	399.30±23.76	80.85±9.95	198.45±15.68	A

Note. — Description of columns: 1. Number of galaxies in the pair sample; 2. Galaxy ID in the pair sample; 3. Total NUV fluxes; 4. NUV fluxes in 4 kpc aperture; 5. NUV fluxes in 10 kpc aperture; 6. Total FUV fluxes; 7. FUV fluxes in 4kpc aperture; 8. FUV fluxes in 10 kpc aperture; 9. Photometry method: 'M' for manual photometry; 'A' for aperture photometry.

Table 4.3. GALEX NUV and FUV fluxes for control galaxies.

No.	ID	NUV fluxes (μJy)			FUV fluxes (μJy)			Pair galaxy ID
		Total	4kpc	10kpc	Total	4kpc	10kpc	
(1)	(2)	(3)	(4)	(5)	(6)	(7)	(8)	(9)
1	LCK-287434	26.69±0.59	4.28±0.13	13.71±0.28	13.47±0.52	2.16±0.14	6.46±0.27	J00202580+0049350
2	LCK-178064	32.52±0.48	3.06±0.09	14.58±0.21	17.06±0.44	1.53±0.10	7.89±0.24	J00202748+0050009
3	LCK-320371	89.64±4.18	8.12±0.47	39.81±1.22	64.74±0.74	6.07±0.20	28.30±0.43	J01093371+0020322
4	LCK-523686	20.38±0.41	2.67±0.07	8.70±0.14	6.34±0.39	0.78±0.08	2.52±0.16	J01093517+0020132
5	LCK-415950	1147.61±1.29	71.78±0.30	279.07±0.59	671.83±2.25	39.00±0.53	141.13±1.00	J01183417-0013416
6	LCK-086596	130.89±0.49	4.14±0.07	19.25±0.15	97.10±0.72	2.87±0.12	13.71±0.26	J01183556-0013594
7	EN1-158103	423.57±1.20	48.20±0.37	183.86±0.74	298.52±2.32	30.50±0.72	116.71±1.41	J02110638-0039191
8	EN1-360222	85.84±0.59	6.52±0.13	37.18±0.31	44.99±1.31	4.59±0.35	23.99±0.82	J02110832-0039171
9	EN1-010947	8.43±0.26	2.15±0.08	7.41±0.19	2.25±0.32	0.69±0.14	1.99±0.28	J09060283+5144411
10	LCK-162208	199.59±0.83	36.47±0.29	136.22±0.59	98.87±0.86	18.38±0.35	73.85±0.71	J09060498+5144071
11	EN1-018834	10.43±0.51	1.60±0.07	4.71±0.13	3.94±0.59	1.10±0.15	2.64±0.24	J09374413+0245394
12	LCK-233199	62.65±0.75	13.15±0.23	45.42±0.47	40.17±0.81	9.67±0.33	29.63±0.60	J09374506+0244504
13	LCK-019297	15.80±0.65	2.61±0.10	10.31±0.24	5.99±0.51	1.22±0.11	4.11±0.23	J09494143+0037163
14	LCK-703238	52.11±0.58	3.39±0.07	18.96±0.19	35.53±0.63	2.61±0.14	13.48±0.32	J09495263+0037043
15	LCK-050667	39.92±0.64	3.62±0.13	18.22±0.30	22.90±0.65	1.94±0.15	10.86±0.37	J10205188+4831096
16	LCK-027930	59.00±0.60	5.04±0.08	25.83±0.20	29.76±0.64	2.71±0.14	14.10±0.33	J10205369+4831246
17	LCK-071868	297.51±0.48	26.51±0.11	132.75±0.26	185.34±0.92	16.75±0.26	84.19±0.59	J10272950+0114490
18	EN1-516050	...	...	...	...	...	...	J10272970+0115170
19	LCK-641925	461.08±0.99	13.38±0.14	92.53±0.37	301.58±1.51	7.52±0.23	53.62±0.60	J10435053+0645466
20	LCK-400414	105.03±0.85	11.42±0.09	38.10±0.19	69.68±0.96	5.80±0.16	22.01±0.33	J10435268+0645256
21	LCK-534543	306.47±0.93	11.40±0.14	56.46±0.32	199.36±1.31	6.20±0.22	32.88±0.50	J10514368+5101195
22	LCK-136060	26.52±0.87	2.21±0.12	12.18±0.31	14.59±0.63	1.09±0.11	7.37±0.29	J10514450+5101303
23	LCK-172179	36.33±0.51	1.93±0.06	11.58±0.17	18.48±0.52	1.16±0.10	6.76±0.24	J12020424+5342317
24	LCK-564807	132.62±0.54	5.93±0.08	39.19±0.21	94.23±0.86	3.88±0.16	25.67±0.41	J12020537+5342487

Table 4.3 (cont'd)

No.	ID	NUV fluxes (μJy)			FUV fluxes (μJy)			Pair galaxy ID
		Total	4kpc	10kpc	Total	4kpc	10kpc	
(1)	(2)	(3)	(4)	(5)	(6)	(7)	(8)	(9)
25	LCK-621286	15.13±0.44	2.80±0.08	9.63±0.18	5.74±0.37	1.27±0.10	4.14±0.19	J13082737+0422125
26	LCK-038716	96.19±0.66	6.35±0.14	31.60±0.31	65.93±0.77	4.17±0.18	22.14±0.42	J13082964+0422045
27	LCK-582705	23.95±0.37	6.74±0.10	18.54±0.19	7.45±0.39	2.66±0.14	6.30±0.24	J13325525-0301347
28	LCK-329416	35.87±0.48	3.67±0.08	19.44±0.20	17.83±0.53	1.93±0.12	9.67±0.28	J13325655-0301395
29	LCK-040350	2.47±0.24	0.48±0.08	1.93±0.18	0.69±0.20	0.16±0.06	0.41±0.14	J13462001-0325407
30	EN1-346329	80.04±0.66	5.25±0.13	27.97±0.29	49.61±1.09	3.25±0.24	18.06±0.56	J13462215-0325057
31	LCK-182514	50.07±0.62	1.99±0.07	9.22±0.16	32.31±0.61	1.39±0.10	5.89±0.20	J14005782+4251207
32	LCK-515902	9.38±0.44	0.53±0.04	2.99±0.09	3.16±0.37	0.26±0.05	1.14±0.11	J14005882+4250427
33	LCK-347435	8.74±0.35	0.88±0.05	3.32±0.11	2.50±0.39	0.36±0.07	1.05±0.13	J14250552+0313590
34	LCK-048281	32.83±0.48	1.33±0.06	6.70±0.13	18.38±0.48	0.53±0.06	2.97±0.15	J14250739+0313560
35	NGC0024	11029.62±19.40	6024.89±12.83	10153.03±18.43	8081.00±26.50	4344.08±18.78	7450.55±25.41	J14334683+4004512
36	NGC2403	317739.62±76.09	234299.82±60.46	326425.75±84.24	234466.58±105.82	166958.51±87.71	241057.21±111.09	J14334840+4005392
37	NGC0925	65670.66±62.90	12313.23±22.70	38203.55±41.90	48593.78±84.14	8666.34±32.27	27602.99±59.02	J14530282+0317451
38	NGC3049	4639.48±9.40	2575.06±6.29	4168.10±8.61	2872.98±17.44	1506.02±12.19	2509.49±16.10	J14530523+0319541
39	NGC3184	47886.38±153.04	5218.17±45.98	30169.53±110.95	34313.52±212.38	3101.25±61.80	20133.21±157.35	J15064391+0346364

Note. — Description of columns: 1. Number of galaxies in the control sample; 2. Galaxy ID in the control sample; 3. Total NUV fluxes; 4. NUV fluxes in 4 kpc aperture; 5. NUV fluxes in 10 kpc aperture; 6. Total FUV fluxes; 7. FUV fluxes in 4kpc aperture; 8. FUV fluxes in 10 kpc aperture; 9. ID of the matched paired galaxies.

We simulate the contamination from one component to the other using stacked light profile of our S and E galaxies. For round-shaped galaxies, we calculate the fluxes of one galaxy with companion galaxy (measured flux, f_m) and without companion galaxy (true flux, f_t) in fixed apertures. The value of $(f_m - f_t)/f_m$ are shown in Figure 4.2. We find for most of our galaxies, the contamination is less than 5%. For the pairs J0211-0039, the contamination is less than 10%. For the pairs J1510+5810 and J1704+3448, the contamination may reach 20%. On average, the contamination brings little error (< 0.025 dex) to our result and does not affect our conclusion.

In order to prove the consistency between these methods, we compared the results of the different methods with GALEX pipeline data (Figure 4.3). For paired galaxies, it can be seen that the results of manual photometry and aperture photometry are consistent with each other for sources well separated from their companion galaxies. Also, the results of both manual and aperture photometry are consistent with pipeline data when the sources are not too close to their companion galaxies and are not very extended. The GALEX pipeline photometry is not preferred because the automatic source extraction may identify extended sources as separate sources (referred to as *shredding* in Takeuchi et al. 2010) or mistake a close pair as a single source, and therefore it is less accurate.

4.2.4 Nuclear fluxes

We also measure fluxes within different circular apertures of each galaxy in order to examine the fraction of the integrated emission contributed by the nuclear and near-nuclear regions. For infrared bands, IRAC fluxes within 4 kpc and 10 kpc apertures are already given by Xu10 for paired galaxies, so we only need to measure MIPS fluxes and the same apertures for the control galaxies using SWIRE and SINGS images. For UV bands, the fluxes within the same apertures are measured, with the goal of comparing the fraction of the nuclear contribution with the IR part. Tables 4.2 and 4.3 give the results for paired and control galaxies, respectively. Notice that the resolutions of GALEX images in the FUV and NUV bands are $\sim 4.3''$ and $\sim 5.3''$, while the resolutions of Spitzer images in the 8 and 24 μm bands are $\sim 2''$ and

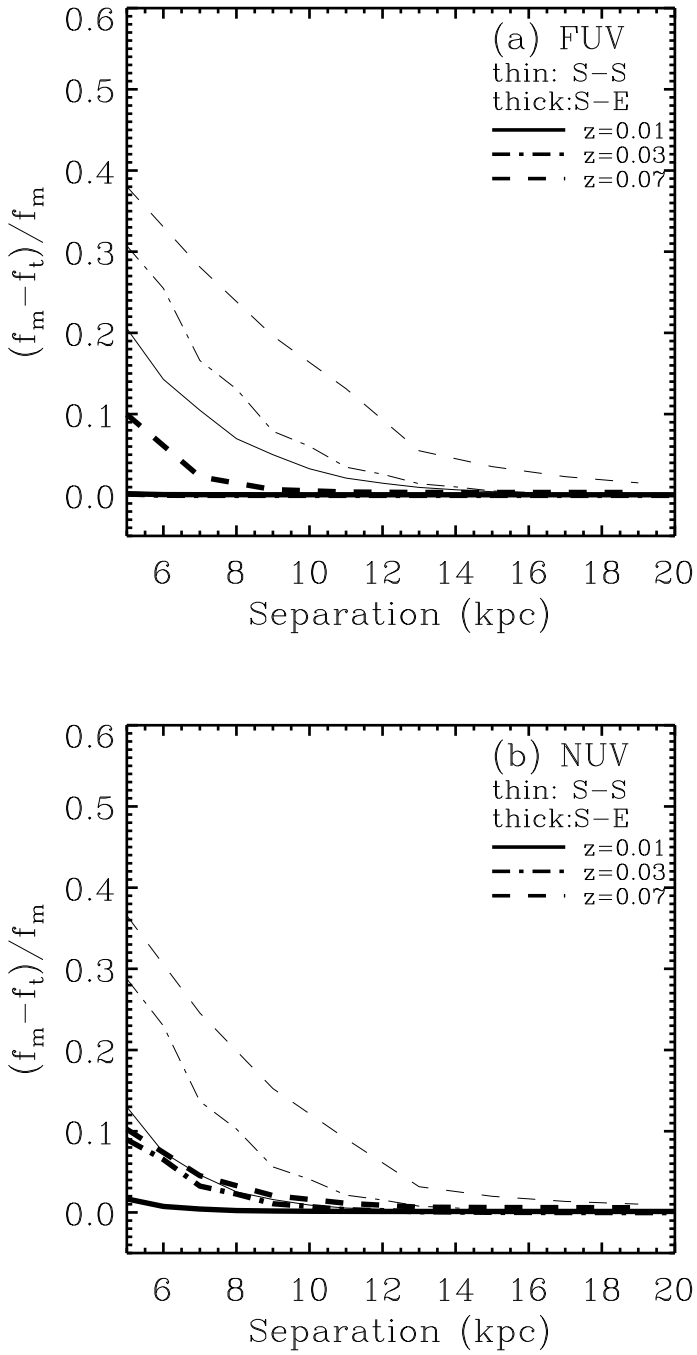

Figure 4.2 Contamination from one component to the other. The simulation uses profile of stacked S and E galaxies in our pair sample. Results for S-S (thin lines) and S-E (thick lines) pairs at $z = 0.01$ (solid), $z = 0.03$ (dash dot), $z = 0.07$ (dashed) are plotted.

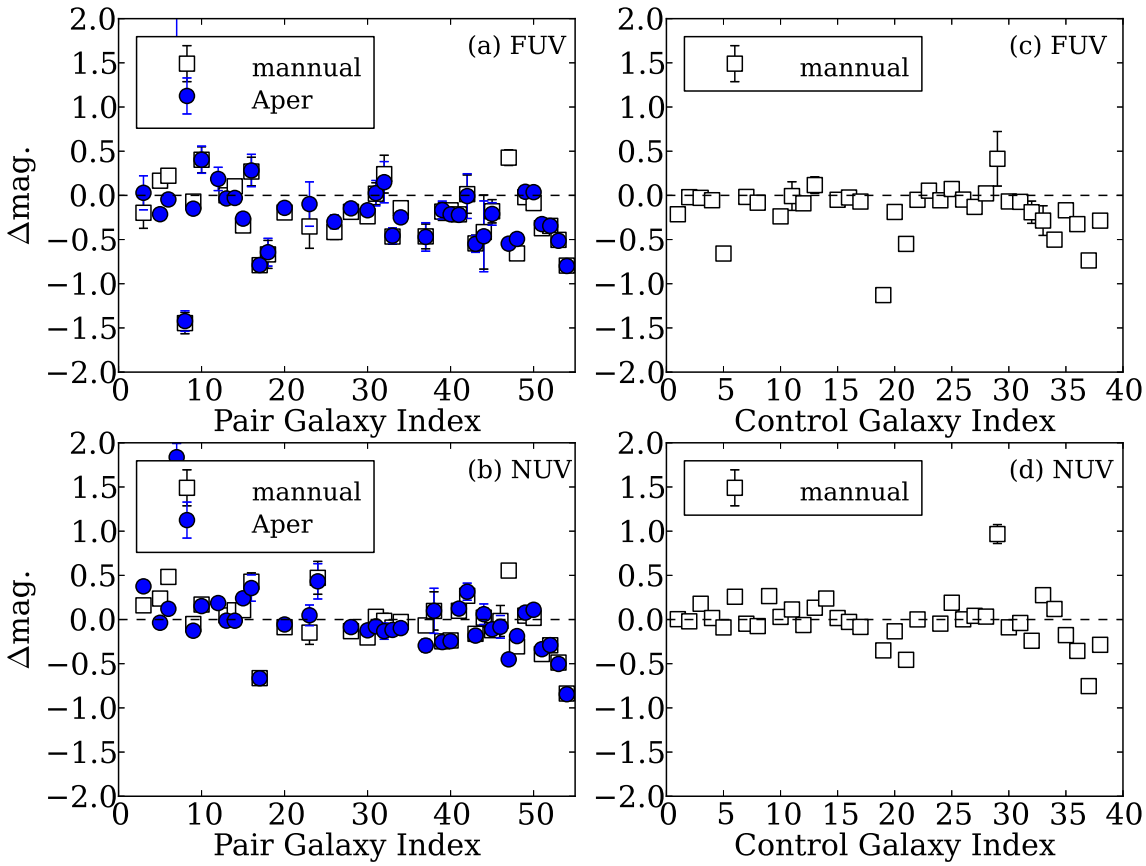

Figure 4.3 Comparison between different methods of photometry. Panels (a) and (b) are for paired galaxies. Panels (c) and (d) are for control galaxies. Squares indicate the magnitude difference between manual measurements and GALEX pipeline data, and dots show the difference between aperture measurements and GALEX pipeline data.

$\sim 6''$. For our galaxies, the 4 kpc central region is about $7''$ in size, and therefore the central regions of most of our galaxies can be resolved. For a few galaxies with small angular size, the difference in image resolutions may cause some uncertainties. However, it can be seen that the resolutions of GALEX and Spitzer MIPS are very similar. Although IRAC 8 μm has a higher resolution, the weight of 8 μm fluxes is very small when calculating the IR luminosity (Equation (4.1)). Therefore, the bias caused by the difference in resolutions can be ignored.

4.3 Dust Attenuation

As mentioned in Section 4.1, dust attenuation in paired galaxies may be very complex and is usually studied using numerical simulations. Here with both UV and IR data, we can examine whether there is a statistical difference in dust attenuation between paired and isolated galaxies. The attenuation in the FUV band, $A_{\rm FUV}$, of these galaxies can be calculated using the formula given in Buat et al. (2011):

$$\begin{aligned} A_{\rm FUV}[{\rm mag}] &= 0.483 + 0.812\ y + 0.373\ y^2 + 0.299\ y^3 \\ &\quad -0.106\ y^4, \end{aligned} \tag{4.2}$$

where $y = \log(L_{\rm IR}/L_{\rm FUV})$. $L_{\rm IR}$ is defined in Equation (4.1). $L_{\rm FUV}$ is νL_ν at the FUV band (1530 Å).

The results for the 39 non-AGN spirals[1] and the control sample are presented in Table 4.4. There are several different attenuation measurements in the literature. Although these measurements depend on star formation history, it has been shown that they deviate little from each other: Buat et al. (2011) compared their results with Meurer et al. (1999) and Buat et al. (2005), and show that the difference between them is at most 0.3 magnitude. The difference between their results and those of Cortese et al. (2008) is small for low dust attenuation, but can reach 0.7 mag for high attenuations. Boquien et al. (2012) also used a fourth order polynomial to fit the relation, and they show that the difference between their work and others (Burgarella

[1]Hereafter, we omit the term 'non-AGN' since in the following analyses we deal only with non-AGN galaxies.

et al. 2006; Cortese et al. 2008; Buat et al. 2011; Hao et al. 2011) is smaller than 0.2 magnitude. In order to assure that using different formulae does not affect our conclusion, we also use Buat et al. (2005) and Cortese et al. (2008) to calculate the dust attenuation, and find our conclusion unchanged.

Table 4.4. SFR, SSFR and $A_{\rm FUV}$ for non-AGN spirals in the pair and control samples.

ID	$\rm SFR_{TOT}$	$\rm logSFR_{FUV}$	$\rm logSFR_{IR}$	$\rm logSSFR_{TOT}$	$\frac{\rm SFR_{FUV}}{\rm SFR_{TOT}}$	$A_{\rm FUV}$	Pair Galaxy ID	$\rm SFR_{TOT}$	$\rm logSFR_{FUV}$	$\rm logSFR_{IR}$	$\rm logSSFR_{TOT}$	$\frac{\rm SFR_{FUV}}{\rm SFR_{TOT}}$	$A_{\rm FUV}$
	$(M_\odot \rm yr^{-1})$	$(M_\odot \rm yr^{-1})$	$(M_\odot \rm yr^{-1})$	$(\rm yr^{-1})$		(mag)		$(M_\odot \rm yr^{-1})$	$(M_\odot \rm yr^{-1})$	$(M_\odot \rm yr^{-1})$	$(\rm yr^{-1})$		(mag)
(1)	(2)	(3)	(4)	(5)	(6)	(7)	(8)	(9)	(10)	(11)	(12)	(13)	(14)
LCK-287434	-0.06	-1.36	0.07	-10.94	5.0%	3.47	J00202580+0049350	0.13	-1.39	0.27	-10.71	3.1%	4.06
LCK-178064	-0.16	-0.95	-0.08	-11.31	16.1%	2.12	J01093517+0020132	-0.91	-1.70	-0.83	-11.96	16.3%	2.10
LCK-320371	0.18	-0.33	0.18	-10.78	30.5%	1.42	J01183556-0013594	0.94	0.49	0.90	-9.99	35.8%	1.24
LCK-523686	-0.53	-1.38	-0.44	-11.47	14.1%	2.27	J02110832-0039171	-0.76	-1.88	-0.64	-11.74	7.7%	2.98
LCK-415950	0.87	0.33	0.88	-10.50	28.7%	1.48	J09374413+0245394	0.90	0.23	0.95	-10.56	21.2%	1.81
LCK-086596	0.11	-0.16	-0.07	-10.75	53.8%	0.81	J10205188+4831096	0.53	-0.62	0.65	-10.35	7.1%	3.07
EN1-158103	0.47	-0.08	0.48	-10.23	28.4%	1.49	J10272950+0114490	0.43	-0.89	0.56	-10.30	4.8%	3.52
EN1-360222	0.52	-0.57	0.64	-10.22	8.0%	2.92	J10435053+0645466	...	...	1.02	...	...	...
EN1-010947	-1.32	-2.01	-1.26	-11.99	20.1%	1.87	J10435268+0645256	...	...	0.06	...	...	...
LCK-162208	0.56	-0.75	0.69	-10.56	4.9%	3.50	J10514450+5101303	-0.97	-1.97	-0.86	-12.10	10.0%	2.66
EN1-018834	-0.03	-1.28	0.10	-11.09	5.6%	3.36	J12020424+5342317	...	...	0.41	...	...	...
LCK-233199	-0.15	-1.04	-0.05	-10.75	12.8%	2.38	J13082964+0422045	0.02	-0.19	-0.24	-10.51	61.8%	0.66
LCK-019297	0.92	-1.37	1.07	-10.04	0.5%	5.64	J13325525-0301347	0.72	-1.00	0.87	-10.18	1.9%	4.60
LCK-703238	-0.04	-0.65	-0.01	-11.24	24.8%	1.64	J13325655-0301395	0.80	0.37	0.75	-10.41	37.3%	1.20
LCK-050667	-0.23	-0.81	-0.21	-11.15	26.4%	1.57	J13462001-0325407	-0.04	-0.76	0.02	-11.05	19.2%	1.92
LCK-027930	0.50	-0.70	0.63	-10.56	6.3%	3.20	J14005782+4251207	0.88	-0.90	1.03	-10.13	1.7%	4.72
LCK-071868	0.84	0.11	0.90	-10.10	19.0%	1.93	J14005882+4250427	1.05	-0.76	1.20	-9.85	1.5%	4.80
EN1-516050	...	...	0.28	...	...	...	J14250739+0313560	-0.86	-1.64	-0.79	-11.52	16.9%	2.06
LCK-641925	-0.09	-0.15	-0.78	-11.28	85.8%	0.21	J14334683+4004512	0.68	-0.35	0.79	-10.57	9.5%	2.73
LCK-400414	-0.05	-0.76	0.01	-11.17	19.5%	1.90	J14334840+4005392	0.90	-0.20	1.02	-10.20	8.0%	2.93
LCK-534543	0.57	-0.21	0.65	-10.57	16.6%	2.08	J15064391+0346364	-0.47	-2.50	-0.32	-11.69	0.9%	5.26
LCK-136060	-0.23	-0.96	-0.16	-11.31	18.6%	1.96	J15064579+0346214	0.71	-0.15	0.80	-10.46	13.9%	2.28
LCK-172179	-0.18	-0.90	-0.12	-11.20	19.3%	1.91	J15101587+5810425	-0.43	-2.24	-0.28	-11.45	1.5%	4.81
LCK-564807	0.30	-0.22	0.30	-10.46	30.2%	1.43	J15101776+5810375	0.39	-0.79	0.52	-10.40	6.6%	3.16

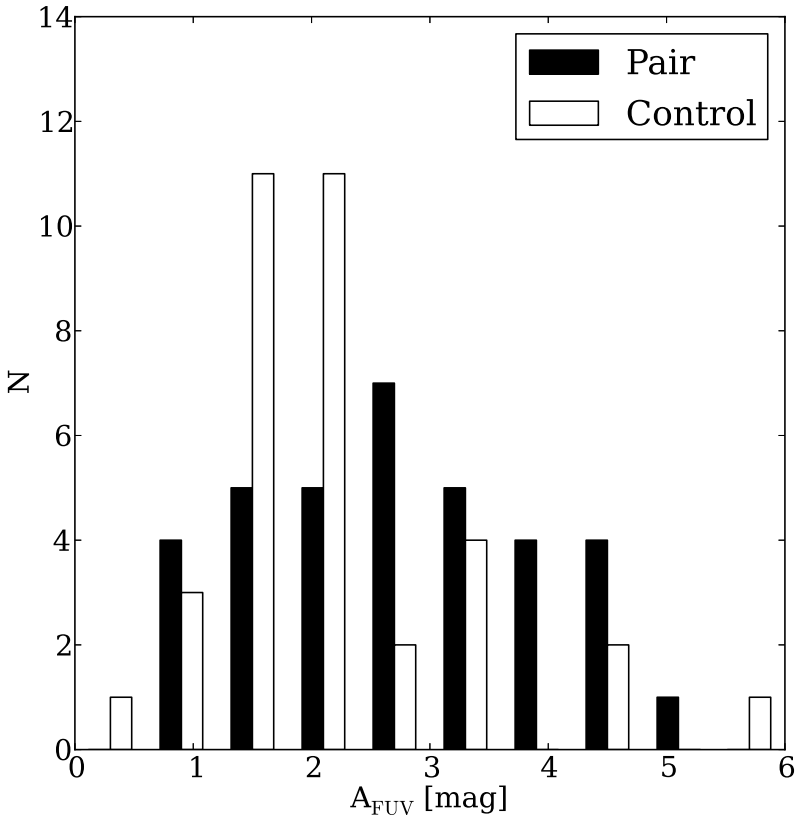

Figure 4.4 Histograms of $A_{\rm FUV}$ distributions for spirals in the pair and control samples.

Figure 4.4 plots the histogram of the distribution of dust attenuation in our pair and control samples. It can be seen that $A_{\rm FUV}$ in paired galaxies has a quite different distribution from that in the control sample. Quantitatively, the mean $A_{\rm FUV}$ is 2.82 ± 0.24 mag for spirals in paired galaxies, whereas it is only 2.20 ± 0.21 mag for the control galaxies. The Kolmogorov-Smirnov (KS) test shows that the possibility that the two distributions are the same is only 0.024. Therefore, the dust attenuation in paired galaxies is not the same as in isolated galaxies. The effect of this difference to computing SSFRs will be discussed in Section 4.4. We now analyze the dependence of dust attenuation on different physical properties for our pair and control samples.

Table 4.4 (cont'd)

ID	SFR_{TOT}	$logSFR_{FUV}$	$logSFR_{IR}$	$logSSFR_{TOT}$	$\frac{SFR_{FUV}}{SFR_{TOT}}$	A_{FUV}	Pair Galaxy ID	SFR_{TOT}	$logSFR_{FUV}$	$logSFR_{IR}$	$logSSFR_{TOT}$	$\frac{SFR_{FUV}}{SFR_{TOT}}$	A_{FUV}
	$(M_\odot yr^{-1})$	$(M_\odot yr^{-1})$	$(M_\odot yr^{-1})$	(yr^{-1})		(mag)		$(M_\odot yr^{-1})$	$(M_\odot yr^{-1})$	$(M_\odot yr^{-1})$	(yr^{-1})		(mag)
(1)	(2)	(3)	(4)	(5)	(6)	(7)	(8)	(9)	(10)	(11)	(12)	(13)	(14)
LCK-621286	-0.45	-1.42	-0.35	-11.77	10.9%	2.57	J15281276+4255474	0.50	-0.94	0.64	-10.76	3.6%	3.87
LCK-038716	0.18	-0.33	0.18	-10.82	30.7%	1.41	J15281667+4256384	-0.67	-1.93	-0.54	-11.70	5.5%	3.38
LCK-582705	-0.91	-1.72	-0.83	-11.40	15.6%	2.15	J15562191+4757172	0.13	-1.06	0.26	-10.36	6.5%	3.18
LCK-329416	0.25	-0.89	0.37	-10.82	7.3%	3.04	J16024254+4111499	1.11	0.33	1.19	-10.00	16.6%	2.09
LCK-040350	-0.34	-2.33	-0.19	-11.04	1.0%	5.17	J16024475+4111589	0.55	-0.16	0.61	-10.23	19.4%	1.91
EN1-346329	0.43	-0.18	0.46	-10.54	24.8%	1.64	J17045089+3448530	0.88	-1.02	1.03	-10.13	1.2%	5.00
LCK-182514	0.55	-0.31	0.64	-10.66	13.8%	2.30	J17045097+3449020	1.44	-0.25	1.59	-9.84	2.0%	4.51
LCK-515902	0.19	-1.26	0.33	-11.18	3.6%	3.88	J20471908+0019150	0.49	-0.00	0.47	-10.88	32.6%	1.35
LCK-347435	0.18	-1.75	0.33	-10.69	1.2%	5.06	J13153076+6207447	1.10	-0.25	1.24	-9.81	4.4%	3.62
LCK-048281	-0.20	-0.86	-0.15	-11.25	21.8%	1.78	J13153506+6207287	1.73	0.07	1.88	-9.36	2.2%	4.44
NGC0024	-0.84	-1.05	-1.09	-10.47	60.8%	0.68	J09494143+0037163	-0.32	-0.55	-0.54	-10.03	58.3%	0.72
NGC2403	-0.30	-0.95	-0.26	-10.29	22.7%	1.73	J09495263+0037043	0.09	-0.12	-0.16	-9.86	60.9%	0.68
NGC0925	-0.04	-0.32	-0.21	-10.10	52.5%	0.84	J13082737+0422125	-0.20	-0.58	-0.29	-10.35	42.5%	1.06
NGC3049	-0.11	-0.66	-0.10	-10.02	28.2%	1.50	J14530282+0317451	-0.63	-1.06	-0.67	-10.55	36.8%	1.22
NGC3184	0.04	-0.38	-0.02	-10.27	38.3%	1.17	J14530523+0319541	-0.43	-0.86	-0.48	-10.60	37.5%	1.19

Note. — Description of columns: 1. Galaxy ID in the control sample; 2. Logarithm of SFR_{TOT} derived from Equation 4.10; 3. Logarithm of SFR_{FUV} derived from Equation (4.7); 4. Logarithm of SFR_{IR} derived from Equation (4.8); 5. Logarithm of $SSFR_{TOT}$; 6. The ratio of SFR_{FUV} to SFR_{TOT}; 7. The attenuation at the FUV band; 8. Galaxy ID in the pair sample; Columns 9-14. the same as 2-7, but for paired galaxies.

Table 4.5. Average $A_{\rm FUV}$ for paired and control galaxies in four different mass bins.

Mass bins	$A_{\rm FUV}$ (mag)			
	pair	control	S in S-S	S in S-E
$9.7 < \log(M/M_\odot) < 10.2$	0.97±0.12	1.18±0.20	0.97±0.12	...
$10.2 < \log(M/M_\odot) < 10.8$	2.48±0.53	2.52±0.69	1.91±0.72	3.35±0.17
$10.8 < \log(M/M_\odot) < 11.2$	3.37±0.28	2.48±0.30	3.61±0.34	2.76±0.38
$11.2 < \log(M/M_\odot) < 11.6$	2.96±0.61	2.02±0.42	3.51±0.71	1.58±0.23

4.3.1 Dependence of Dust Attenuation on Mass

First we examine the dependence of $A_{\rm FUV}$ on the stellar mass of galaxies. The stellar mass is calculated using the 2MASS K_s-band luminosities (Xu10). We divide the samples into four mass bins using the same bins as Xu10 (see also Section 4.4). The average $A_{\rm FUV}$ in each mass bin is given in Table 4.5 and shown in Figure 4.5. It can be observed in the figure that the general trend for dust attenuation is that it increases as the stellar mass of a galaxy increases until the stellar mass reaches $\sim 10^{11} M_\odot$ for paired galaxies and $\sim 10^{10.5} M_\odot$ for isolated galaxies. This correlation between dust attenuation and mass may be due to the correlation between metallicity and dust content (Brinchmann et al. 2004). However, in the more massive bins, dust attenuation seems to decrease.

We compare this trend with previous studies. Kauffmann et al. (2003) investigated a sample selected with the SDSS z' band and found that dust attenuation reaches a maximum at a stellar mass of $10^{10.5} M_\odot$ and then decreases as the stellar mass increases. They concluded that when the stellar mass is larger than $10^{10.5} M_\odot$, the number of galaxies with old stellar populations rapidly increase, implying less massive galaxies contain more gas and young stars. A similar trend is found for our K-band selected control galaxies. The mass turn-off of paired galaxies appears higher than

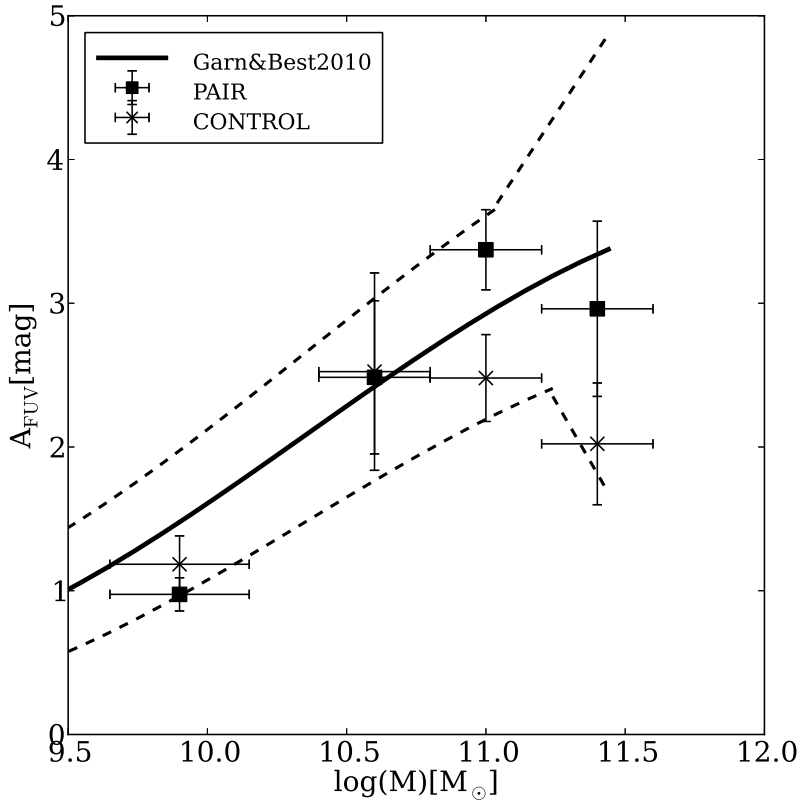

Figure 4.5 Dependence of $A_{\rm FUV}$ on galaxy stellar mass for spirals in pairs (squares) and for their control galaxies (crosses). The solid line indicates the result given by Garn & Best (2010) (corrected from $H_0 = 70\ \mathrm{km\,s^{-1}\,Mpc^{-1}}$ to $H_0 = 75\ \mathrm{km\,s^{-1}\,Mpc^{-1}}$), and the dashed lines show the 1σ uncertainty.

in control galaxies, implying that merging processes increase the dust attenuation in galaxies. However, the trend here can be due to the selection effect as well. Iglesias-Páramo et al. (2006) found that dust attenuation is larger for higher stellar mass galaxies in UV selected samples whereas it is lower for higher stellar mass galaxies in IR selected samples. The trend we find for control galaxies can be explained by the sample being K-band selected and therefore containing both kinds of galaxies.

Garn & Best (2010) have investigated a sample of nearby star forming galaxies and given the dependence of dust attenuation of Hα luminosity $A_{\mathrm{H}\alpha}$ on stellar mass. Using $A_{\mathrm{FUV}}/A_{\mathrm{H}\alpha} = 1.68$ (Meurer et al. 2009), we overplot their result on Figure 4.5 to give a comparison of our result with this more global result derived from a larger sample. Our result is consistent with theirs to within 1σ uncertainty.

In more massive bins, the difference in dust attenuation between the paired and control galaxies becomes larger, implying that more massive galaxies are affected more strongly by merger process.

4.3.2 Dust attenuation in S-S and S-E pairs

Do spirals in S-S pairs and S-E pairs have different enhancements of dust attenuation? In the pair sample, there are 26 spirals in S-S pairs, and 9 spirals in S-E pairs. The mean A_{FUV} of spirals in S-S pairs and S-E pairs is 2.89 ± 0.31 mag and 2.63 ± 0.30 mag, respectively. The KS test shows that for spirals in S-S pairs the probability that the distribution of dust attenuation is the same as for control galaxies is 0.031, while for spirals in S-E pairs the probability is 0.603. Therefore, the A_{FUV} enhancement is mainly contributed by spirals in S-S pairs. It should be noted that the number of spirals in S-E pairs is small, and therefore may lack statistical significance. More data are needed to investigate whether or not the SSFRs are enhanced in spirals in S-E pairs.

Figure 4.6 shows the average A_{FUV} of spirals in S-S pairs and S-E pairs in each mass bin. This result indicates that an S-S interaction extends the duration of gas supply and makes massive galaxies able to have rich gas content, while an S-E interaction dissipates gas and makes massive galaxies more gas poor. The decrease of A_{FUV} in S-E

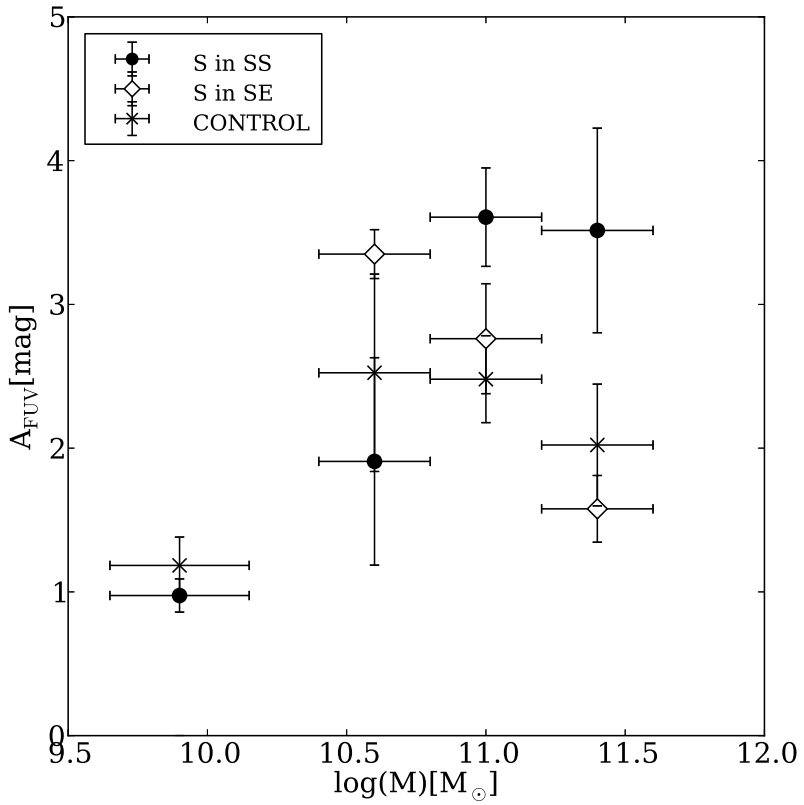

Figure 4.6 Dependence of $A_{\rm FUV}$ on galaxy stellar mass for non-AGN spirals in S-S pairs (circles), S-E pairs (diamonds), and for the control galaxies (crosses).

pairs presumably reflects that during an interaction with a hot-gas halo in early-type galaxies, late-type galaxies lose cold gas through hydrodynamic effects such as ram pressure stripping, viscous stripping, and thermal evaporation (Park & Choi 2009).

We define an enhancement parameter $\epsilon(A_{\rm FUV})$ as

$$\epsilon(A_{\rm FUV}) = A_{\rm FUV}^{\rm pair}[{\rm mag}] - A_{\rm FUV}^{\rm control}[{\rm mag}]. \tag{4.3}$$

The ϵ for paired and control galaxies are plotted in Figure 4.7. The enhancement for spirals in S-S pairs increases as the stellar mass of galaxies becomes larger, while the enhancement of spirals in S-E pairs shows the opposite trend. These trends can be

quantitatively described by the linear regressions

$$\begin{aligned}&\langle\epsilon^{S-S}(A_{\rm FUV})[{\rm mag}]\rangle\\ &= (-13.92\pm7.33)+(1.34\pm0.68)\log M[M_\odot]\end{aligned} \tag{4.4}$$

and

$$\begin{aligned}&\langle\epsilon^{S-E}(A_{\rm FUV})[{\rm mag}]\rangle\\ &= (17.68\pm1.44)-(1.59\pm0.13)\log M[M_\odot].\end{aligned} \tag{4.5}$$

The trend for spirals in S-E pairs still needs further tests because, as mentioned above, there are only nine galaxies in this sample so the result may not be representative. In the rest of this section, we focus on spirals in S-S pairs.

4.3.3 Dust attenuation in primaries and secondaries

The primary and secondary components may have different dust attenuations. Therefore, the spiral galaxies in S-S pairs are divided into primaries (13 galaxies) and secondaries (13 galaxies). The mean $A_{\rm FUV}$ of primaries is 3.01 ± 0.47 mag, and that of secondaries is 2.76 ± 0.41 mag. The difference is within the standard error. The KS test gives 0.828 as the possibility that these two samples are drawn from the same distribution. Figure 4.8 shows the mean $A_{\rm FUV}$ of primaries and secondaries in each mass bin. No apparent trend is found.

4.3.4 Separation and attenuation

The spatial separation between two components of a galaxy pair is another parameter that may affect dust attenuation. During different stage of merging, dust attenuation can change significantly. A smaller separation may indicate a later stage of merging, during which the amount and distribution of dust can be influenced more severely than at an earlier stage.

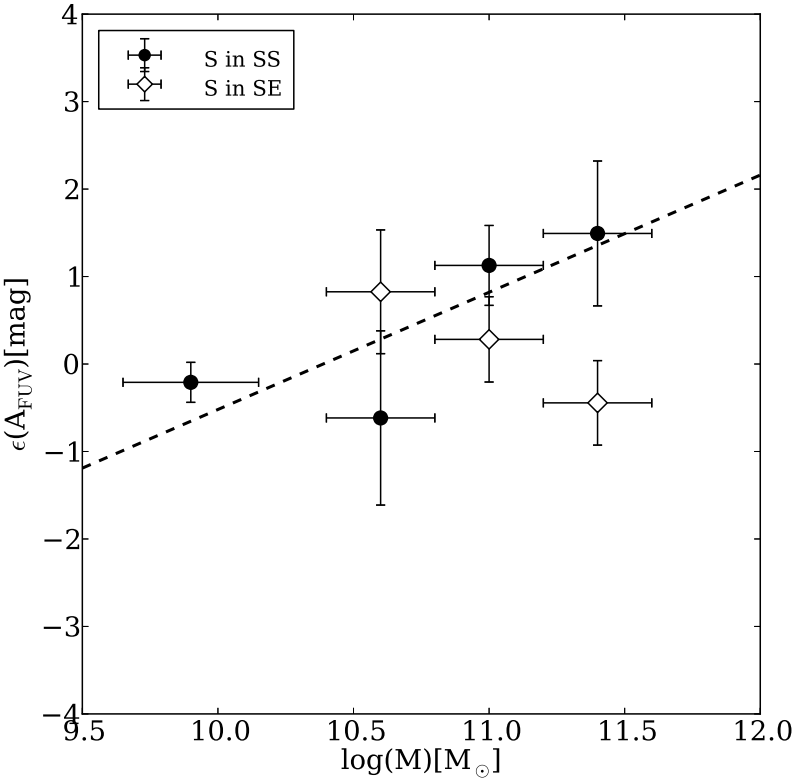

Figure 4.7 Dependence of $A_{\rm FUV}$ enhancement on galaxy stellar mass for spirals in S-S pairs (dots) and S-E pairs (diamonds). The dashed line is the linear regression for spirals in S-S pairs.

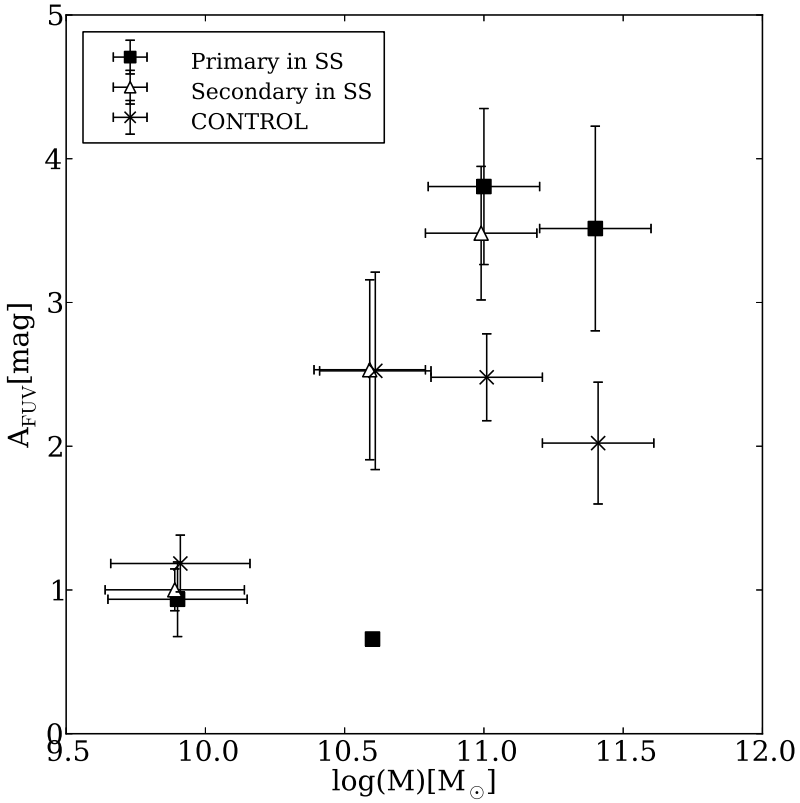

Figure 4.8 Mean $A_{\rm FUV}$ of primaries (squares) and secondaries (trianges) in S-S pairs and control galaxies (crosses) in different mass bins. Note that there is only one primary galaxy in the second mass bin.

We adopt the normalized separation parameter SEP, defined in Xu10:

$$\mathrm{SEP} = \frac{s}{r_1 + r_2}, \tag{4.6}$$

where s is the projected separation, and r_1 and r_2 are the K-band Kron radii of the primary and secondary from 2MASS, respectively. s, r_1 and r_2 have the same units.

The dust attenuation versus SEP plot shows quite a large scatter and no apparent trend (Figure 4.9). Therefore, the average values of A_{FUV} for galaxies in S-S pairs with SEP greater than 1 (17 galaxies) and less than 1 (9 galaxies) are examined instead, with the goal of investigating whether and how the separation affects dust attenuation. For round-shaped galaxies, when SEP is smaller than 1 the two components will overlap. The SEP 1 is chosen to divide the sample because this value is close to the mean SEP (1.12 ± 0.08) of the whole sample. It also makes our analysis consistent with Xu10 and allows a convenient comparison between our results and theirs.

The mean A_{FUV} is 2.64±0.39 mag for pairs with SEP greater than 1, and 3.36±0.48 mag for pairs with SEP less than 1. The difference is within the error. Figure 4.10 plots the mean A_{FUV} for spirals in S-S pairs with SEP greater than 1 and less than 1 in each mass bin. There is an increase in A_{FUV} for galaxies with SEP greater than 1 when the stellar mass of galaxies increases, while hardly any trend can be seen for galaxies with SEP less than 1. It is possible that at intermediate distances, the gas content can be enriched, whereas the situation becomes more complicated when the two galaxies come closer (for instance, increasing SFRs may deplete gas), but this result may be biased by the projection effect.

4.3.5 IRX-β Relation

With FUV, NUV and IR data, we can examine the IRX-β relation in paired galaxies and in their nuclei. IRX is the IR to UV ratio. β is the slope of the UV spectrum assuming a power law $F_\lambda \propto \lambda^\beta$, and can be inferred from the difference between the FUV and NUV bands (Kong et al. 2004). The IRX-β relation has been intensively discussed in many works. Several formulae have been proposed to represent the relation for different types of galaxies. To name a few, Boissier

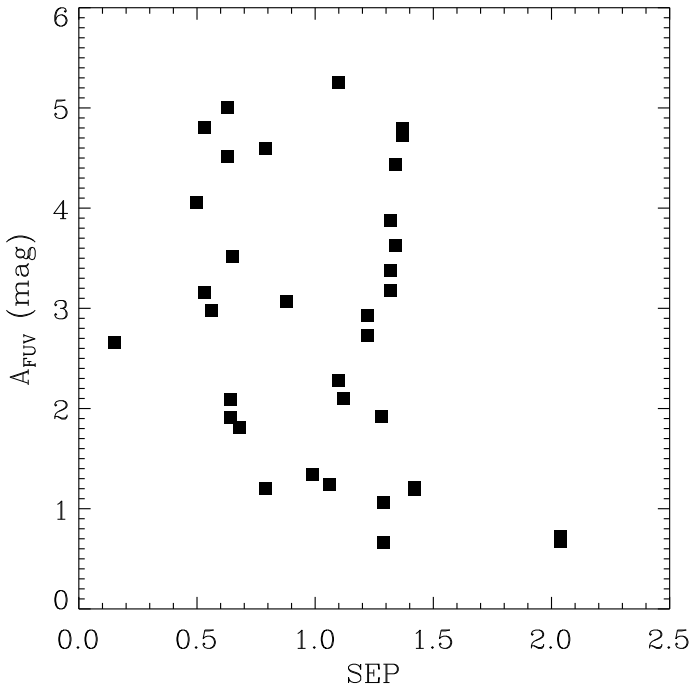

Figure 4.9 Dependence of $A_{\rm FUV}$ of paired galaxies on the normalized separation SEP defined in Equation (4.6).

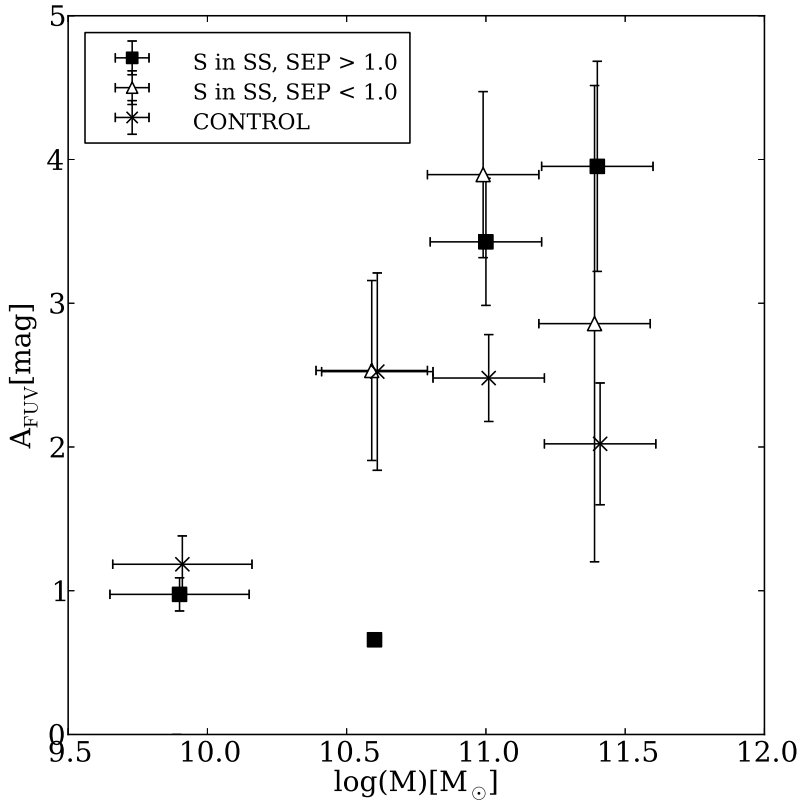

Figure 4.10 Mean $A_{\rm FUV}$ of non-AGN spirals in S-S pairs with normalized separations (SEP) greater than 1 (squares) and less than 1 (triangles) in different mass bins. There is only one galaxy with SEP>1 in the second mass bin. The crosses are the galaxies in the control sample.

et al. (2007), Cortese et al. (2006), Meurer et al. (1999), Muñoz-Mateos et al. (2009), Overzier et al. (2011), Takeuchi et al. (2012), etc. In Figure 4.11, we plot IRX versus β for the paired and control galaxies, and overplot the relations given by Meurer et al. (1999), Muñoz-Mateos et al. (2009) and Takeuchi et al. (2012) as comparisons. Meurer's law is only applicable to starburst galaxies. Takeuchi et al. (2012) rederived the relation for the same sample with newer data and corrected for the aperture effect. Muñoz-Mateos et al. (2009) investigated the relation for more quiescent galaxies using a SINGS sample.

In Figure 4.11, the solid line indicates Meurer's law, the dashed line represents the result from Takeuchi et al. (2012), and the dotted line is the result from Muñoz-Mateos et al. (2009). The control galaxies follow these lines closely. In contrast, the paired galaxies are severely dispersed from the lines. The locations of the paired galaxies are spread from the region where the quiescent galaxies are locate to where the Goldader et al. (2002) ULIRGs reside. The large scatter for paired galaxies in the IRX-β diagram suggests that interaction complicates the physical processes on dust attenuation. Most of paired galaxies have a similar location to those found by Jonsson et al. (2006) for luminous mergers using numerical simulations. The positions of the nuclear regions of paired galaxies are similar to those of the ULIRGs in Goldader et al. (2002). This is consistent with an interaction injecting gas into galaxies, especially in the nuclear regions. The central regions of ULIRGs are more extreme and show the largest deviations from the IRX-β laws. These deviations can be explained by these galaxies, especially the central parts, being strongly obscured by dust. Only a very small fraction of UV light can be detected, and thus IRX has very little correlation with β (Goldader et al. 2002).

4.4 SFRs in merger galaxies

In Section 3, we find that the distributions of dust attenuation in paired and control galaxies are different, and that the attenuation is dependent on morphology and mass. Therefore, the result of Xu10 may be significantly affected by their not including the UV part of SFRs. A safe way to calculate the SFRs in galaxies is to

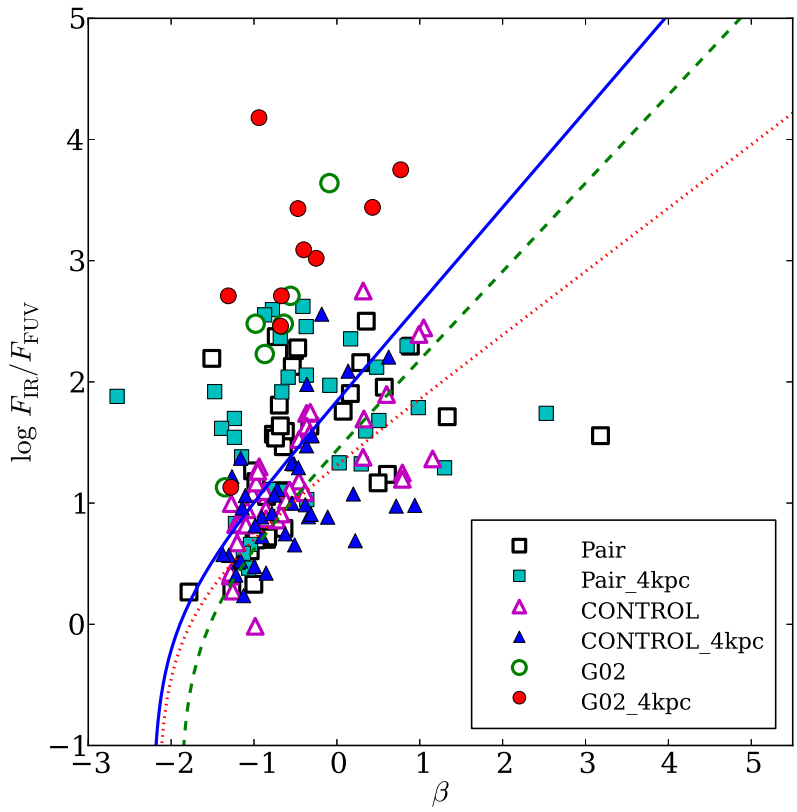

Figure 4.11 IRX-β relation for spirals in the pair sample (squares) and their counterparts in the control sample (triangles). The circles are the results for ULIRGs from Goldader et al. (2002). Filled symbols represent the quantities within a 4 kpc aperture. The results of Meurer et al. (1999) (solid line), Muñoz-Mateos et al. (2009) (dotted line) and Takeuchi et al. (2012) (dashed line) are plotted as reference.

combine the obscured SFRs and unobscured SFRs (e.g. Takeuchi et al. 2005a; Buat et al. 2005; Cortese et al. 2006). Assuming a constant burst of star formation for 10^8 yr and a Salpeter initial mass function (IMF Salpeter 1955), Buat et al. (2007) present SFR calculations using FUV and IR luminosity as follows:

$$\log \mathrm{SFR_{FUV}}[M_\odot \mathrm{yr}^{-1}] = \log L_{\mathrm{FUV}}[L_\odot] - 9.51 \tag{4.7}$$

$$\log \mathrm{SFR_{IR}}[M_\odot \mathrm{yr}^{-1}] = \log L_{\mathrm{IR}}[L_\odot] - 9.75. \tag{4.8}$$

To calculate the total SFR, the two parts should be added together. Since the IR emission is not only from dust heated by massive young stars, but also from old stars, the contribution of the latter should be removed. The obscured SFRs ($\mathrm{SFR_{dust}}$) are then given by

$$\mathrm{SFR_{dust}} = (1-\eta)\mathrm{SFR_{IR}}. \tag{4.9}$$

Therefore, the total SFRs are given by

$$\mathrm{SFR_{TOT}} = \mathrm{SFR_{FUV}} + (1-\eta)\mathrm{SFR_{IR}}, \tag{4.10}$$

where η is the fraction of IR emission by old stars. We use $\eta = 0.3$ as suggested by Buat & Xu (1996). Hirashita et al. (2003) give a larger value of 0.4. Bell (2003) estimated η to be 0.32 ± 0.16 for galaxies with $L_{\mathrm{IR}} < 10^{11} L_\odot$, and 0.09 ± 0.05 for galaxies with $L_{\mathrm{IR}} > 10^{11} L_\odot$. Buat et al. (2011) found an average value of 0.17 ± 0.10 for a sample of star forming galaxies. In paired galaxies, the contribution from old stars should be less because of the higher star formation activity. Therefore, the SSFRs enhancement in paired galaxies is actually stronger than we have estimated. However, it should be stressed that the difference is not significant. Although Bell (2003) give an apparently lower η for galaxies with $L_{\mathrm{IR}} > 10^{11} L_\odot$, only three galaxies with such high luminosities are included in our sample. Even if $\eta = 0.09$ is taken, the total SFRs are at most 0.1 dex larger than using $\eta = 0.3$, which is within the uncertainty.

For the 39 spirals in pairs and their control galaxies, $\mathrm{SFR_{TOT}}$, $\mathrm{SFR_{FUV}}$, $\mathrm{SFR_{dust}}$, and the fraction of total SFRs contributed by FUV parts are listed in Table 4.4. The distributions of the fractions of $\mathrm{SFR_{FUV}}$ for paired and control galaxies are quite

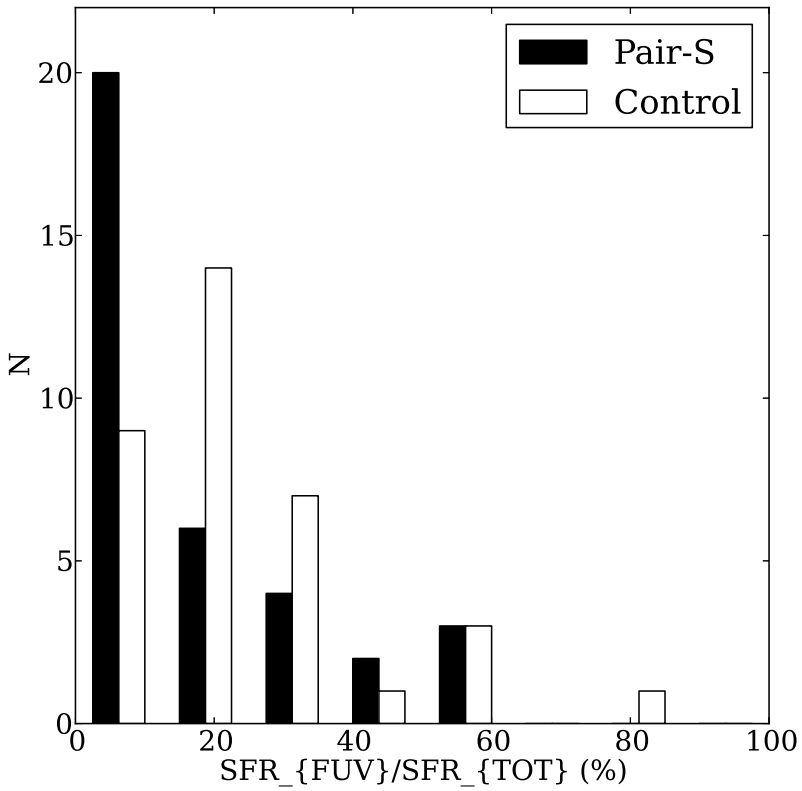

Figure 4.12 Histograms of $\mathrm{SFR_{FUV}/SFR_{TOT}}$ distributions for spirals in the pair and control samples.

different (Figure 4.12; the KS test gives 0.024). The FUV indicated SFRs contribute from several percent to as high as 80 percent, which can be sufficient to affect the distribution of the total SFRs.

Figure 4.13 shows a the comparison of histograms of SFRs for the pair and control samples. The histograms show a significant excess of paired galaxies in the high SFR end. There are 5 galaxies with log(SFR) larger than 1 in the pair sample, but none in the control sample. The KS test gives 0.049, quite a low value for the null hypothesis that these two samples are drawn from the same population. The mean log(SFR) in pair and control samples are 0.32 ± 0.12 and 0.06 ± 0.07, respectively. The fact that both dust attenuation and SFRs are found enhanced in paired galaxies is consistent with the correlation between SFRs and A_{FUV} found by previous studies (e.g. Brinchmann et al. 2004; Iglesias-Páramo et al. 2004).

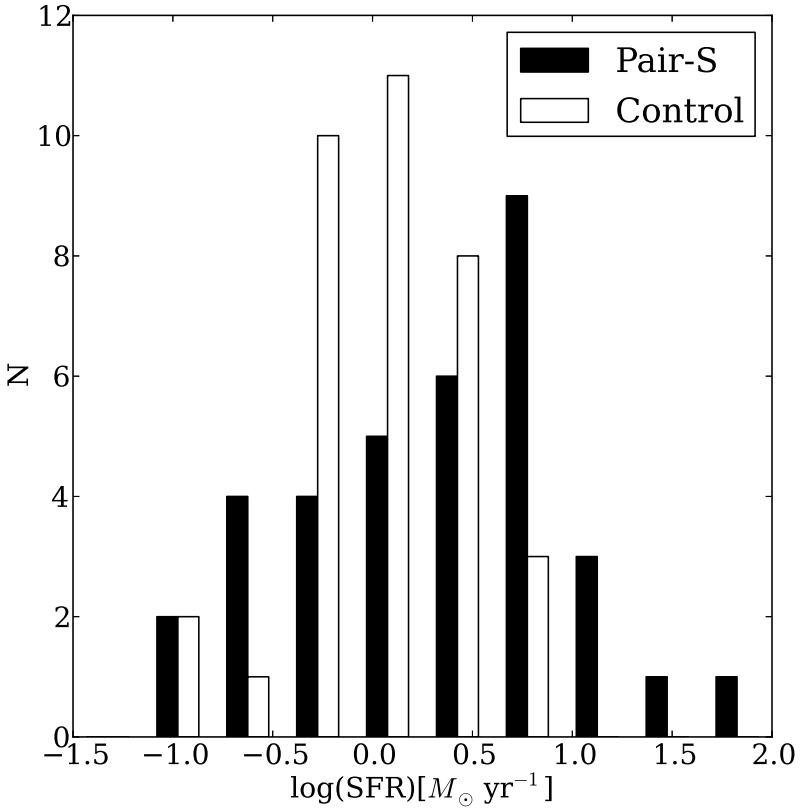

Figure 4.13 Histograms of SFR distributions for spirals in the pair and control samples.

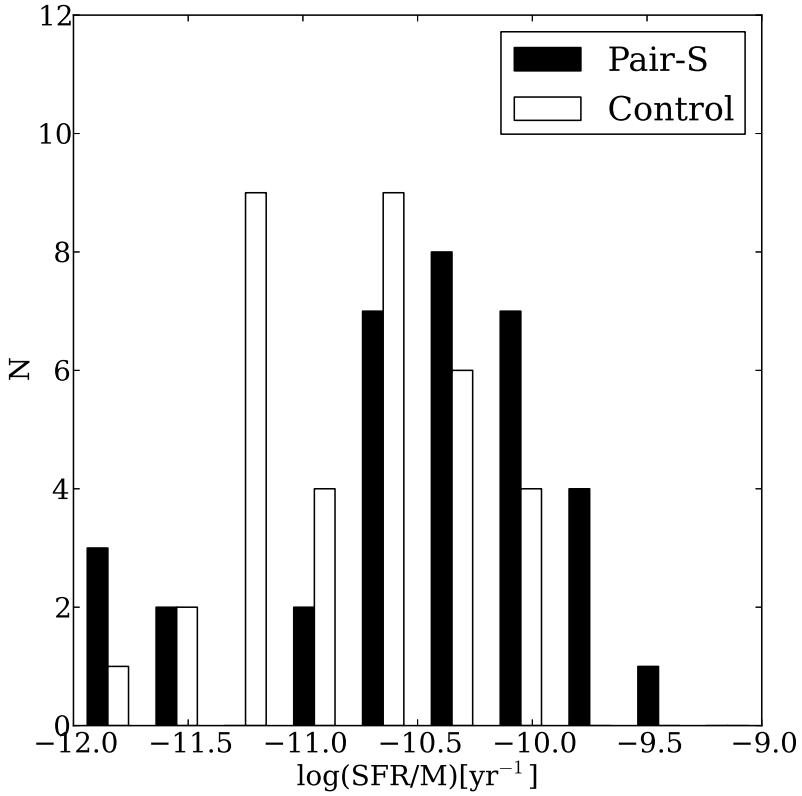

Figure 4.14 Histograms of SSFR distributions for spirals in the pair and control samples.

Table 4.6. Average SSFRs for paired and control galaxies in four different mass bins.

Mass bins	logSSFR (yr^{-1})			
	pair	control	S in S-S	S in S-E
$9.7 < \log(M/M_\odot) < 10.2$	-10.28±0.15	-10.23±0.08	-10.28±0.15	...
$10.2 < \log(M/M_\odot) < 10.8$	-10.36±0.05	-10.78±0.21	-10.38±0.08	-10.33±0.03
$10.8 < \log(M/M_\odot) < 11.2$	-10.62±0.20	-10.86±0.10	-10.38±0.21	-11.24±0.34
$11.2 < \log(M/M_\odot) < 11.6$	-10.67±0.21	-11.03±0.18	-10.65±0.30	-10.72±0.16

The SFR normalized by the stellar mass M is SSFR:

$$\mathrm{SSFR}[\mathrm{yr}^{-1}] = \frac{\mathrm{SFR}[M_\odot \mathrm{yr}^{-1}]}{M[M_\odot]}. \tag{4.11}$$

Table 4.4 lists the results of $\mathrm{SSFR_{TOT}}$ ($\mathrm{SFR_{TOT}}/M$) for paired and control galaxies. The total SSFR distributions of pair and control samples are shown in Figure 4.14. (Hereafter, we abbreviate $\mathrm{SSFR_{TOT}}$ as SSFR.) The two distributions show significant differences from each other. The KS test yields a probability of 0.024. The mean logSSFR is -10.54 ± 0.11 for the pair sample, and -10.79 ± 0.08 for the isolated control sample. Therefore, the paired galaxies show an apparent enhancement of SFRs and SSFRs. This result is consistent with Xu10's conclusion.

4.4.1 Dependence of SSFR enhancement on Mass

The mass dependence of SSFR enhancement is examined following Xu10's method. The galaxies are divided into 4 groups with different masses (Table 4.6). The average SSFR versus mass of each group is plotted in Figure 4.15. The result of Brinchmann et al. (2004) is overplotted to give a comparison. Our result shows good consistency with their result which was derived from a more generally selected sample.

Figure 4.15 shows that the more massive galaxies have stronger enhancement of

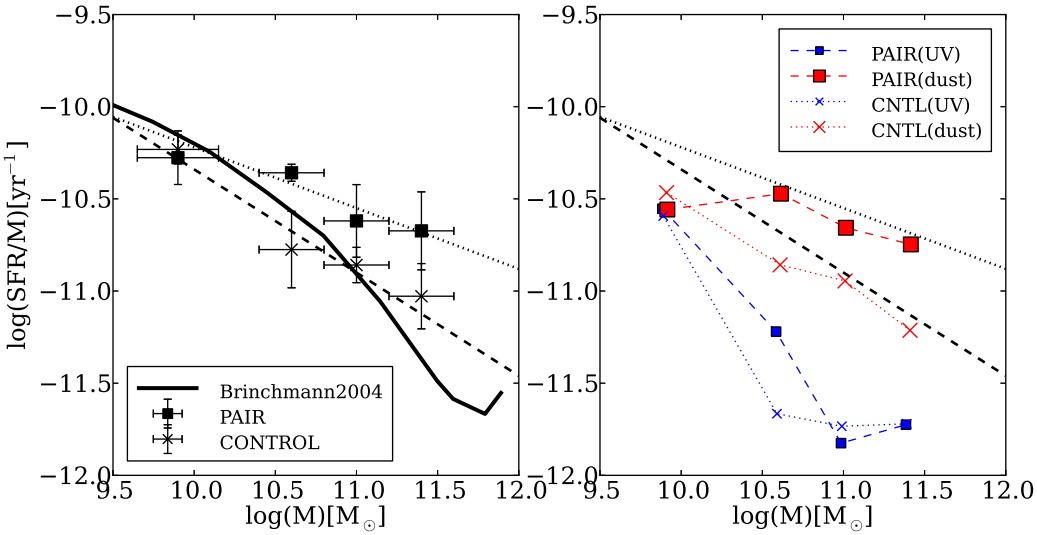

Figure 4.15 Left: Dependence of SSFRs on galaxy stellar mass for paired galaxies (squares) and for the control sample (crosses). The solid line is the result given by Brinchmann et al. (2004), modified for initial mass function (IMF) and H_0. Right: Similar to left, but divided into UV (small symbols) and dust (large symbols) parts. The dotted line shows the linear regression of the SSFRs-mass relation for spirals in paired galaxies, and the dashed line for control galaxies.

SSFR, implying massive galaxies affect each other more severely. Xu10 found that the SSFRs of spirals in pairs are nearly constant; however, here a decreasing trend is also found for paired galaxies although not as apparent as for the control sample:

$$\begin{aligned} &\mathrm{SSFR}^{\mathrm{pair}}[\mathrm{yr}^{-1}] \\ &= (-7.28 \pm 0.75) - (0.30 \pm 0.07) \log M[M_{\odot}], \end{aligned} \tag{4.12}$$

and

$$\begin{aligned} &\mathrm{SSFR}^{\mathrm{ctrl}}[\mathrm{yr}^{-1}] \\ &= (-4.94 \pm 1.08) - (0.53 \pm 0.10) \log M[M_{\odot}]. \end{aligned} \tag{4.13}$$

The decreasing trends for both control and paired galaxies are shown in Figure 4.15. The difference between this result and Xu10's is due to the FUV contribution. The right panel of Figure 4.15 presents the dust obscured and unobscured parts of SFRs. Although the dust obscured SSFRs are almost constant, $\mathrm{SSFRs}_{\mathrm{FUV}}$ become less and less as the mass increases.

4.4.2 SSFR Enhancement in S-S and S-E pairs

As mentioned in Section 4.3.2, among our spirals there are 26 spirals in spiral-spiral (S-S) pairs and 9 spirals in spiral-elliptical (S-E) pairs. Xu10 found that only the SSFRs of spirals in S-S pairs are enhanced. After adding the unobscured SFRs, we found the mean logSSFR of spirals in S-S pairs is -10.41 ± 0.12, and that of spirals in S-E pairs is -10.92 ± 0.22. The KS test shows the possibility of the distributions of SSFRs of spirals in S-S pairs and in their control galaxies are drawn from the same sample is 0.031, and the possibility is 0.957 for spirals in S-E pairs, consistent with Xu10's result.

Figure 4.16 shows the mass dependence of SSFR for spirals in S-S and S-E pairs. Spirals in S-S pairs follow the trend described by Equation (4.12). On the other hand, the SSFRs of spirals in S-E pairs show no dependence on mass. The right panel of

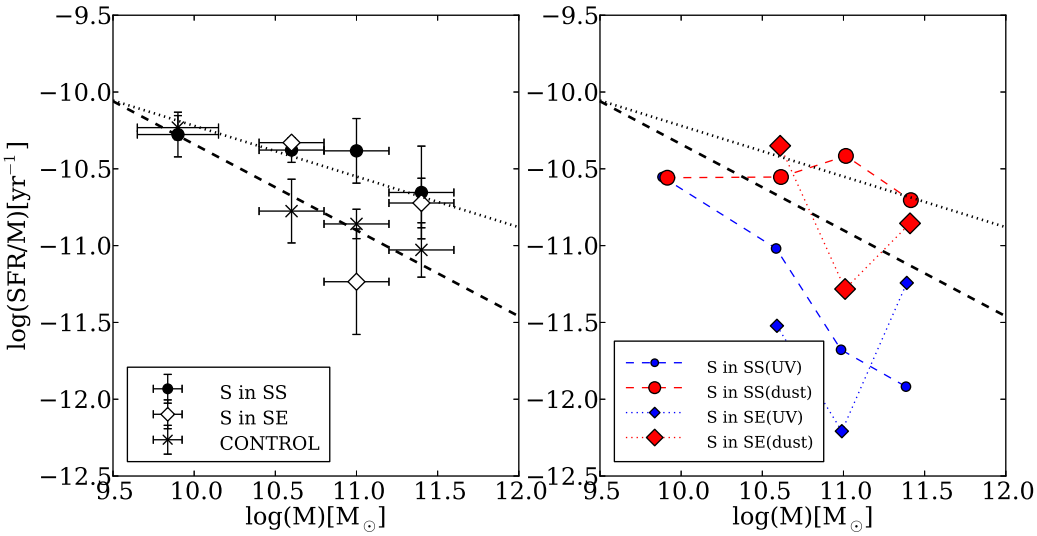

Figure 4.16 Left: Dependence of SSFRs on galaxy stellar mass for non-AGN spirals in S-S pairs (dots), S-E pairs (diamonds), and for the control sample (crosses). Right: Similar to left, but divided into UV (small symbols) and dust parts (large symbols). The lines are the same as in Figure 4.15.

Figure 4.16 presents the obscured and unobscured parts of SSFRs for S-S and S-E pairs. The SSFRs of spirals in S-E pairs, for either the obscured or unobscured parts, do not have an apparent dependence on mass. Unlike how the fraction of unobscured SSFRs reduces for spirals in S-S pairs, the contribution of unobscured SSFRs of spirals in S-E pairs remains similar as the mass increases. For spirals in S-S pairs, the average contribution of unobscured SSFRs at higher mass becomes lower, implying heavier dust attenuation.

As defined by Xu10, the SSFR enhancement indicator ϵ is

$$\epsilon = \log \mathrm{SSFR}_{\mathrm{PAIR-S}} - \log \mathrm{SSFR}_{\mathrm{control}}. \tag{4.14}$$

Figure 4.17 plots the dependence of ϵ on mass. There is an apparent increasing trend for spirals in S-S pairs, while there is no trend for spirals in S-E pairs. The correlation between the enhancement in S-S pairs and the stellar mass of galaxies is

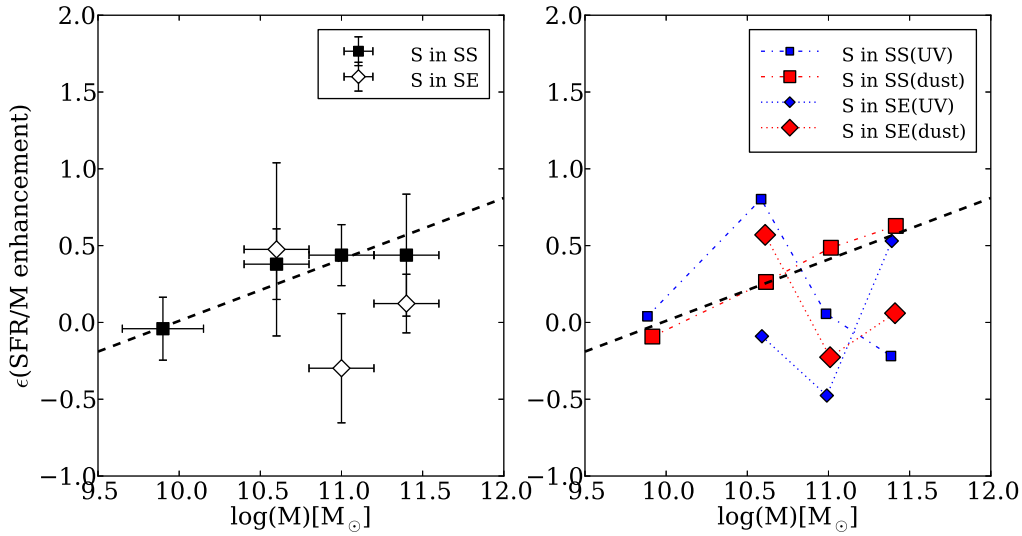

Figure 4.17 Left: Dependence of SSFR enhancement on galaxy stellar mass for spirals in S-S pairs (squares) and S-E pairs (diamonds). Right: Similar to left, but divided into UV (small symbols) and dust parts (large symbols). The dashed line shows the linear regression for spirals in S-S pairs.

found to be

$$\begin{aligned} \langle \epsilon \rangle_{\mathrm{S+S}} &= 0.01(\pm 0.08) \\ &\quad +0.40(\pm 0.09) \log \frac{M}{(10^{10} M_{\odot})}, \end{aligned} \tag{4.15}$$

which is consistent with Xu10's result within the uncertainties.

The obscured and unobscured SSFRs for spirals in S-S and S-E pairs are also plotted in Figure 4.17. The obscured SSFRs of spirals in S-S pairs have an increasing enhancement as the mass of galaxies increases. However, the unobscured SSFRs of spirals in S-S pairs do not show this trend.

4.4.3 SSFRs in Primaries and Secondaries

Woods & Geller (2007) and Ellison et al. (2008) found that secondary components of paired galaxies show stronger enhancements than primary components. Xu10 argue that there is no significant difference between the mean SSFR of primaries and

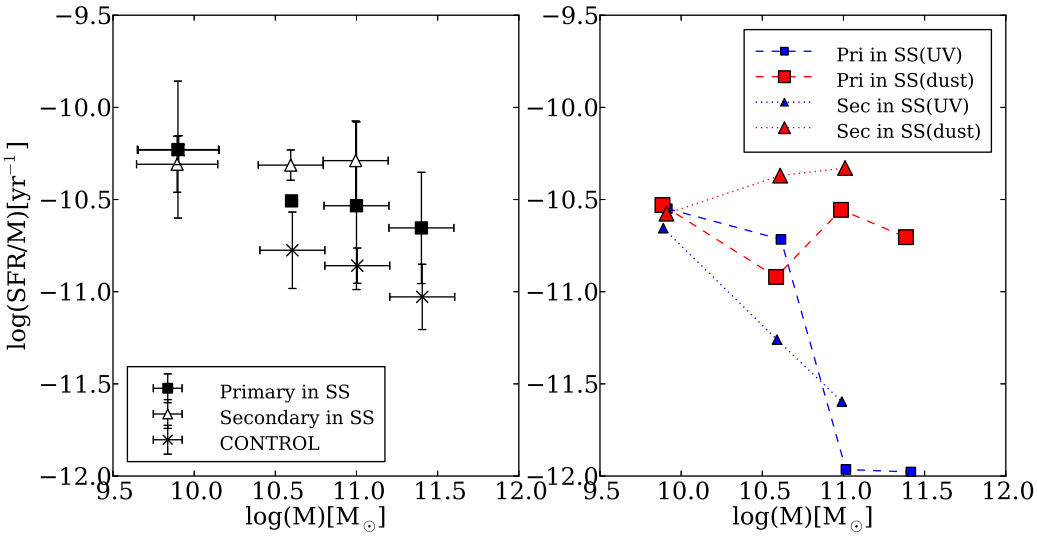

Figure 4.18 Left: Mean SSFRs of primaries (squares) and secondaries (triangles) of galaxies in S-S pairs in different mass bins. Note that there is only one primary galaxy in the second mass bin. Crosses represent galaxies in the control sample. Right: Similar to left, but divided into UV (small symbols) and dust parts (large symbols).

secondaries in any of the mass bins they studied. Here we check the total SSFRs in primaries and secondaries in paired galaxies and in their counterparts in the control sample. The mean logSSFRs of primaries is -10.53 ± 0.20, and that of secondaries is -10.30 ± 0.13. Although the secondaries have larger average SSFRs the difference is within the standard error. The KS test for the primaries and secondaries gives a probability of 0.226, so it is hard to conclude whether the distributions are different or not.

The mass dependence of the SSFRs of primaries and secondaries is also examined (Figure 4.18). It seems the secondaries have larger SSFRs in more massive bins, but the difference is not significant. No significant difference is found between the primaries and secondaries in each mass bin for both obscured and unobscured SSFRs.

4.4.4 Enhancement in one or two components

KS tests for the secondaries and control galaxies and for the primaries and control sample give probabilities of 0.098 and 0.190, respectively, indicating that both primaries and secondaries in the pair sample are distributed differently from the control sample. Figure 4.20 confirms the trend found in Figure 14 in Xu10: when one component has strong star formation activity, the other component is also actively star forming.

Holmberg found that in paired galaxies the two components tend to have similar colors, which implies a sign of co-evolution of the two components (Holmberg 1958). Xu10 examined the Holmberg effect by comparing the SSFRs of the two components in ten massive S-S galaxies. Here we also examine the Holmberg effect in the two components of nine massive paired galaxies ($\log(M/M_{\odot}) > 10.7$). Massive pairs are examined because only these pairs show an apparent enhancement of SSFRs, which indicates the merging influence on each component. Figure 4.20 shows that there is concordance of the two components. The correlation coefficient is 0.457 for the two components in paired galaxies, and is 0.007 for their counterparts in the control sample. The correlation between the two components is less tight than Xu10's result, where a coefficient of 0.58 was found. Our result shows the two components in pairs show evidence of co-evolution.

4.4.5 Separation and SSFRs

It is hard to see any trend in the scatter plot of SSFRs versus the normalized separation SEP (Figure 4.21). Therefore, as in Section 4.3.4, the average property is investigated by separating the spirals in S-S pairs into two groups: one with SEP greater than 1, and the other with SEP less than 1. The mean logSSFR for paired galaxies with SEP greater than 1 is -10.38 ± 0.15, and for those with SEP less than 1 it is -10.49 ± 0.22. No significant difference is found in the distributions of the two groups (KS test gives 0.802). Figure 4.22 plots the average SSFRs of paired galaxies for these two groups in each mass bin as well as for their obscured and unobscured parts. No systematic trend is found except that the unobscured SSFRs for pairs with

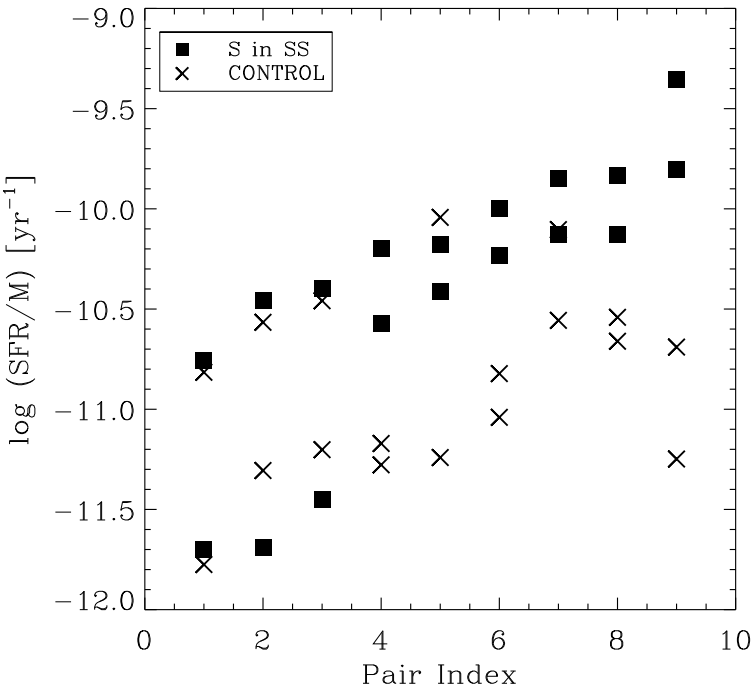

Figure 4.19 SSFRs of paired galaxies with mass greater than $10^{10.7} M_{\odot}$. Squares show the paired galaxies arranged in order of the higher SSFR value of each pair. Crosses show the control galaxies.

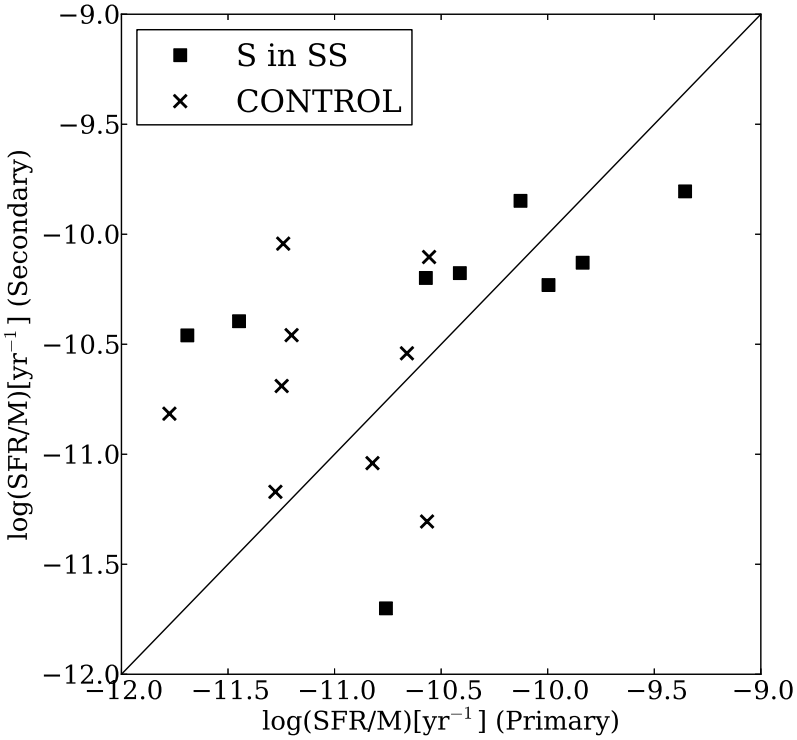

Figure 4.20 Correlation between SSFRs of two components in the S-S pairs with M $\geq$ $10^{10.7}$M$_{\odot}$. Squares and crosses represent spirals in the pair and control samples, respectively.

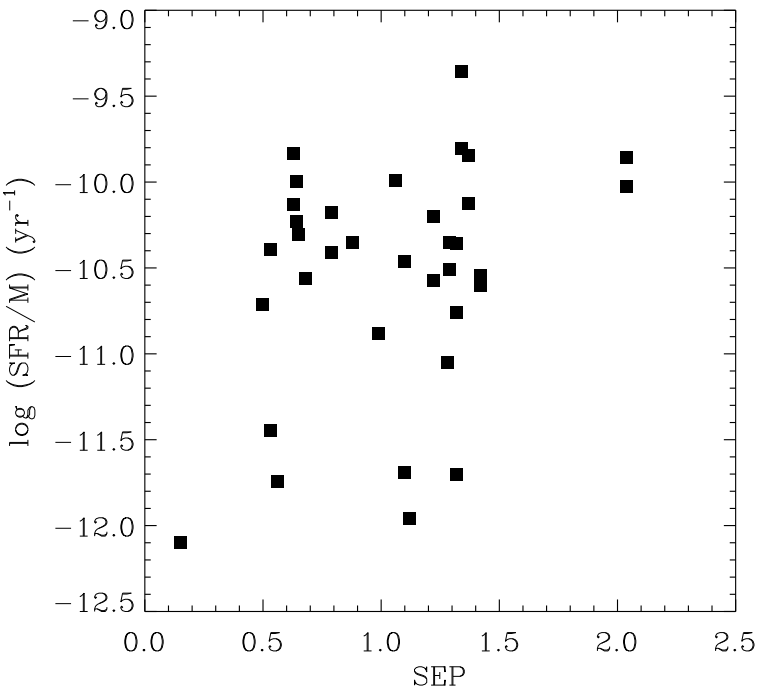

Figure 4.21 Dependence of log SSFR of paired galaxies on the normalized separation SEP defined in Equation (4.6).

SEP larger than 1 seem to decrease as the mass increases. Although previous studies (e.g. Xu & Sulentic 1991; Barton et al. 2000; Lambas et al. 2003, etc.) conclude that paired galaxies with separation $\gtrsim 20h^{-1}$ kpc have stronger enhancement of SFRs than those with separation $\lesssim 20h^{-1}$ kpc, the separation seems not to be a determining parameter of star formation activity for mergers with separation $\lesssim 20h^{-1}$ kpc. There may be several conflicting factors that can affect the outcome. As Xu10 suggested, galaxies with smaller separations may undergo gas depletion due to prolonged star formation activity at the place where the two galaxies overlapped. Also, the projection effect may confuse efforts to probe the actual dependence on the true 3D separations.

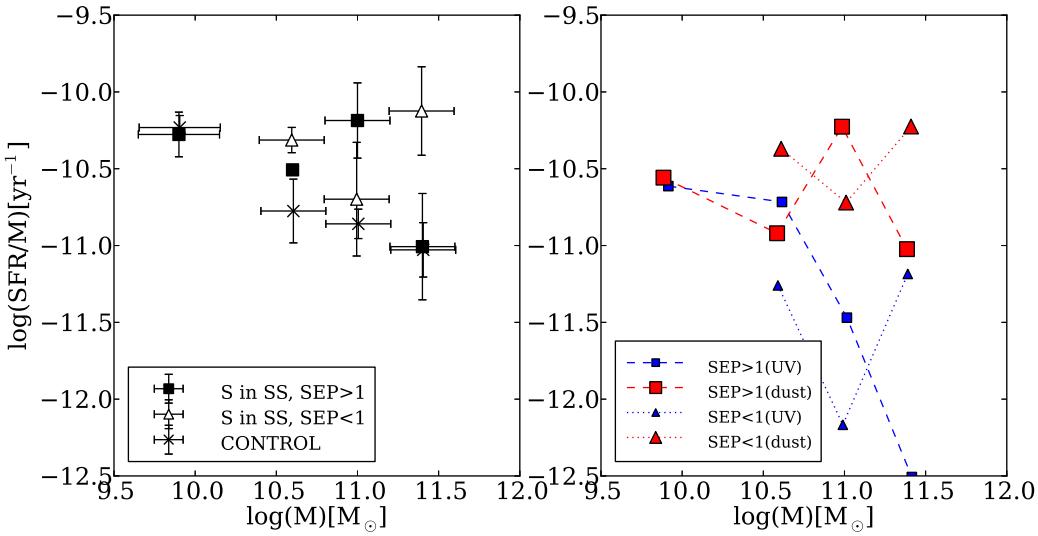

Figure 4.22 Left: Mean SSFRs of spirals in S-S paired galaxies with SEP greater than 1 (squares) and less than 1 (triangles) in different mass bins. There is only one galaxy with SEP>1 in the second mass bin. Crosses show the galaxies in the control sample. Right: Similar to left, but divided into UV (small symbols) and dust parts (large symbols).

4.4.6 SFRs in nuclear regions

From Tables 4.2 and 4.3, the SFRs inside 4 kpc and 10 kpc are derived. The nuclear contributions to unobscured SFRs (FUV), obscured SFRs (dust) and their combination are all plotted in Figure 4.23. The median nuclear contribution of unobscured SFRs is 15% for paired galaxies and 6% for control ones. The difference becomes even larger for the obscured part: the average nuclear contribution of obscured SFRs reaches 33% for paired galaxies, while it becomes 5% for control ones. For the combination of the two parts, the nuclear contribution is 30% for paired galaxies, and is 5% for the control ones. These results are consistent with the theory that a starburst is triggered in the centre of galaxies because of the gas inflow induced by the interaction. Compared to Kennicutt et al. (1987) and Kennicutt & Kent (1983)'s results derived from Hα images (in which the central regions contributes 13% and 4%), our result is larger. This may be due to the different aperture size: Kennicutt et al. (1987) used an aperture size of $4.7''$, while we used 4 kpc, which corresponds to an average aperture size of $\sim 9''$ for the pair sample and $\sim 7''$ for the control sample.

4.5 The Importance of Including the UV part of SFRs

Our results for SSFRs basically agree with the conclusions generated by Xu10, but our findings on dust attenuation in pair and control samples are not similar, as we have shown in Sections 4.3 and 4.4. From Table 4.4, we can see that in spite of some galaxies having contributions of the $\mathrm{SSFR_{FUV}}$ larger than 50%, the average contributions of $\mathrm{SSFRs_{FUV}}$ are 17.1%±3.1% and 22.7%±3.1% for paired and control galaxies, respectively. On average, the UV part of SSFRs contribute much less to the total SSFRs than the IR part of SSFRs. The average SSFR is -10.54 ± 0.11 in our study, which is very close to that obtained by Xu10 (-10.50 ± 0.10). Therefore, the contribution to the total cosmic star formation density is in agreement with Xu10's result within the errors. The average contribution of $\mathrm{SSFRs_{FUV}}$ calculated here is less than the mean value given by Takeuchi et al. (2005a) because our sample is

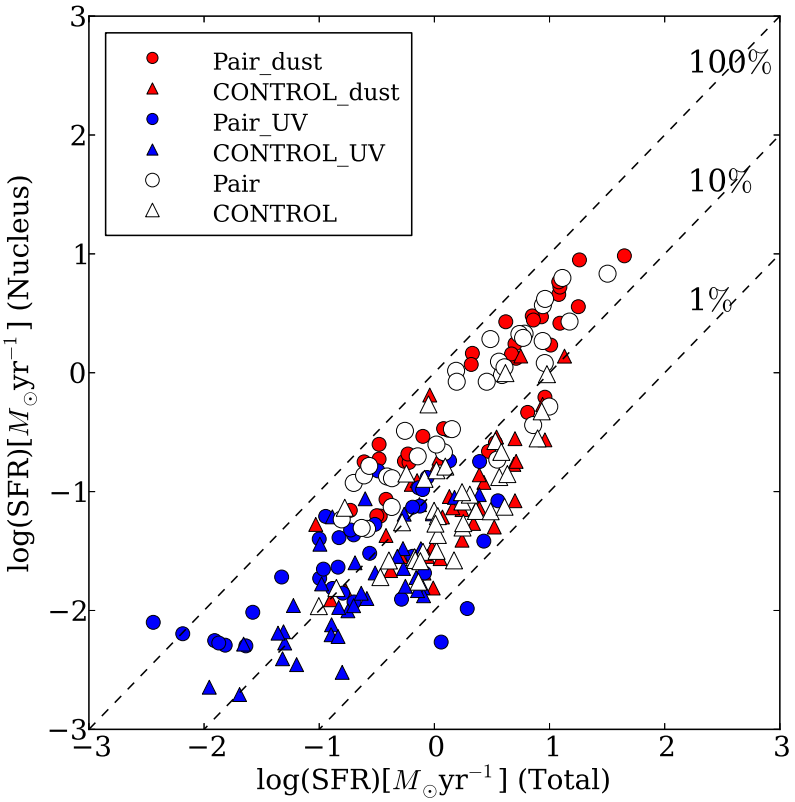

Figure 4.23 Comparison of SFRs included within a 4 kpc aperture and SFRs of a whole galaxy. The $\mathrm{SFRs_{FIR}}$ (dust obscured SFRs) are shown in red, $\mathrm{SFR_{FUV}}$ (unobscured) in blue, and the total SFRs in white. Spirals in the pair and control samples are shown as circles and triangles, respectively. The lines indicate 1%, 10% and 100% nuclear contributions to the total SFRs.

NIR/optical selected, while their sample is more general and includes objects such as small galaxies with luminous UV emission. Also, their analysis is based on luminosity functions, and therefore volume corrections are accounted for and cannot be compared easily to invividual groups.

Nevertheless, the $\mathrm{SSFR_{FUV}}$ in different mass bins are still worth investigating, since the galaxies with large $\mathrm{SSFR_{FUV}}$ may fall in the same mass bin and change the total SSFRs distribution severely. We find that as the stellar mass of galaxies increases, the enhancement also increases. Our studies on companion morphologies, primaries and secondaries, the Holmberg effect, and on the dependence of separations also give similar results to Xu10. However, the SSFRs for paired galaxies show a slight decrease as the mass of galaxies increases, which is unlike Xu10's Figure 5 with almost constant SSFRs. One may argue that in more massive bins, the old stellar contribution becomes smaller and the trend may be due to using a constant η. However, this trend still exists even if we reduce the contribution of the old-stellar population η to 9% for the two bins with larger mass. This trend is caused by the decreasing UV contribution as the mass increases, implying that at the low mass end the UV contribution is quite important and should not be ignored, although in this work the trend is weak and does not affect the calculation of cosmic star formation density. We find the cosmic star formation density contributed by spirals in paired galaxies is 2.0×10^{-4} $M_\odot$ $\mathrm{yr^{-1}}$ $\mathrm{Mpc^{-3}}$ (the spiral fraction is kindly provided by C. K. Xu, private communication), which is consistent with Xu10's result of 2.54×10^{-4} $M_\odot$ $\mathrm{yr^{-1}}$ $\mathrm{Mpc^{-3}}$.

4.6 Summary and Conclusions

We presented FUV and NUV photometry results for a local sample of paired galaxies. By combining the UV and IR data, we investigated the dust attenuation and SFRs in merging spirals and in a control sample of isolated galaxies. Dust attenuation is calculated using UV and IR fluxes and compared between the pair and control samples. SFRs indicated by UV are compared with SFRs indicated by IR, and then the UV and IR parts SFRs are combined to give the total SFRs and

SSFRs to study the enhancement of star formation activity in paired galaxies. The results are compared to Xu10's results that are based on IR images. We also studied the difference in dust attenuation and SSFRs between spiral galaxies in S-S pairs and S-E pairs, between primaries and secondaries, and between paired galaxies with normalized separations SEP greater than 1 and those with SEP less than 1. The KS test results for the mean $A_{\rm FUV}$ and SSFRs in each group are summarized in Tables 4.7 and 4.8. We come to the following conclusions:

1. Dust attenuation in paired and control galaxies shows different distributions. Paired galaxies tend to have heavier dust attenuation than isolated ones.

2. The enhancement of dust attenuation depends on the morphology of paired galaxies: spirals in S-S pairs have higher dust attenuation than control galaxies but spirals in S-E pairs do not.

3. No systematic difference in dust attenuation is found between primaries and secondaries. Dust attenuation in galaxies with SEP greater than 1 and those with SEP less than 1 in S-S pairs do not show significant difference.

4. Our investigation of total SSFRs in paired galaxies confirms Xu10's IR data only results. The reason is that in our galaxies, the dust obscured SSFRs dominate the total SSFRs at an average level.

5. Including $\rm SSFR_{FUV}$ affects the less massive galaxies most. Nevertheless, this inclusion hardly changes the contribution of paired galaxies to the cosmic SFR in the local universe.

6. Paired galaxies show a stronger concentration of IR emission and dust attenuation in their nuclear regions than control galaxies do, which is evidence for merger-induced starbursts.

7. In the IRX-β diagram (Figure 4.11), paired galaxies show larger scatter than control galaxies. The nuclear regions of paired galaxies are located in a similar region to ULIRGs.

Table 4.7. Average $A_{\rm FUV}$ and SSFRs for different subsamples of galaxies. The number in the bracket indicates the number of galaxies in each subsample.

	Control(35)	pair(35)	S in S-S(26)	S in S-E(9)	S in S-S			
					Primary(13)	Secondary(13)	Sep>1(17)	Sep>1(9)
$A_{\rm FUV}$ (mag)	2.20 ± 0.21	2.82 ± 0.24	2.89 ± 0.31	2.63 ± 0.30	3.01 ± 0.47	2.76 ± 0.41	2.64 ± 0.39	3.36 ± 0.47
logSSFR ($\rm yr^{-1}$)	-10.79 ± 0.08	-10.54 ± 0.11	-10.41 ± 0.12	-10.92 ± 0.22	-10.53 ± 0.20	-10.30 ± 0.13	-10.38 ± 0.15	-10.49 ± 0.22

Table 4.8. Summary of results of KS tests for $A_{\rm FUV}$ and SSFRs between different subsamples of galaxies.

	Control vs. Pair	S-S vs. Control	S-E*vs. Control	Pri. vs. Sec.	Sep> 1 vs. Sep< 1*
$A_{\rm FUV}$	0.024	0.031	0.603	0.828	0.579
SSFRs	0.024	0.031	0.957	0.226	0.802

*The sample size is small (nine galaxies) so the test results may be biased.

Our future work will focus on the spatial symmetry of UV and IR images as well as the spectral energy distribution of these galaxies. With the data release of Herschel, sub-millimeter bands and a larger sample of paired galaxies will be available for further investigation.

Chapter 5

Conclusions

Galaxies are fundamental building blocks of the structure in the universe. In order to understand the past and present states of our universe, it is necessary to understand how galaxies formed and evolved. This research focuses on star formation rates (SFRs) of galaxies, which provide important information on the physical nature and evolutionary histories of galaxies (Kennicutt 1998a), and are of strong current interest of research in astronomy.

Theoretically, the SFRs in galaxies can be inferred from the emissions from massive stars, i.e. ultraviolet continuum or optical line emissions. However, dust attenuation makes the situation complicated: dust can absorb UV and optical emissions, and then reemits them at infrared (IR) wavelengths. Therefore, our work used observational data from UV to IR to give a panchromatic view of the star formation and dust properties of galaxies. A number of aspects of our research are listed below.

5.1 Star Formation Rate Calibrations

In most cases, young stars in galaxies cannot be spatially resolved by telescopes. Therefore, we need to calibrate SFRs from the integrated light of galaxies. A number of efforts have been made to present SFR calibrations at different wavelengths. Since MIR bands can reflect the bulk of dust emission and have better spatial resolution than FIR, it is useful to present SFR calibrations using MIR bands. However, the

complicated features (e.g. polycyclic aromatic hydrocarbon (PAH) emissions, silicate absorption at 9.7 and 18 μm, molecular hydrogen lines and fine-structure lines) contained in MIR bands can introduce a large scatter in calibrations. The MIR-SFR relation is intensively studied using Spitzer IRAC 8 μm and MIPS 24 μm photometry data and spectral data (e.g. Calzetti et al. 2007; Kennicutt et al. 2009; Rieke et al. 2009). Nevertheless, there is still a debate about the reliability of MIR indicators because of the complicated features it contains.

The AKARI/IRC Point Source Catalogue Version (hereafter IRCPSC) provides positions and fluxes of all-sky survey at *S9W* (9 μm) and *L18W* (18 μm) bands (Ishihara et al. 2010). Comparing with Spitzer 8 and 24 μm bands, the AKARI IRC *S9W* and *L18W* bands cover wider wavelength ranges, including silicate absorption features at both bands and emission contributed by large PAH molecules at the *L18W* band. Using a sample of nearby galaxies with GALEX-SDSS-2MASS-AKARI data, we investigated whether and to what degree the AKARI broadband MIR data can trace SFRs, and how much the inclusion of silicate absorption and longer wavelength PAH features can affect the calibrations.

The most important contributions of this research are as follows: 1) Through a comparison with IRAS data and theoretical models, we proved that the fluxes of the extended sources in AKARI far-infrared (FIR) catalog are underestimated by the point-spread function photometry used in the pipeline. We corrected the fluxes of extended sources using AKARI diffuse maps with the software Source Extractor. 2) We presented the SFR calibrations using AKARI IRC MIR bands. In spite of complicated features contained in these bands, both the *S9W* and *L18W* emissions correlate with the SFR of galaxies with small scatters. These calibrations agree well with previous works based on the Spitzer data within the uncertainties, and should be applicable to dust-rich galaxies (Yuan et al. 2011).

The method we used to derive SFRs is the code CIGALE (Code Investigating GALaxy Emission). CIGALE is a very robust code that can fit from UV to submillimeter wavelengths simulatenously. It is based on the notion that the energy absorbed by dust is balanced by the energy emitted by dust (Noll et al. 2009). Using CIGALE, we fit the SEDs of our galaxies adopting the spectra of Maraston (2005)

stellar populations, and assuming an exponentially decayed star formation history for old stellar populations and a constant burst for young stellar populations. The infrared part of the SED is fitted using Dale & Helou (2002) templates.

The reliability of the SED fitting was checked using a sample of mock galaxies: First, the best models of SED fitting for each object are determined by a simple χ^2 minimization method; second, we add a randomly distributed error according to a Gaussian curve with $\sigma = 0.1$ to the flux to obtain a catalogue of mock galaxies; then, SEDs of these galaxies are fit again using CIGALE with the same input parameters as for the real sample; finally, the results of physical parameters are compared with the best models to see if the correlations are good.

Using the code CIGALE, we also constructed mock galaxy samples from redshift $z \sim 0$ to $z \sim 2.5$ based on our local GALEX-SDSS-2MASS-AKARI sample mentioned above. We presented SFR calibrations using the bands of Wide Infrared Survey Explorer (WISE) (bands W3 and W4 at $\sim$ 12 and 22 μm, respectively). The results are then compared with high redshift data in the COSMOS field and previous works. Our model-derived calibrations are consistent with those derived from real data, and also consistent with the calibrations given by previous works. Since WISE has very high sensitivity and all-sky coverage, these calibrations will give useful information on the evolution of SFRs at different redshift. Now we are working on applying these calibrations to the recently released data of WISE to study the star formation densities of the universe.

5.2 Star Formation and Dust Extinction in Major Mergers

Mergers of galaxies play a key role in the formation and evolution of galaxies. Since the interaction between galaxies may compress gas and induce starburst in galaxies, one of the questions about mergers is related to the strong evolution of the cosmic star formation density at $z \sim 1$. A change of merger rate at higher redshift could be responsible for this evolution. However, there are both positive and negative

pieces of evidence found in previous researches. Therefore, it is necessary to carry out a quantitative study on whether and how much the merger-induced star formation contributes to the total star formation in the universe.

Xu et al. (2010) (hereafter Xu10) claim that the different results mentioned above may be caused by different selection methods. In order to reduce the biases, they built a 'local benchmark' sample of close pairs selected from near-infrared band by carefully choosing selection criteria, and then studied the specific star formation rates (SSFRs) in mergers and their control galaxies. They found that the SSFRs in merger galaxies are enhanced in comparison to isolated galaxies, and the contribution of the merger-induced SFR is not significant comparing to the total SFR in the local universe.

However, as many previous works, their study is based only on IR bands and assumes the dust attenuation is similar in mergers and isolated galaxies. Since dust attenuation in merger galaxies is quite complicated, previous works are mostly based on theoretical modeling and numerical simulations (e.g. Bekki & Shioya 2000; Goldader et al. 2002). Our study sheds light on dust attenuation and star formation in merger galaxies using both UV (from GALEX) and IR (from Spitzer) data.

We measured the UV fluxes of the mergers and their control galaxies for Xu10's sample. With both UV and IR data, the dust attenuation can be reliably calculated. We also calculated SFRs of these galaxies by combining the FIR and UV indicated star formation rates (SFRs). Since FIR luminosities indicates obscured SFRs and UV unobscured SFRs, the SFRs calculated here are more reliable than using only one indicator. In addition, we investigated the dust attenuation and SSFRs within 4 kpc aperture of each galaxy to look into the difference at the nuclear parts of mergers and isolated galaxies.

An important finding in this work is that dust attenuation in merger galaxies is enhanced in comparison with isolated galaxies. The enhancement is found to be contributed mainly by spiral galaxies in spiral-spiral (S-S) pairs, and increases with increasing stellar mass of galaxies. We also found that the SSFRs are enhanced in merger galaxies. The SFRs in pair galaxies are found more concentrated in the central part than isolated galaxies. The IRX-β study shows that the nuclear parts of the pairs

resemble ultra-luminous infrared galaxies (ULIRGs) most.

5.3 Future research

My plan for future research is to expend my study from local galaxies to galaxies at higher redshfits. More concretely, I have the following research plans:

1. *Galaxy Mergers* In our current study, the dust attenuation and star formation in local mergers are investigated. Pair galaxies can also give us an insight to the evolution of galaxy morphology (Rampazzo & Sulentic 1992). Since the galaxies in our sample are well resolved by IR and UV observations, our next step is to investigate how the merging process affects the morphology of galaxies. By investigating the symmetry and concentration of these merger galaxies using GALEX and Spitzer images, the distribution of SFRs in these mergers can be obtained. Then, through analyzing correlation between the distribution and stellar masses, projected separations, we can have a better understanding of the effect of interaction on morphology of galaxies.

   Also, since we now have photometric data from UV to IR for these galaxies, we can also investigate the SEDs for these galaxies and compare them with isolated ones. We will also search Herschel data for these galaxies in order to investigate the influence of merging on cold dust.

2. *High redshift star forming galaxies* Herschel-ATLAS (H-ATLAS) provides an unprecedented opportunity to study star formation and dust properties of galaxies at different redshifts. With the two bands (100, 150 μm) of PACS and the three bands (250, 350, 500 μm) of SPIRE, H-ATLAS data provide information around the peak of dust emission for high redshift galaxies. We try to search for a new method to select high-redshift star-forming galaxies in H-ATLAS survey using rest-frame ultraviolet (UV) Lyman Break selection and far-infrared (FIR) colors.

   The selected sample may contain exotic objects (mergers, submillimeter galaxies

(SMGs), etc.). Therefore, it can be used to study the properties of high redshift galaxies, such as the energy sources (AGNs or starbursts), the links between SMGs and Lyman break galaxies (LBGs), etc. We will also compare the star formation in these galaxies with the local ones we have researched, and examine the MIR-SFR relations at higher redshift.

Bibliography

Abazajian, K., Adelman-McCarthy, J. K., Agüeros, M. A., et al. 2005, AJ, 129, 1755

Alonso-Herrero, A., Rieke, G. H., Rieke, M. J., et al. 2006, ApJ, 650, 835

Barnes, J. E., & Hernquist, L. 1996, ApJ, 471, 115

Barton, E. J., Geller, M. J., & Kenyon, S. J. 2000, ApJ, 530, 660

Bekki, K., & Shioya, Y. 2000, A&A, 362, 97

Bell, E. F. 2003, ApJ, 586, 794

Bell, E. F., Papovich, C., Wolf, C., et al. 2005, ApJ, 625, 23

Binney, J., & Merrifield, M. 1998, Galactic Astronomy, Princeton Series in Astrophysics (Princeton University Press)

Boissier, S., Gil de Paz, A., Boselli, A., et al. 2007, ApJS, 173, 524

Boquien, M., Buat, V., Boselli, A., et al. 2012, A&A, 539, A145

Borch, A., Meisenheimer, K., Bell, E. F., et al. 2006, A&A, 453, 869

Bridge, C. R., Appleton, P. N., Conselice, C. J., et al. 2007, ApJ, 659, 931

Brinchmann, J., Charlot, S., White, S. D. M., et al. 2004, MNRAS, 351, 1151

Bruzual A., G., Magris, G., & Calvet, N. 1988, ApJ, 333, 673

Buat, V., Giovannoli, E., Takeuchi, T. T., et al. 2011, A&A, 529, A22

Buat, V., & Xu, C. 1996, A&A, 306, 61

Buat, V., Iglesias-Páramo, J., Seibert, M., et al. 2005, ApJ, 619, L51

Buat, V., Takeuchi, T. T., Iglesias-Páramo, J., et al. 2007, ApJS, 173, 404

Burgarella, D., Buat, V., Donas, J., Milliard, B., & Chapelon, S. 2001, A&A, 369, 421

Burgarella, D., Pérez-González, P. G., Tyler, K. D., et al. 2006, A&A, 450, 69

Calzetti, D. 1997, AJ, 113, 162

Calzetti, D., Armus, L., Bohlin, R. C., et al. 2000, ApJ, 533, 682

Calzetti, D., Kinney, A. L., & Storchi-Bergmann, T. 1994, ApJ, 429, 582

Calzetti, D., Kennicutt, Jr., R. C., Bianchi, L., et al. 2005, ApJ, 633, 871

Calzetti, D., Kennicutt, R. C., Engelbracht, C. W., et al. 2007, ApJ, 666, 870

Cardelli, J. A., Clayton, G. C., & Mathis, J. S. 1989, ApJ, 345, 245

Chabrier, G. 2001, ApJ, 554, 1274

Charlot, S., & Fall, S. M. 2000, ApJ, 539, 718

Chary, R., & Elbaz, D. 2001, ApJ, 556, 562

Cole, S., Lacey, C. G., Baugh, C. M., & Frenk, C. S. 2000, MNRAS, 319, 168

Cortese, L., Boselli, A., Franzetti, P., et al. 2008, MNRAS, 386, 1157

Cortese, L., Boselli, A., Buat, V., et al. 2006, ApJ, 637, 242

Dale, D. A., & Helou, G. 2002, ApJ, 576, 159

Dale, D. A., Bendo, G. J., Engelbracht, C. W., et al. 2005, ApJ, 633, 857

Dale, D. A., Gil de Paz, A., Gordon, K. D., et al. 2007, ApJ, 655, 863

de Mello, D. F., Sulentic, J. W., de Souza, R. E., Reduzzi, L., & Rampazzo, R. 1996, A&A, 308, 387

de Vaucouleurs, G. 1974, in IAU Symposium, Vol. 58, The Formation and Dynamics of Galaxies, ed. J. R. Shakeshaft, 1–52

Desert, F.-X., Boulanger, F., & Puget, J. L. 1990, A&A, 237, 215

Domingue, D. L., Sulentic, J. W., Xu, C., et al. 2003, AJ, 125, 555

Domingue, D. L., Xu, C. K., Jarrett, T. H., & Cheng, Y. 2009, ApJ, 695, 1559

Draine, B. T., & Li, A. 2007, ApJ, 657, 810

Elbaz, D., Cesarsky, C. J., Chanial, P., et al. 2002, A&A, 384, 848

Ellison, S. L., Patton, D. R., Simard, L., & McConnachie, A. W. 2008, AJ, 135, 1877

Eminian, C., Kauffmann, G., Charlot, S., et al. 2008, MNRAS, 384, 930

Ferrara, A., Bianchi, S., Cimatti, A., & Giovanardi, C. 1999, ApJS, 123, 437

Fioc, M., & Rocca-Volmerange, B. 1997, A&A, 326, 950

Flores, H., Hammer, F., Thuan, T. X., et al. 1999, ApJ, 517, 148

Förster Schreiber, N. M., Roussel, H., Sauvage, M., & Charmandaris, V. 2004, A&A, 419, 501

Freedman Woods, D., Geller, M. J., Kurtz, M. J., et al. 2010, AJ, 139, 1857

Garn, T., & Best, P. N. 2010, MNRAS, 409, 421

Giovannoli, E., Buat, V., Noll, S., Burgarella, D., & Magnelli, B. 2011, A&A, 525, A150

Goldader, J. D., Meurer, G., Heckman, T. M., et al. 2002, ApJ, 568, 651

Gordon, K. D., Clayton, G. C., Witt, A. N., & Misselt, K. A. 2000, ApJ, 533, 236

Hammer, F., Flores, H., Elbaz, D., et al. 2005, A&A, 430, 115

Hancock, M., Smith, B. J., Struck, C., et al. 2008, in Astronomical Society of the Pacific Conference Series, Vol. 381, Infrared Diagnostics of Galaxy Evolution, ed. R.-R. Chary, H. I. Teplitz, & K. Sheth, 148

Hao, C.-N., Kennicutt, R. C., Johnson, B. D., et al. 2011, ApJ, 741, 124

Helou, G., Roussel, H., Appleton, P., et al. 2004, ApJS, 154, 253

Hernquist, L., & Barnes, J. E. 1991, Nature, 354, 210

Hirashita, H., Buat, V., & Inoue, A. K. 2003, A&A, 410, 83

Hollenbach, D. J., & Tielens, A. G. G. M. 1997, ARA&A, 35, 179

Holmberg, E. 1958, Meddelanden fran Lunds Astronomiska Observatorium Serie II, 136, 1

Hopkins, A. M. 2004, ApJ, 615, 209

Hopkins, A. M., Miller, C. J., Nichol, R. C., et al. 2003, ApJ, 599, 971

Hunter, D. 1997, PASP, 109, 937

Hwang, H. S., Elbaz, D., Dickinson, M., et al. 2011, A&A, 535, A60

Iglesias-Páramo, J., Buat, V., Donas, J., Boselli, A., & Milliard, B. 2004, A&A, 419, 109

Iglesias-Páramo, J., Buat, V., Takeuchi, T. T., et al. 2006, ApJS, 164, 38

Ishihara, D., Onaka, T., Kataza, H., et al. 2010, A&A, 514, A1

Jarrett, T. H., Chester, T., Cutri, R., et al. 2000, AJ, 119, 2498

Jonsson, P., Cox, T. J., Primack, J. R., & Somerville, R. S. 2006, ApJ, 637, 255

Kartaltepe, J. S., Sanders, D. B., Scoville, N. Z., et al. 2007, ApJS, 172, 320

Kartaltepe, J. S., Sanders, D. B., Le Floc'h, E., et al. 2010, ApJ, 721, 98

Kauffmann, G., Heckman, T. M., White, S. D. M., et al. 2003, MNRAS, 341, 33

Kawada, M., Baba, H., Barthel, P. D., et al. 2007, PASJ, 59, 389

Kelly, B. C. 2007, ApJ, 665, 1489

Kennicutt, Jr., R. C. 1998a, ARA&A, 36, 189

—. 1998b, ApJ, 498, 541

Kennicutt, Jr., R. C., & Kent, S. M. 1983, AJ, 88, 1094

Kennicutt, Jr., R. C., Roettiger, K. A., Keel, W. C., van der Hulst, J. M., & Hummel, E. 1987, AJ, 93, 1011

Kennicutt, Jr., R. C., Calzetti, D., Walter, F., et al. 2007, ApJ, 671, 333

Kennicutt, Jr., R. C., Hao, C.-N., Calzetti, D., et al. 2009, ApJ, 703, 1672

Kong, X., Charlot, S., Brinchmann, J., & Fall, S. M. 2004, MNRAS, 349, 769

Kroupa, P. 2001, MNRAS, 322, 231

Kurucz, R. L. 2005, Memorie della Societa Astronomica Italiana Supplementi, 8, 86

Lagache, G., Dole, H., Puget, J.-L., et al. 2004, ApJS, 154, 112

Lambas, D. G., Tissera, P. B., Alonso, M. S., & Coldwell, G. 2003, MNRAS, 346, 1189

Lançon, A., Hauschildt, P. H., Ladjal, D., & Mouhcine, M. 2007, A&A, 468, 205

Leger, A., D'Hendecourt, L., & Defourneau, D. 1989, A&A, 216, 148

Leger, A., & Puget, J. L. 1984, A&A, 137, L5

Li, Y., Mo, H. J., van den Bosch, F. C., & Lin, W. P. 2007, MNRAS, 379, 689

Lilly, S. J., Le Fevre, O., Hammer, F., & Crampton, D. 1996, ApJ, 460, L1

Lotz, J. M., Davis, M., Faber, S. M., et al. 2008, ApJ, 672, 177

Madau, P., Pozzetti, L., & Dickinson, M. 1998, ApJ, 498, 106

Maraston, C. 2005, MNRAS, 362, 799

Maraston, C., Daddi, E., Renzini, A., et al. 2006, ApJ, 652, 85

Melbourne, J., Koo, D. C., & Le Floc'h, E. 2005, ApJ, 632, L65

Meurer, G. R., Heckman, T. M., & Calzetti, D. 1999, ApJ, 521, 64

Meurer, G. R., Wong, O. I., Kim, J. H., et al. 2009, ApJ, 695, 765

Mo, H., van den Bosch, F., & White, S. D. M. 2010, Galaxy Formation and Evolution (Cambridge University Press)

Muñoz-Mateos, J. C., Gil de Paz, A., Boissier, S., et al. 2009, ApJ, 701, 1965

Noll, S., Burgarella, D., Giovannoli, E., et al. 2009, A&A, 507, 1793

Onaka, T., Matsuhara, H., Wada, T., et al. 2007, PASJ, 59, 401

Overzier, R. A., Heckman, T. M., Wang, J., et al. 2011, ApJ, 726, L7

Park, C., & Choi, Y.-Y. 2009, ApJ, 691, 1828

Peebles, P. J. E. 1993, Principles of Physical Cosmology

Pérez-González, P. G., Kennicutt, Jr., R. C., Gordon, K. D., et al. 2006, ApJ, 648, 987

Pickles, A. J. 1998, VizieR Online Data Catalog, 611, 863

Pierini, D., Gordon, K. D., Witt, A. N., & Madsen, G. J. 2004, ApJ, 617, 1022

Pollo, A., Rybka, P., & Takeuchi, T. T. 2010, A&A, 514, A3

Rampazzo, R., & Sulentic, J. W. 1992, A&A, 259, 43

Reddy, N. A., Erb, D. K., Pettini, M., Steidel, C. C., & Shapley, A. E. 2010, ApJ, 712, 1070

Relaño, M., Lisenfeld, U., Pérez-González, P. G., Vílchez, J. M., & Battaner, E. 2007, ApJ, 667, L141

Rettura, A., Rosati, P., Strazzullo, V., et al. 2006, A&A, 458, 717

Rieke, G. H., Alonso-Herrero, A., Weiner, B. J., et al. 2009, ApJ, 692, 556

Robertson Brant E., Ellis Richard S., Dunlop James S., McLure Ross J., & Stark Daniel P. 2010, Nature, 468, 4955, 10.1038/nature09527

Salim, S., Rich, R. M., Charlot, S., et al. 2007, ApJS, 173, 267

Salpeter, E. E. 1955, ApJ, 121, 161

Saunders, W., Sutherland, W. J., Maddox, S. J., et al. 2000, MNRAS, 317, 55

Schechter, P. 1976, ApJ, 203, 297

Schlegel, D. J., Finkbeiner, D. P., & Davis, M. 1998, ApJ, 500, 525

Schmidt, M. 1959, ApJ, 129, 243

Scoville, N., Aussel, H., Brusa, M., et al. 2007, ApJS, 172, 1

Shupe, D. L., Rowan-Robinson, M., Lonsdale, C. J., et al. 2008, AJ, 135, 1050

Smith, B. J., Struck, C., Hancock, M., et al. 2007a, AJ, 133, 791

Smith, J. D. T., Draine, B. T., Dale, D. A., et al. 2007b, ApJ, 656, 770

Steinmetz, M., & Navarro, J. F. 2002, New A, 7, 155

Struck, C. 2006, Galaxy Collisions - Dawn of a New Era, ed. J. W. Mason (Springer Verlag), 115

Surace, J. A., Shupe, D. L., Fang, F., et al. 2005, The SWIRE Data Release 2: Image Atlases and Source Catalogs for ELAIS-N1, ELAIS-N2, XMM-LSS, and the Lockman Hole

Takeuchi, T. T., Buat, V., & Burgarella, D. 2005a, A&A, 440, L17

Takeuchi, T. T., Buat, V., Heinis, S., et al. 2010, A&A, 514, A4

Takeuchi, T. T., Buat, V., Iglesias-Páramo, J., Boselli, A., & Burgarella, D. 2005b, A&A, 432, 423

Takeuchi, T. T., Yuan, F.-T., Ikeyama, A., Murata, K. L., & Inoue, A. K. 2012, ApJ in press

Telesco, C. M., Wolstencroft, R. D., & Done, C. 1988, ApJ, 329, 174

Toomre, A., & Toomre, J. 1972, ApJ, 178, 623

Tremonti, C. A., Heckman, T. M., Kauffmann, G., et al. 2004, ApJ, 613, 898

Treyer, M., Schiminovich, D., Johnson, B. D., et al. 2010, ApJ, 719, 1191

Tuffs, R. J., Popescu, C. C., Völk, H. J., Kylafis, N. D., & Dopita, M. A. 2004, A&A, 419, 821

Walcher, J., Groves, B., Budavári, T., & Dale, D. 2011, Ap&SS, 331, 1

Wechsler, R. H., Bullock, J. S., Primack, J. R., Kravtsov, A. V., & Dekel, A. 2002, ApJ, 568, 52

Woods, D. F., & Geller, M. J. 2007, AJ, 134, 527

Woods, D. F., Geller, M. J., & Barton, E. J. 2006, AJ, 132, 197

Wright, E. L., Eisenhardt, P. R. M., Mainzer, A. K., et al. 2010, AJ, 140, 1868

Wu, H., Cao, C., Hao, C.-N., et al. 2005, ApJ, 632, L79

Xu, C., & Sulentic, J. W. 1991, ApJ, 374, 407

Xu, C. K., Sun, Y. C., & He, X. T. 2004, ApJ, 603, L73

Xu, C. K., Domingue, D., Cheng, Y.-W., et al. 2010, ApJ, 713, 330

Yamamura, I. 2008, in 37th COSPAR Scientific Assembly, Vol. 37, 3529

Yamamura, I., Makiuti, S., Ikeda, N., et al. 2009, in Astronomical Society of the Pacific Conference Series, Vol. 418, AKARI, a Light to Illuminate the Misty Universe, ed. T. Onaka, G. J. White, T. Nakagawa, & I. Yamamura, 3

Young, J. S., & Scoville, N. Z. 1991, ARA&A, 29, 581

Yuan, F.-T., Takeuchi, T. T., Buat, V., et al. 2011, PASJ, 63, 1207

Zheng, X. Z., Hammer, F., Flores, H., Assémat, F., & Pelat, D. 2004, A&A, 421, 847

Zhu, Y.-N., Wu, H., Cao, C., & Li, H.-N. 2008, ApJ, 686, 155